

國立臺灣大學電機資訊學院電子工程學研究所

碩士論文

Graduate Institute of Electronics Engineering

College of Electrical Engineering & Computer Science

National Taiwan University master thesis

菱形晶格週期性金屬孔洞電漿子熱輻射器和窄頻共振

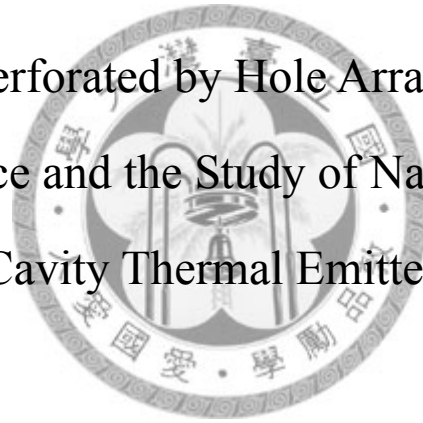
腔型熱輻射器之特性研究

The Characteristics of Plasmonic Thermal Emitters with

Top Metal Perforated by Hole Array Arranged in

Rhombus Lattice and the Study of Narrow Bandwidth

Cavity Thermal Emitters



吳奕廷

Wu Yi-Ting

指導教授：李嗣涔 博士

Advisor: Lee Si-Chen, Ph.D.

中華民國 98 年 7 月

July, 2009

致謝

在台大的日子，時光像飛梭般前進，不懂的東西太多，對實驗室的貢獻太少，好不容易有了那麼一丁點的進展，才知道魔鬼總是藏在細節裡，越是看似簡單的東西，越需要細心、耐心和提早行動絕不推拖拉的責任心。首先，我要衷心的感謝我的指導教授 李嗣涇博士。老師開放的心胸和做學問的態度深深影響著我，老師總是對各種事物保持好奇心和敏銳的洞察力。這兩年在老師的悉心指導下，獲益良多！老師永遠恭謙的態度、實事求是的精神、精湛的分析力和過人的體力，深深為我所欽佩；老師在百忙之中時仍能詳細的指引學生探究學術的真理，並在論文寫作上給予極大的幫助，我深深的感動並受用於指導教授的付出和關懷，希望老師多注意身體的健康。再來，我要感謝口試委員呂學士教授、管傑雄教授、林浩雄教授、劉致為教授、張宏鈞教授還有林致廷教授們抽空閱覽本論文並提出寶貴建議和指導，教授們學有專精的指導提升了本論文的品質和正確性。

除了國中短暫的補習兩年外，從小到大我都不曾補習，所以學校老師教的好壞深深影響著我學習的成效，進研究所後我才明白台大之所以成為台大的地方：一流師資認真教學、一流同儕認真討論；這兩年修課的老師們都教的相當好，同儕間也異常的認真，我特別感謝光電所張宏鈞老師、台積電林本堅博士、電子所郭宇軒、胡振國老師，還有電信所吳宗霖老師，他們紮實而精闢的講解，深深的補足了我理論方面的不足，浸潤於大師們的丰采是我生命中可以帶走的盛筵。

接著我要感謝交通大學電工所崔秉鉞教授，他讓我明白「態度」的重要性，做任何事情不是玩家酒，做任何事都要「玩真的全力以赴」；我還要感謝交通大學電工所林鴻志教授，教授說：「交大、台大畢業的研究生企業都會搶著要，可是你要怎麼說服你的老闆十年後繼續用你，而不是用當年交大、台大應屆畢業的研究生？」這絕對是我人生中最值得拿來警惕的一段話！特別是在這金融海嘯肆虐的非常年代，我在此表達我對兩位老師高度的敬意和深深的歉意。

接下來我要感謝我大學時的恩師，李佩雯老師、郭明庭老師還有洪志旺老師，洪老師說你看不懂是因為你看不夠久；郭老師說你看不懂是因為你看的書不夠多，一本書看不懂看五六本就會懂，這兩句話真是令我受用無窮！然而我最感激的還是李佩雯老師，李佩雯老師生動有趣的教學引領我走向奈米電子的道路，我永遠記得老師「次微米元件物理與技術」這門課，老師出的作業直接翻書永遠找不到答案，惟有深入的思考和廣泛的查資料才能作答，這樣的啟蒙訓練對

我碩士班的研究提供了莫大的幫助。我也要感謝國小的石玉美老師、國中的蘇媚慧老師和萬家春校長，謝謝你們的栽培，指引我走向正確的道路。我也要感謝高中文組班的陳淑娟同學，妳說：「為什麼要認為轉組是浪費半年？轉組是給自己再一次的選擇機會！」沒有妳我沒有勇氣從文組轉到理組去追尋夢想，也不可能拿到台灣大學電子工程研究所的碩士學位。

接下來，我要感謝 SP 組的各位：首先是聰哥、昱維、宜函和大慶，謝謝你們耐心地帶我作實驗以及無私地給予我寶貴的建議和協助；謝謝張議聰學長和葉宜涵學長，你們無私的幫忙、亦師亦友的督促和討論，是我不放棄的力量；謝謝江昱維學長和跳級生莊大慶學長(跳級了所以是學長)，雖然我們之間的討論十句話總有八句是很好笑的垃圾話 XD，但總是有那麼一兩句是切中了問題的要害、直搗問題的核心，兩年來著實裨益良多；謝謝張沛恩學弟，謝謝你各方面強大的火力支援，和您的每一次討論都能讓我在研究和分析上得到豁然開朗的快感，很好很強大！我還要衷心的感謝再感謝蔡尚儒學長，謝謝你在我累的半死曝光曝不出來的時候及時的發明了濾紙曝光密技，沒有它我可能至今一事也無成！

感謝昱維、獸哥陳鴻欣、宜修、尚儒、尚儒的總機小姐 XD、大慶、吳哲寬、賴博、恩公、小馬、剛剛、老王、阿肥陳彥廷還有 楊神哲育(我有挪台)，多虧了你們，研究生涯才能有這麼多的歡樂，那些一起吃飯、一起去台東玩，一起講垃圾笑話、一起做研究、一起去聯誼的日子，是我永遠也難忘的回憶。感謝 436 真·傑尼斯事務所的賀軍翔、大師梁為傑、型男伯川、正姐群包含：助理、阿筑、維珍還有山寨版松島菜菜子林嘿嘿，謝謝你們很辛苦的想把我改造成阮經天，雖然你們還是失敗了！還有其他熱心且強大的學長：管 group 林士弘學長、本 group 的珈擇、介宏、小胖、昭儒、正曠、tingo、昱帆、旭凱，謝謝你們各方面的幫助和包容，相信從今以後不會再有人搞爆你們的貴重儀器、一片五萬台幣的光單、和耽誤你們的進度了。也祝福恩公、浩蕨、楊鈞任、陳逸仁、尚儒、賴博、小馬、鴻欣、昱維、晨昀、書緯、家銘，願你們的未來如鳳凰花般的燦爛。我還要感謝台大財金法律雙主修的高材生劉翰芷同學，每次看到您優異的表現總讓我明白：生命可以更努力也可以更喜樂，永遠不要為遇到的任何的阻礙找藉口。

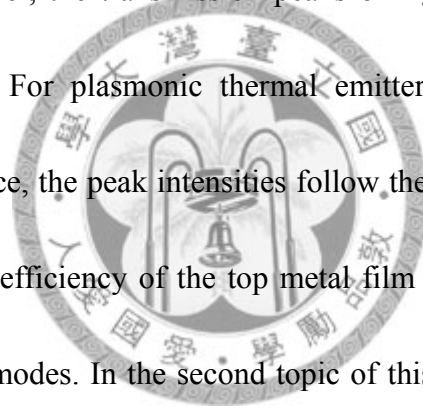
最後，我要感謝我的爸媽、和以外公、外婆、大舅和大舅媽為首的親戚們，你們總是在我最需要、最困苦的時候給我最大的幫助和關心、我衷心感謝你們的陪伴與支持，沒有你們就沒有今天的我，所有的榮耀皆歸於你們和 李嗣涇老師。

摘要

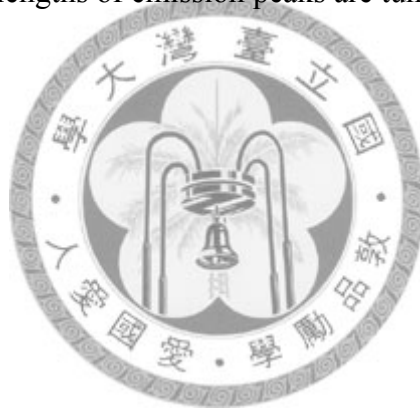
本文的第一個主題是從理論和實驗探討銀薄膜上菱形晶格週期性圓型孔洞的異常性穿透現象及其對電漿子熱幅射器幅射頻譜的影響，當銀/矽模態波長夠長使得銀/矽模態和銀/空氣模態不耦合時，銀/矽模態的穿透強度由其簡併模態的數目決定；在銀/矽模態和銀/空氣模態耦合的短波長區，銀/矽模態的峰值將因耦合而變得不明顯。對於菱形晶格電漿子熱幅射器而言，其幅射峰值的強度為黑體幅射強度乘上表面金屬的穿透效率，穿透效率正比於簡併模態的數目。本文的第二個主題是將電漿子熱幅射器的厚度增加到微米等級以分析反射頻譜和幅射頻譜中的共振腔模態，發現共振腔模態也會如同表面電漿子般的和表面週期性孔洞耦合產生布拉格散射共振腔模態；本文提出了隨機孔洞分布型共振腔熱幅射器打亂表面的週期以消除和週期有關的表面電漿子模態和布拉格散射共振腔模態以實現窄頻純頻譜的中紅外光共振腔型熱幅射器，並藉由改變孔洞的大小發現了孔洞的存在將導致了侷域型共振腔模態和 Fabry-Peort 孔洞振盪模態的產生，雖然小孔洞的隨機孔洞分布型共振腔熱幅射器可以提供純淨的幅射頻譜，其輸出強度卻受限於低密度的孔洞總面積而相當的弱。據此，本文提出了另一種新穎的短週期孔洞陣列型共振腔熱幅射器以解決輸出強度的問題：高輸出強度、純淨的幅射頻譜、可在高溫下穩定的操作、低半高寬的幅射峰值和微弱的非理想效應像是侷域型共振腔模態或 Fabry-Perot 孔洞振盪模態可以同時被達成，而且只要改變共振腔的厚度即可決定不同波長的幅射峰值。

Abstract

In this first topic of this thesis, the extraordinary transmission characteristics of silicon substrates with a silver film on top perforated with hole array arranged in a rhombus lattice are investigated in theory and experiment. It is found that the transmissions of Ag/Si modes are approximately linearly dependent on the numbers of degenerated modes in the longer wavelength range where the couplings between Ag/Si and Ag/air modes are weak. In the shorter wavelength range where Ag/Si and Ag/air are coupled together, the transmission peaks of Ag/Si modes are unapparent due to modes coupling. For plasmonic thermal emitters (PTEs) with hole array arranged in rhombus lattice, the peak intensities follow the blackbody radiation curve multiplying transmission efficiency of the top metal film which is dependent on the numbers of degenerated modes. In the second topic of this thesis, the SiO₂ thickness of PTEs is increased to the order of μm to investigate cavity modes in the reflection and emission spectra, it is found that cavity modes (CMs) would be scattered by the periodic hole array and result in many Bragg scattered CMs in the spectra. Cavity thermal emitters (CTEs) with randomly distributed hole array (RDHA) are proposed to eliminate Bragg scattered CMs and Ag/SiO₂ SPPs modes to realize narrower-band mid-infrared thermal emitters with purer spectra. The influence of hole size to the CMs is also investigated, it is found that larger scattering of light through larger



surface hole array would form the localized CMs (LCMs) and Fabry-Perot hole shape resonance (FP hole) modes. Although CTEs with RDHA can offer pure emission spectra if the hole size is small, their output intensities are very weak due to low density of total hole area. Novel CTEs with short period of hole array (SPHA) are proposed to overcome the intensity problem. High output intensity, pure emission spectra, high temperature operation, narrow full width half maximum of emission peaks and low non-ideal effect such as LCMs and FP-hole modes and could achieve simultaneously. The wavelengths of emission peaks are tunable by the thickness of the cavity.



Contents

Chapter 1 Introduction.....	1
1.1 Extraordinary transmission and surface plasmons polaritons.....	1
1.2 Infrared thermal emitters	4
1.3 The motivations of the research in this thesis	5
1.4 Frameworks of this thesis.....	6
Chapter 2 The Fundamental theorem.....	8
2.1 The fundamentals of surface plasmon polaritons.....	8
2.1.1 Surface plasmon polaritons at a single smooth interface.....	8
2.1.2 Surface plasmon polaritons at a smooth metal/dielectric/metal tri-layer structure	19
2.2 Excitation of surface plasmon polaritons	23
2.3 The extraordinary light transmission and infrared thermal emitters	26
2.3.1 Extraordinary light transmission.....	26
2.3.2 Infrared thermal emitters.....	27
2.4 Process flow.....	28
2.4.1 Fabrication processes of samples of metal hole arrays.....	28
2.4.2 Fabrication processes of infrared thermal emitters.....	30
2.5 Measurement systems.....	31
2.5.1 Introduction of FTIR.....	31
2.5.2 Transmission measurement.....	32
2.5.3 Reflection measurement.....	33
2.5.4 Thermal emission measurement	35
Chapter 3 Extraordinary transmission through a silver film perforated with hole arrays arranged in a rhombus lattice and its application in plasmonic thermal emitters.....	37
3.1 Extraordinary transmission through a silver film perforated with hole array arranged in a rhombus lattice.....	37
3.1.1 Experiments	37

3.1.2 Results and discussion	39
3.2 Plasmonic thermal emitters with top metal perforated by hole array arranged in rhombus lattice.....	53
3.2.1 Experiments	53
3.2.2 Results and discussion	54
Chapter 4 The characteristic of cavity modes in the plasmonic thermal emitters and the fabrication of narrow-band cavity thermal emitters.....	61
4.1 The characteristic of cavity modes in tri-layer Ag/SiO ₂ /Au plasmonic thermal emitters	61
4.1.1 Experiments	61
4.1.2 Results and discussion	64
4.2 Cavity thermal emitters with randomly distributed hole array and the influence of hole size to the cavity modes	72
4.2.1 Experiments	73
4.2.2 Results and discussion	77
4.3 Cavity thermal emitters with short period of hole array	90
4.3.1 Experiments	91
4.3.2 Results and discussion	92
Chapter 5 Conclusions.....	101
Appendix Proof of momentum conservation law of grating coupling	104
References.....	107

Figure Captions

Fig. 2.1 (a) SPPs at metal/dielectric interface. (b) Electric field decay rapidly away the interface. (c) The dispersion relation of the SPPs (solid line) and light line (dash line). 11

Fig. 2.2 Decay lengths of SPPs (a) in the dielectric δ_d , (b) in the metal δ_m and (c) along the interface (L_{sp}). The dielectric is SiO₂ and the metal is Ag. 18

Fig. 2.3 (a) The metal/dielectric/metal (MDM) tri-layer structure, the thickness of dielectric is w . The red lines represent the intensity of SPPs of two interfaces and will couple together once Eq. (2.56) is satisfied; (b) the simpler equivalent structure of Fig. 2.3 (a) once Eq. (2.56) is satisfied. 22

Fig. 2.4 Parallel polarization plane waves (TM mode) impinge on the one dimensional grating whose period is Λ . The blue lines, green lines and red lines represent the incident lights, reflection lights and transmission lights respectively. ... 25

Fig. 2.5 The (a) side and (b) top view of a silicon substrate with a silver film on top perforated with hole array arranged in a rhombus lattice. φ is the incident and reflective angle, $k_{//}$ is the light wave vector component parallel to the sample surface along ΓK direction. 27

Fig. 2.6 (a) The side view and (b) top view of infrared thermal emitters. 28

Fig. 2.7 The principle of Fourier transform infrared spectrometry. 32

Fig. 2.8 The experiment setup of transmission at incline incidence. 33

Fig. 2.9 Schematic diagram of reflection measurement in the angle φ from 12° to 65°. 34

Fig. 2.10 The optical path and reflection mirrors of reflection measurement 34

Fig. 2.11 The thermal emitter chamber, (a) top view (b) side view. 36

Fig. 3.1 The (a) side and (b) top view of a silicon substrate with a silver film on top perforated with hole array arranged in a rhombus lattice. $|\vec{a}_1| = |\vec{a}_2| = a = 5\mu\text{m}$ and $d = 2.5\mu\text{m}$. φ is the incident and transmission angle, $k_{//}$ is the light wave vector component parallel to the sample surface along ΓK direction. 38

Fig. 3.2 The dispersion relation extracted from transmission spectra for sample (a) A, (b) B, (c) C, (d) D, (e) E, (f) F and their modes analyses for sample (g) A, (h) B, (i) C, (j) D, (k) E, (l) F. The green and red dashed lines are the calculated dispersion curves of Ag/SiO₂ and Ag/air modes, respectively. 42

Fig. 3.3 The transmission spectra of sample C with incident angle φ varying from 0° to 60° by 10° step. 44

Fig. 3.4 The transmission spectra for samples (a) A, (b) B, (c) C, (d) D, (e) E and (f) F

in the normal direction $\varphi=0^\circ$.	48
Fig. 3.5 (a) The schematic cross section and (b) top view of PTEs with top metal perforated by hole array arranged in rhombus lattice with $ \vec{a}_1 = \vec{a}_2 =a=5\mu\text{m}$ and $d=2.5\mu\text{m}$.	54
Fig. 3.6 Emission spectra in the normal direction of all five PTEs with rhombus lattice. The lattice angle $\theta=(a) 50^\circ, (b) 60^\circ, (c) 70^\circ, (d) 80^\circ$ and $(e) 90^\circ$.	59
Fig. 4.1 (a) The side view and (b) top view of PTEs with the thickness of SiO_2 $t_{\text{ox}}=0.55, 2\mu\text{m}$ and $2.6\mu\text{m}$ for samples A, B and C, respectively. The surface silver films are perforated with hole array in hexagonal lattice with $ \vec{a}_1 = \vec{a}_2 =a=3\mu\text{m}$ and $d=1.5\mu\text{m}$. φ is the incident and reflective angle, $k_{//}$ is the parallel component of wave vectors of lights.	63
Fig. 4.2 Emission spectra of samples (a) A, (b) B and (c) C at temperature 300°C .	65
Fig. 4.3 The dispersion relation of reflection spectra for samples (a) A, (b) B, (c) C and their modes analysis for samples (d) B and (e) C. The blue dashed lines are the calculated results of Eq. (4.9).	69
Fig. 4.4 (a) The measured dispersion relation of reflection spectra and (b) corresponding modes analysis for sample B. The blue dashed lines are the calculations results of Eq. (4.13).	72
Fig. 4.5 (a) The side view and (b) top view of CTEs with RDHA.	73
Fig. 4.6 The relation between transmission and the distribution of the nearest center-to-center distance of holes for sample I.	77
Fig. 4.7 Theoretical dispersion curves of CM for CTEs with RDHA. $t_{\text{ox}}=2\mu\text{m}$	78
Fig. 4.8 The dispersion relation of reflection spectra for sample (a) D, (b) E, (c) F and their modes analysis for sample (d) D, (e) E and (f) F. The blue dashed lines are the calculated results of Eq. (4.9).	80
Fig. 4.9 The dispersion relation of reflection spectra of samples (a) G, (b) H and (c) I.	81
Fig. 4.10 The theoretical dispersion curves of CMs and LCMs.	83
Fig. 4.11 The dispersion relation of reflection spectra of samples (a) J and (b) K.	84
Fig. 4.12 The relation of the wavelength of FP-hole modes to the hole diameter.	85
Fig. 4.13 The reflection spectra of sample L to N with the fixed incident and reflective angles $\varphi = 12^\circ$ and the fixed diameters of holes $d=2\mu\text{m}$.	86
Fig. 4.14 The emission spectra of samples (a) E, (b) H, (c) I and (d) J in the normal direction ($\varphi = 0^\circ$).	89
Fig. 4.15 The dispersion relation of reflection spectra for (a) sample O and (b) sample	

P. The period of hole array for sample O and P are $2.3\ \mu\text{m}$ and $1.7\ \mu\text{m}$, respectively.....94

Fig. 4.16 The emission spectra in the normal direction $\varphi=0^\circ$ for (a) sample O and (b) sample P. The period of hole array for sample O and P are $2.3\ \mu\text{m}$ and $1.7\ \mu\text{m}$, respectively. The thicknesses of SiO_2 of both samples are $2\ \mu\text{m}$. ..96

Fig. 4.17 The emission spectrum for sample Q. The thickness of SiO_2 is $1.6\ \mu\text{m}$97

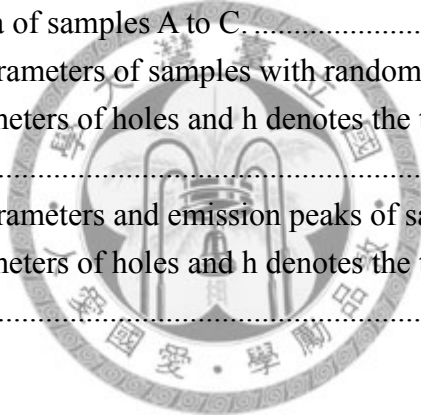
Fig. 4.18 The calculation of minimum skin depth of subwavelength holes to the wavelengths of lights guided inside the holes according to Eq. (4.23).99

Fig. 4.19 The reflection spectra at $\varphi=12^\circ$ for sample E which is a CTE with 15nm top thin silver film and sample P which is a CTE with SPHA. The period and diameter of hole array of sample P are $1.7\ \mu\text{m}$ and $1\ \mu\text{m}$, respectively.....99



List of Tables

Table 2.1 Conditions and purposes of the cleaning solvents	29
Table 2.2 The photolithography conditions	30
Table 3.1 The structure parameters of samples A to F.	39
Table 3.2 The theoretical and measured parameters of EOT in the normal direction for silicon substrates with top silver film perforated with hole array arranged in rhombus lattice.	49
Table 3.3 The comparisons of normalized transmission intensities for wavelength larger than 10 μm	51
Table 3.4 The theoretical and measured parameters of EOT for PTEs with rhombus lattice.	60
Table 4.1 The comparisons between theoretical peak wavelengths and measured results of emission spectra of samples A, B and C in $\varphi = 0^\circ$ direction.	70
Table 4.2 The comparisons between theoretical values and measured results of emission spectra of samples A to C.	71
Table 4.3 The structure parameters of samples with randomly distributed hole array, d denotes the diameters of holes and h denotes the thickness of to silver film.	74
Table 4.4 The structure parameters and emission peaks of samples O, P and Q, d denotes the diameters of holes and h denotes the thickness of to silver film.	91



Chapter 1 Introduction

1.1 Extraordinary transmission and surface plasmons polaritons

Optical transmission through a single aperture, such as slit and hole in an opaque screen, has been studied for years. In 1944, Hans Bethe [1] derived an analytical expression which tells that for a single hole perforated in the thin metal film with diameter r , the transmission ratio of light normalized to the hole area in the normal direction is

$$T(\lambda) = \frac{64(kr)^4}{27\pi^2} \approx 374.3 \left(\frac{r}{\lambda}\right)^4 \quad (1.1)$$

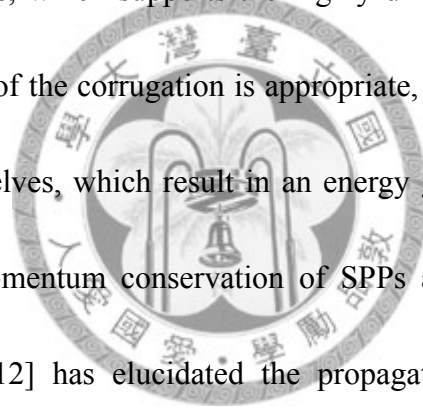
where $k=2\pi/\lambda$ is the wavenumber of incident light, λ is the wavelength of incident light.

According to this standard diffraction theory, it has been thought that subwavelength hole have a very low transmission ratio since the transmission is proportional to $(r/\lambda)^4$. However, in 1998, Ebbesen *et al.* [2-3] had reported that metal films perforated with two-dimensional subwavelength periodic hole arrays exhibit extraordinary transmission (EOT) which exceeded the prediction of Eq. (1.1) resulting from resonant excitation of surface plasmons polaritons (SPPs). Even more, the transmission ratio normalized to the hole area is larger than 1, the flux of photons per unit area emerging from the hole is larger than the incident flux per unit area of hole.

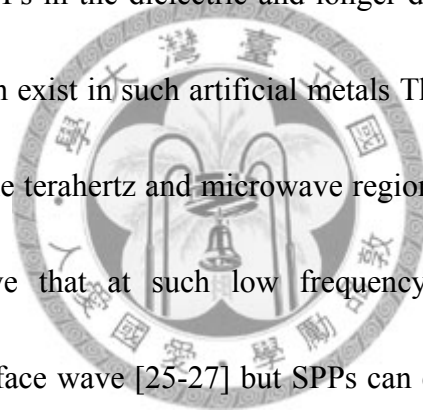
SPPs, first reported by Ritchie [4-5] in the 1950s, are electromagnetic

excitations that propagate along a dielectric/metal interface. These waves are trapped on the interface and decay rapidly away the interface. Grupp *et al.* [6], provide direct evidence that the enhanced transmission through subwavelength apertures is mediated by SPPs on metal surface.

For circular hole surrounded by concentric grooves and single slit surrounded by periodic parallel grooves in a metallic film, the emitted light from such apertures concentrate in a specific direction with a constrained range of angles instead of diverging in all directions, which supports the highly directional beaming nature of SPPs [7-9]. If the period of the corrugation is appropriate, the SPPs can Bragg reflect and interfere with themselves, which result in an energy gap in the SPPs dispersion relation [10-11]. The momentum conservation of SPPs and light through periodic perforated hole arrays [12] has elucidated the propagation of SPPs. When light impinges on perforated metal films, localized surface plasmons (LSPs) result from the individual hole-shape resonance will shift the wavelength of emission peak and affect the transmittance [13-16]. As the sizes of the perforated apertures become smaller than the thickness of the metal film, a transition from SPP mode to waveguide resonance mode was observed [17]. In addition, the combined effects of SPP and Fabry-Perot resonances determined by the thickness of perforated metal film have been studied in the THz region theoretically and experimentally [18-19]. According to



theoretical analyses, if the perforated metal film has symmetric interfaces, then SPPs at the top and the bottom interfaces are coupled via evanescent waves [20,21], which consistent with the theorem of *spoof SPPs* what Pendry et al. [22] discovered three years later. The theorem of spoof SPPs states that metal films perforated with an array of subwavelength and sub-period holes can be viewed as an effective metals with a plasma frequency equal to the cut-off frequency of holes which is much lower than the plasma frequency of original metals. This spoof low plasma frequency offer higher confinement of SPPs in the dielectric and longer decay length of SPPs inside the holes, strong SPPs can exist in such artificial metals This explained why the EOT can still be observed in the terahertz and microwave region [23, 24] where traditional theorem of SPPs believe that at such low frequency only highly delocalized Sommerfeld-Zenneck surface wave [25-27] but SPPs can exist in the metal/dielectric interface. It solved the long-term question how such weak SPPs in terahertz and microwave contribute strong extraordinary light transmission.



EOT can be applied in the fields of subwavelength photolithography [28-29], solar cell [30-31], quantum dot infrared photodetector [32], biosensor [33], channel waveguide [34], modulator [35], tunable light sources/filters [36, 37] and plasmonic thermal emitters [38-41].

1.2 Infrared thermal emitters

Mid-infrared light source is important in the fields of gas sensing, free space optical communication, healthcare, missile countermeasures and biomedicine [42-43].

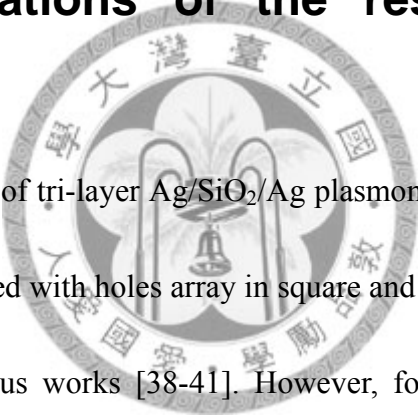
Blackbody radiation is a good mid-infrared light source since maximum intensity of radiation located at the wavelength of $5\mu\text{m}$ is in the temperature around 300°C according to Wien's law. The physical, chemical and optical properties of most optical materials in this temperature are stable. A simple optical filter combined with a hot source can filter out unwanted parts of blackbody radiation and form a stable mid-infrared light source without complex quantum structures, epitaxy and expensive cooling equipments which are needed in the infrared semiconductor laser [42].

Infrared thermal light sources with filters structures to tailor the thermal radiation spectra had been studied for long time from one dimensional to three dimensional theoretically and experimentally [38-41, 44-50]. Among them, emitters which use lossless dielectric *distributed Bragg reflectors (DBR)* as the filters [44-46] may be thought to the best structures since low full width half maximum (FWHM) and high power output can be achieved simultaneously. However, it is hard to use these structures in mid-infrared since the emissivity of most optical materials is not small in the mid-infrared [51]. For example, SiO_2 , a common optical thin film material, have large extinction coefficient (k) around $10\mu\text{m}$ [52] contributed from strong phonon

vibration [53] makes it impossible to be the material of DBR without strong thermal radiation.

An alternative approach to form the filters without strong emissivity is to use metals perforated with hole arrays whose emissivity are low. This kind of thought was realized by Tsai et al. [38-41] as plasmonic thermal emitters using thin dielectric as the emission source. The emissivity of thin dielectric sandwiched between two metals can be enhanced greatly [54] by the additional dipole radiation in the cavity [55-56].

1.3 The motivations of the research in this thesis



The emission spectra of tri-layer Ag/SiO₂/Ag plasmonic thermal emitters (PTEs) with top Ag layer perforated with holes array in square and hexagonal lattice had been investigated in the previous works [38-41]. However, for two dimensional lattice, square and hexagonal lattices are the special case of a rhombus lattice with specific lattice angle $\theta=90^\circ$ and 60° . It is interesting to know how emission spectra changes when θ changes from 90° to 40° by 10° step. Besides, the intensity distribution of various emission peaks was not known either.

Tsai et al. [41] had point out that once the thickness of SiO₂ becomes thicker than $1.3\mu\text{m}$, not only SPPs mode but also parallel-plate waveguide mode (which is also known as Fabry-Perot resonance mode or simply cavity mode) would appear in the

emission spectra. However, not all peaks can be explained satisfactorily by the traditional theorem of surface plasmon polaritons or waveguide modes. Besides, the red shift of emission peaks were also observed but the reason was not clear. These questions are the major goal of research in this thesis.

1.4 Frameworks of this thesis

The contents of this thesis are outlined as follows.

In this chapter 2, the basic theorem of SPPs and the excitation of SPPs using grating coupling will be introduced. Next, the basic theorem of extraordinary transmission of light through subwavelength periodic hole arrays and the basic operating principle of PTEs will be introduced. Finally, the fabrication processes and the measurement systems will be elucidated.

In chapter 3, the transmission characteristics of silicon substrates with silver films on top perforated with hole array arranged in a rhombus lattice have been investigated, it is found that the transmission of Ag/Si modes are approximately linearly dependent on the numbers of degenerated modes in the longer wavelength range where the couplings between Ag/Si and Ag/air modes are weak. In the shorter wavelength range where Ag/Si and Ag/air are coupled together, the transmission intensities are approximately constant without apparent peaks in the wavelength range longer than the Ag/air modes and decay rapidly in the wavelength smaller than the

Ag/air modes due to asymmetric slope of the Ag/air mode in the spectra. PTEs with rhombus lattice had been investigated experimentally and theoretically either. Only hexagonal lattice produce the strongest radiation peak due to largest degenerated modes. The peak intensities follow the blackbody radiation curve multiplying transmission efficiency of the top metal film which is dependent on the numbers of degenerated modes.

In chapter 4, the emission spectra of PTEs with oxide thickness of 0.55, 2 and 2.6 μm were investigated, a new model was developed to successfully explain and fit the experimental results which are not able to explain well in the past [41]. According to this new model, CTEs with randomly distributed hole arrays (RDHA) are proposed to offer pure cavity mode radiation spectra with small full width at half maximum (FWHM) which are better than those of the traditional PTEs. However, the low output intensity due to low density of holes is its drawback. The influence of hole size to the emission peaks and reflection spectra was investigated either. In order to overcome the problem of low output intensity, novel cavity thermal emitters with short period were invented to overcome this problem; high output intensity, low FWHM and pure emission spectra can be realized simultaneously.

Finally, the conclusions are given in chapter 5; the mathematical derivations of gratings coupling are given in Appendix.

Chapter 2 The Fundamental theorem

In this chapter, the basic theorem of surface plasmon polaritons (SPPs), excitation of SPPs using grating coupling will be introduced. Next, the basic theorem of extraordinary transmission of light through subwavelength periodic hole array and the basic operating principle of plasmonic thermal emitters will be introduced. Finally, the fabrication processes and the measurement system will be elucidated.

2.1 The fundamentals of surface plasmon polaritons

2.1.1 Surface plasmon polaritons at a single smooth interface

2.1.1.1 Transverse electric (TE) mode

First, assume that surface waves of transverse electric (TE) mode can exist in the interface ($z=0$) of the metal and dielectric and decay rapidly away the interface as shown in Fig. 2.1(a) and (b). The electric fields components in Cartesian coordinates can be described as follow.

For $z>0$

$$E_y(x, z, \omega) = A_d e^{-k_d z} e^{i(k_x x - \omega t)} \quad (2.1)$$

and for $z<0$

$$E_y(x, z, \omega) = A_m e^{k_m z} e^{i(k_x x - \omega t)} \quad (2.2)$$

where $\text{Re}[k_d] > 0$ and $\text{Re}[k_m] > 0$ indicate the fact that surface waves decay rapidly away the interface. A_d and A_m are constants. k_{xd} and k_{xm} denote as *propagation constants* of the traveling waves in dielectric and metal respectively. Both E_x and E_z are zero in the dielectric and metal for TE mode. Let the materials in Fig 2.1 (a) be homogeneous, that is, the complex relative dielectric constant ϵ_r , complex relative permeability μ_r , k_{xd} , k_{xm} , k_d and k_m are all independent of positions (x, y, z).

Substituting Eqs. (2.1) and (2.2) into Maxwell equation $\nabla \times \vec{E} = -j\omega\mu_0\mu_r\vec{H}$, the magnetic fields of both regions can be obtained

For $z > 0$

$$H_x(x, z, \omega) = -iA_d \frac{1}{\omega\mu_0\mu_{rd}} k_d e^{ik_{xd}x} e^{-k_d z} \quad (2.3)$$

$$H_z(x, z, \omega) = A_d \frac{k_{xd}}{\omega\mu_0\mu_{rd}} e^{ik_{xd}x} e^{-k_d z} \quad (2.4)$$

and for $z < 0$

$$H_x(x, z, \omega) = iA_m \frac{1}{\omega\mu_0\mu_{rm}} k_m e^{ik_{xm}x} e^{k_m z} \quad (2.5)$$

$$H_z(x, z, \omega) = A_m \frac{k_{xm}}{\omega\mu_0\mu_{rm}} e^{ik_{xm}x} e^{k_m z} \quad (2.6)$$

where μ_0 is the permeability in the vacuum; μ_{rd} and μ_{rm} are the relative permeability of dielectric and metal respectively.

The following boundary conditions of Maxwell equations should be satisfied at the interface ($z=0$)

$$E_y \text{ continuity Eq. (2.1) = Eq. (2.2)} \quad (2.7)$$

$$H_x \text{ continuity Eq. (2.3) = Eq. (2.5)} \quad (2.8)$$

Solving Eq. (2.7), Eq. (2.8) and let $\mu_{rd} = \mu_{rm} = 1$ for non-magnetic materials, the solutions of above equations are

$$A_d e^{ik_{xd}x} = A_m e^{ik_{xm}x} \quad (2.9)$$

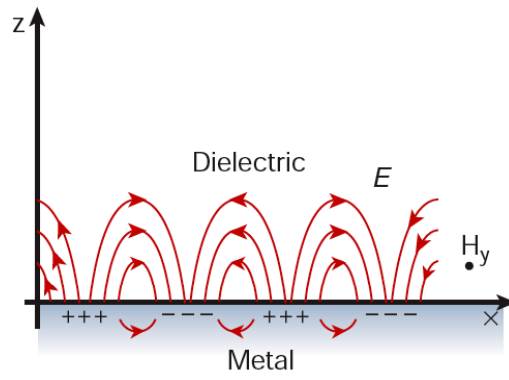
$$-A_d k_d e^{ik_{xd}x} = A_m k_m e^{ik_{xm}x} \quad (2.10)$$

Substituting Eq. (2.9) into Eq. (2.10) yields

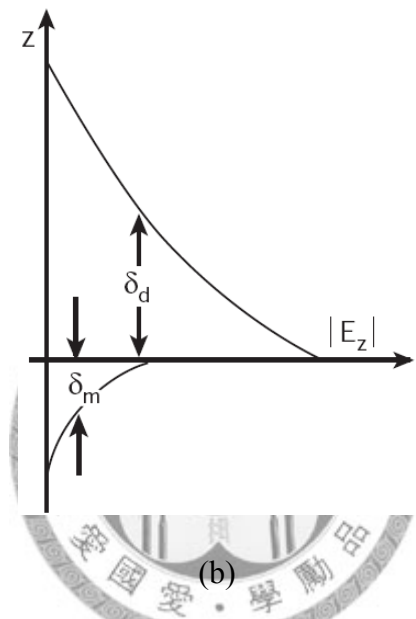
$$A_m e^{ik_{xm}x} (k_d + k_m) = A_d e^{ik_{xd}x} (k_d + k_m) = 0 \quad (2.11)$$

Since $\text{Re}[k_d] > 0$ and $\text{Re}[k_m] > 0$, the only solution of Eq. (2.11) is $A_m = A_d = 0$ and the electromagnetic fields intensity from Eq. (2.1) to Eq. (2.6) become all zero. So, *there are no surface TE waves existing in the interface of two non-magnetic materials.*

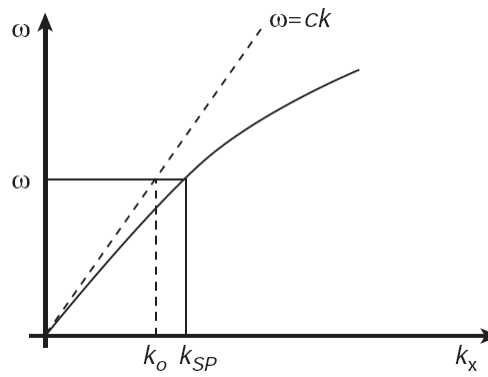
However, it should be noted that surface TE waves can still exist if the interface is formed by magnetic materials or metamaterials where $\mu_{rd} \neq \mu_{rm}$ [56].



(a)



(b)



(c)

Fig. 2.1 (a) SPPs at metal/dielectric interface. (b) Electric field decay rapidly away the interface. (c) The dispersion relation of the SPPs (solid line) and light line (dash line).

2.1.1.2 Transverse magnetic (TM) mode

Next, consider the case of surface transverse magnetic waves (TM mode), the magnetic fields can be presented as follows

For $z > 0$

$$H_y(x, z, \omega) = A_d e^{-k_d z} e^{i(k_{xd}x - \omega t)} \quad (2.12)$$

and for $z < 0$

$$H_y(x, z, \omega) = A_m e^{k_m z} e^{i(k_{xm}x - \omega t)} \quad (2.13)$$

The definitions and characteristics of A_d , A_m , k_{xd} , k_{xm} , k_d and k_m are identical as what were defined in Sec. 2.1.1.1. Both H_x and H_z are zero in dielectric and metal for TM mode.

Substituting Eq. (2.12) and Eq. (2.13) into Maxwell equation $\nabla \times \vec{H} = j\omega\epsilon_0\epsilon_r \vec{E}$, the magnetic fields of both regions can be obtained

For $z > 0$

$$E_x(x, z, \omega) = iA_d \frac{1}{\omega\epsilon_0\epsilon_{rd}} k_d e^{ik_{xd}x} e^{-k_d z} \quad (2.14)$$

$$E_z(x, z, \omega) = -A_d \frac{k_{xd}}{\omega\epsilon_0\epsilon_{rd}} e^{ik_{xd}x} e^{-k_d z} \quad (2.15)$$

and for $z < 0$

$$E_x(x, z, \omega) = -iA_m \frac{1}{\omega\epsilon_0\epsilon_{rm}} k_m e^{ik_{xm}x} e^{k_m z} \quad (2.16)$$

$$E_z(x, z, \omega) = -A_m \frac{k_{xm}}{\omega \epsilon_0 \epsilon_{rm}} e^{ik_{xm}x} e^{k_m z} \quad (2.17)$$

where ϵ_0 is the permittivity in the vacuum; ϵ_{rd} and ϵ_{rm} are the relative permittivity of dielectric and metal respectively.

The following boundary conditions of Maxwell equations should be satisfied at the interface ($z=0$)

$$H_y \text{ continuity Eq. (2.12) = Eq. (2.13)} \quad (2.18)$$

$$E_x \text{ continuity Eq. (2.14) = Eq. (2.16)} \quad (2.19)$$

$$D_z \text{ continuity Eq. (2.15) } \times \epsilon_0 \epsilon_{rd} = \text{Eq. (2.17) } \times \epsilon_0 \epsilon_{rm} \quad (2.20)$$

Solving Eq. (2.18) - Eq. (2.20) yields

$$A_d e^{ik_{xd}x} = A_m e^{ik_{xm}x} \quad (2.21)$$

$$A_d \frac{1}{\epsilon_{rd}} k_d e^{ik_{xd}x} = -A_m \frac{1}{\epsilon_{rm}} k_m e^{ik_{xm}x} \quad (2.22)$$

$$A_d k_{xd} e^{ik_{xd}x} = A_m k_{xm} e^{ik_{xm}x} \quad (2.23)$$

Substituting Eq. (2.21) into Eq. (2.22) and Eq. (2.23) yields

$$A_d e^{ik_{xd}x} \left(\frac{1}{\epsilon_{rd}} k_d + \frac{1}{\epsilon_{rm}} k_m \right) = A_m e^{ik_{xm}x} \left(\frac{1}{\epsilon_{rd}} k_d + \frac{1}{\epsilon_{rm}} k_m \right) = 0 \quad (2.24)$$

$$k_{xd} = k_{xm} \quad (2.25)$$

Since both A_d and A_m can not be zero, the solution of Eqs. (2.24) - (2.25) is

$$\left(\frac{1}{\epsilon_{rd}} k_d + \frac{1}{\epsilon_{rm}} k_m \right) = 0 \quad (2.26)$$

Eq. (2.26) can be rearranged as

$$\frac{k_d}{k_m} = -\frac{\varepsilon_{rd}}{\varepsilon_{rm}} \quad (2.27)$$

Since the materials are homogenous, the wave equations Eq. (2.12) and Eq. (2.13) should obey the Helmholtz equation [57] $\nabla^2 \vec{H} + k_0^2 \mu_r \varepsilon_r \vec{H} = 0$. Substituting Eq. (2.12) and Eq. (2.13) into Helmholtz equation, the following equations can be obtained

$$k_d^2 - k_{xd}^2 + k_0^2 \mu_{rd} \varepsilon_{rd} = 0 \quad (2.28)$$

$$k_m^2 - k_{xm}^2 + k_0^2 \mu_{rm} \varepsilon_{rm} = 0 \quad (2.29)$$

where $k_0 = \frac{\omega}{c}$ and c is the light speed in the vacuum.

Dividing Eq. (2.28) by Eq. (2.29) gives

$$\left(\frac{k_d}{k_m} \right)^2 = \frac{k_{xd}^2 - k_0^2 \mu_{rd} \varepsilon_{rd}}{k_{xm}^2 - k_0^2 \mu_{rm} \varepsilon_{rm}} \quad (2.30)$$

Substituting Eq. (2.25), Eq. (2.27) into Eq. (2.30) and let $\mu_{rd} = \mu_{rm} = 1$ for non-magnetic material assumption, the following results are obtained

$$k_{xd} = k_{xm} = k_0 \sqrt{\frac{\varepsilon_{rd} \times \varepsilon_{rm}}{\varepsilon_{rd} + \varepsilon_{rm}}} = \frac{\omega}{c} \sqrt{\frac{\varepsilon_{rd} \times \varepsilon_{rm}}{\varepsilon_{rd} + \varepsilon_{rm}}} \quad (2.31)$$

$$k_d = k_0 \sqrt{\frac{-(\varepsilon_{rd}^2)}{\varepsilon_{rd} + \varepsilon_{rm}}} \quad (2.32)$$

$$k_m = k_0 \sqrt{\frac{-(\varepsilon_{rm}^2)}{\varepsilon_{rd} + \varepsilon_{rm}}} \quad (2.33)$$

where k_{xd} and k_{xm} in the Eq. (2.31) are also known as the *dispersion relation of SPPs*

and usually denoted as k_{sp} . Substituting Eq. (2.25) into Eq. (2.23) yields

$$A_d = A_m = A \quad (2.34)$$

where A is a non-zero constant. Eqs. (2.31) - (2.34) can now be substituting back into Eqs. (2.12) - (2.17) and the whole electric and magnetic fields distributions in real space can be obtained.

Finally, it should be noted that Eq. (2.27) indicates that $\text{Re}[\epsilon_{rd}]$ and $\text{Re}[\epsilon_{rm}]$ should have opposite because of $\text{Re}[k_d] > 0$ and $\text{Re}[k_m] > 0$. Since only metals can offer negative dielectric constants according to Drude model[58, 59]. It is impossible to generate the surface waves on a smooth dielectric/dielectric or most metal/metal interface whose dielectric constants are both positive or both negative. *Surface waves can only exist in the metals/dielectric interface and only TM mode is allowed; these surface TM waves are named as surface plasmon polaritons (SPPs) by Ritchie in 1957 [4].*

Now, let's go back to see why it is called surface plasmon polaritons [5]. The non-zero electric fields inside the metal implies that the free electrons inside metals will oscillate with these electric fields together as shown in Fig. 2.1(a); the collection of free electrons oscillating in certain common frequency are called *plasmon* [57]. Since these only occur near the surface of metal and decay rapidly inside the metal, it is more accurate to call it *surface plasmon*. The coupling of free oscillating electrons

and surface waves in the dielectric forms a newly kind of virtual particles propagating along the interface and carry with their own energies $\hbar\omega$ and momentums $\hbar k_{sp}$ according to the Eq. (2.31) and Fig. 2.1(c). These virtual particles are named as *polaritons* since only TM mode is allowed for non-magnetic materials. It should be note that the momentums of SPPs are always larger than the momentums of the propagation light at the same frequency, as shown in Fig. 2.1 (c) and Eq. (2.31)

$$\hbar k_{sp} = \hbar k_0 \sqrt{\frac{\epsilon_{rd} \times \epsilon_{rm}}{\epsilon_{rd} + \epsilon_{rm}}} = \hbar k_0 \sqrt{\epsilon_{rd}} \times \sqrt{\frac{1}{\frac{\epsilon_{rd}}{\epsilon_{rm}} + 1}} > \hbar k_0 \sqrt{\epsilon_{rd}} \approx \hbar k_0 n_d \quad (2.35)$$

where $n_d \approx \sqrt{\epsilon_{rd}}$ is the refractive index of dielectric and usually >1 . $\epsilon_{rm} < 0$ for most metals according to Drude mode [58, 59].

Finally, the decay lengths of SPPs inside the dielectric and the metal are denoted as δ_d and δ_m , respectively; their values are defined as the distances where the intensity of electric fields drop to 1/e

$$\delta_d = \frac{1}{\text{Re}[k_d]} \quad (2.36)$$

$$\delta_m = \frac{1}{\text{Re}[k_m]} \quad (2.37)$$

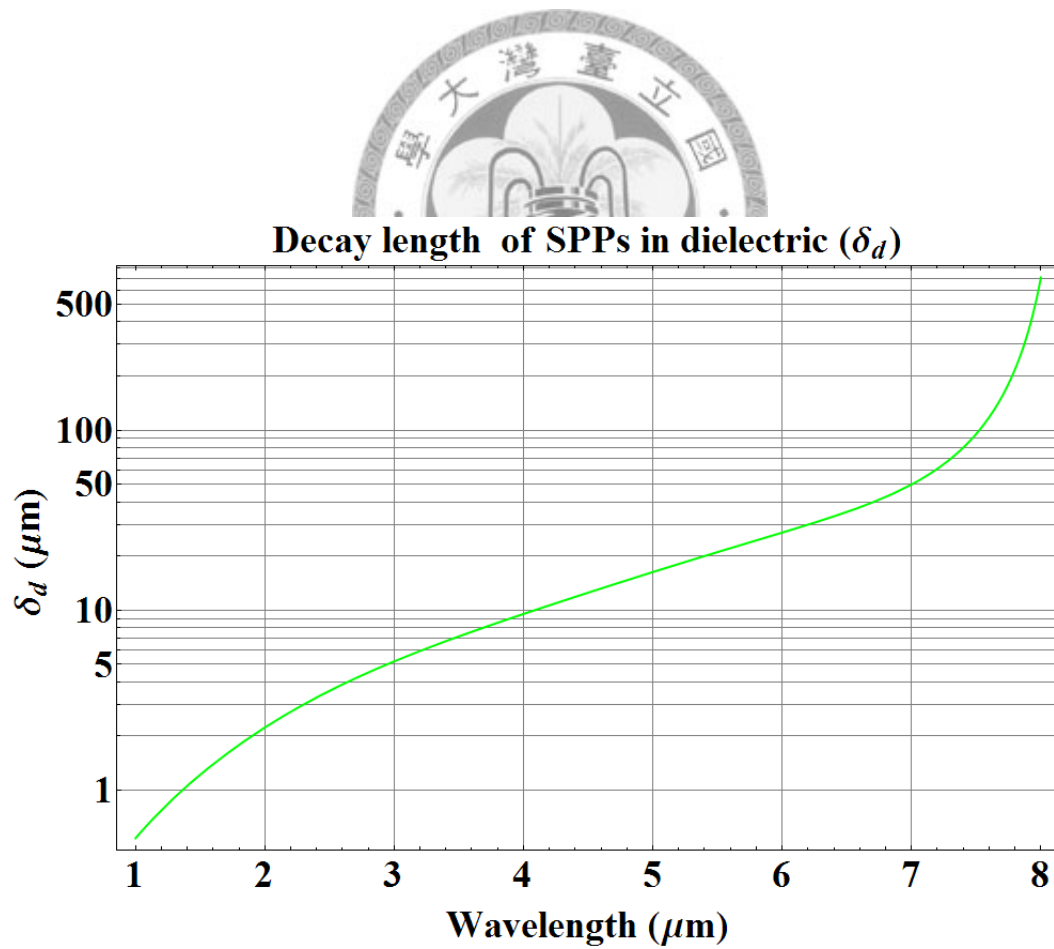
where k_d and k_m can be calculated from Eq. (2.32) and Eq. (2.33).

The decay length of SPPs propagating along the interface is denoted as L_{sp} and is defined as the distances where the energy of SPPs drops to 1/e

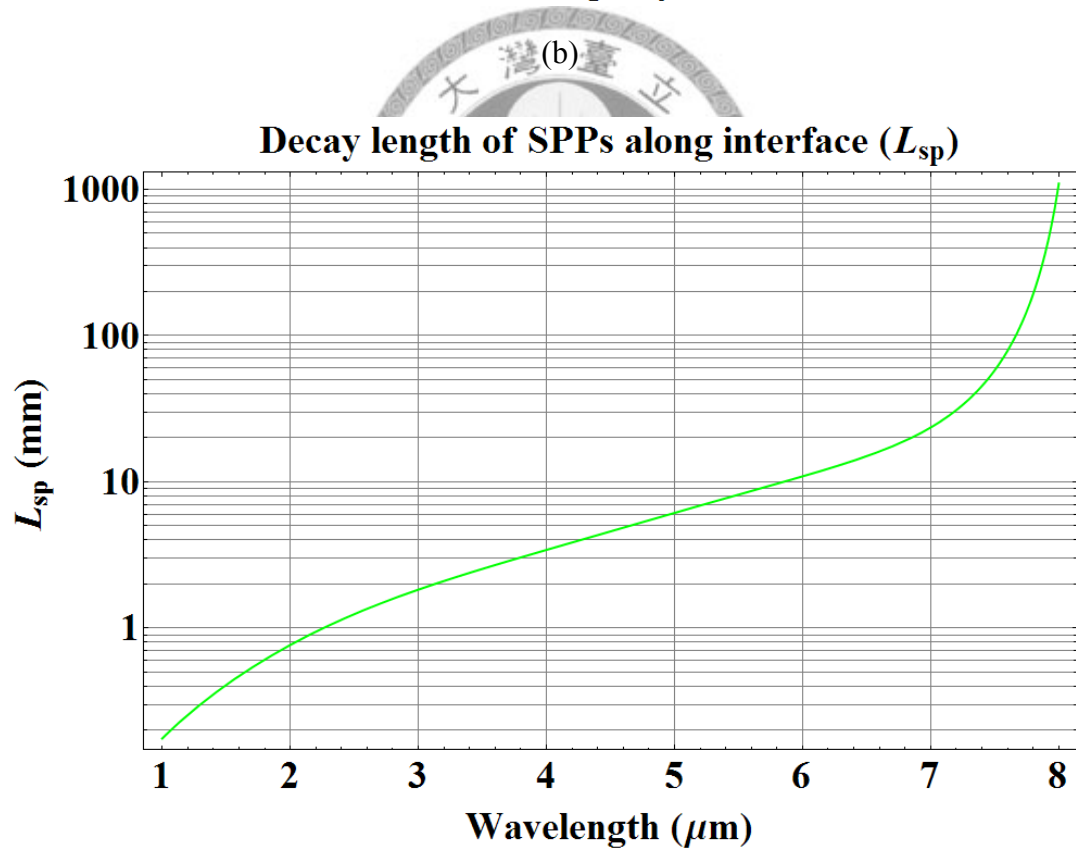
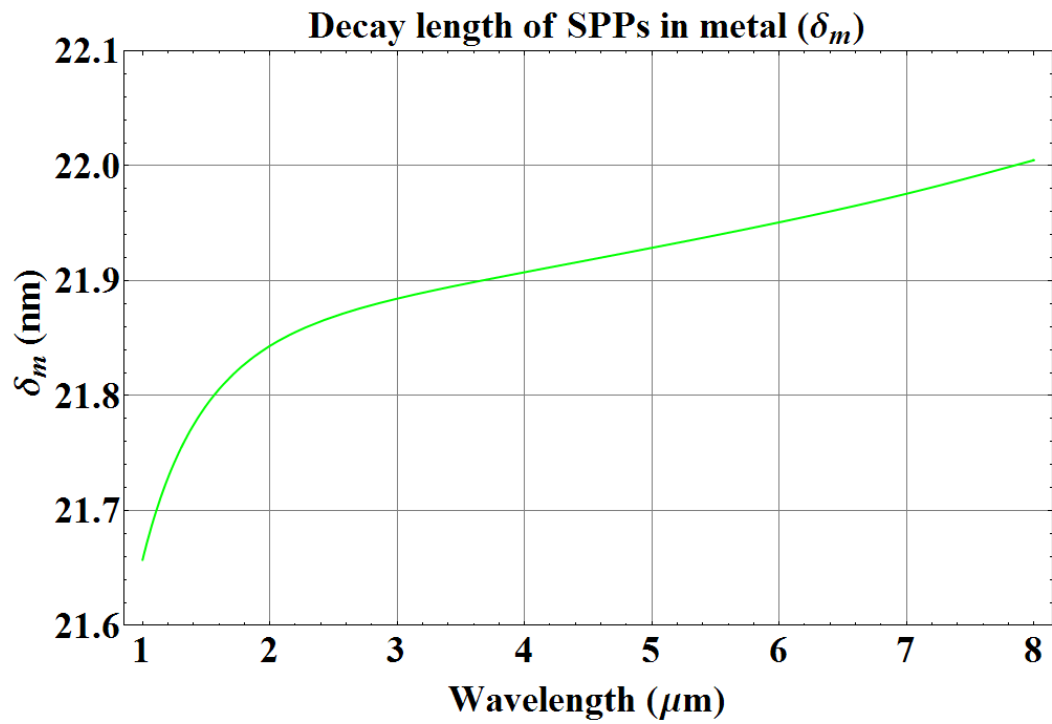
$$L_{sp} = \frac{1}{2 \times \text{Im}[k_{xd}]} = \frac{1}{2 \times \text{Im}[k_{xm}]} \quad (2.38)$$

where k_{xd} and k_{xm} can be calculated from Eq. (2.31).

Figs. (2.2) show the examples of calculations results of Eqs. (2.36) - (2.38), the dielectric material is SiO₂ and the metal is Ag. All optical constants come from Ref. [52, 60, 61].



(a)



(c)

Fig. 2.2 Decay lengths of SPPs (a) in the dielectric δ_d , (b) in the metal δ_m and (c) along the interface (L_{sp}). The dielectric is SiO_2 and the metal is Ag.

2.1.2 Surface plasmon polaritons at a smooth metal/dielectric/metal tri-layer structure

Fig. 2.3 (a) shows a typical symmetric metal/dielectric/metal (MDM) tri-layer structure. There is no TE mode SPPs in the MDM structure [62]. Consider SPPs of TM mode, the magnetic fields distributions are described as follows.

For $z \geq \frac{w}{2}$

$$H_y(x, z, \omega) = A_m e^{-k_m z} e^{i(k_{xm}x - \omega t)} \quad (2.39)$$

For $z \leq -\frac{w}{2}$

$$H_y(x, z, \omega) = A_m e^{k_m z} e^{i(k_{xm}x - \omega t)} \quad (2.40)$$

For $-\frac{w}{2} \leq z \leq \frac{w}{2}$

$$H_y(x, z, \omega) = A_d e^{k_d z} e^{i(k_{xd}x - \omega t)} + B_d e^{-k_d z} e^{i(k_{xd}x - \omega t)} \quad (2.41)$$

The definitions and characteristics of H_x , H_z , k_{xd} , k_{xm} , k_d and k_m are identical as what were defined in Sec. 2.1.1.2.

Substituting Eqs. (2.39) - (2.41) into Maxwell equation $\nabla \times \vec{H} = j\omega\epsilon_0\epsilon_r\vec{E}$, the magnetic fields of both regions can be derived

For $z \geq \frac{w}{2}$

$$E_x(x, z, \omega) = iA_m \frac{1}{\omega\epsilon_0\epsilon_{rm}} k_m e^{ik_{xm}x} e^{-k_m z} \quad (2.42)$$

$$E_z(x, z, \omega) = -A_m \frac{k_{xd}}{\omega\epsilon_0\epsilon_{rm}} e^{ik_{xm}x} e^{-k_m z} \quad (2.43)$$

For $z \leq -\frac{w}{2}$

$$E_x(x, z, \omega) = -iA_m \frac{1}{\omega \epsilon_0 \epsilon_{rm}} k_m e^{ik_{xm}x} e^{k_m z} \quad (2.44)$$

$$E_z(x, z, \omega) = -A_m \frac{k_{xm}}{\omega \epsilon_0 \epsilon_{rm}} e^{ik_{xm}x} e^{k_m z} \quad (2.45)$$

and for $-\frac{w}{2} \leq z \leq \frac{w}{2}$

$$E_x(x, z, \omega) = -iA_d \frac{1}{\omega \epsilon_0 \epsilon_{rd}} k_d e^{ik_{xd}x} e^{k_d z} + iB_d \frac{1}{\omega \epsilon_0 \epsilon_{rd}} k_d e^{ik_{xd}x} e^{-k_d z} \quad (2.46)$$

$$E_z(x, z, \omega) = -A_d \frac{k_{xd}}{\omega \epsilon_0 \epsilon_{rd}} k_d e^{ik_{xd}x} e^{k_d z} - B_d \frac{k_{xd}}{\omega \epsilon_0 \epsilon_{rd}} k_d e^{ik_{xd}x} e^{-k_d z} \quad (2.47)$$

The following boundary conditions of Maxwell equations should be satisfied at the interface ($z = \pm \frac{w}{2}$ respectively)

$$H_y \text{ continuity Eq. (2.39) = Eq. (2.41)} \quad (2.48)$$

$$\text{Eq. (2.40) = Eq. (2.41)} \quad (2.49)$$

$$E_x \text{ continuity Eq. (2.42) = Eq. (2.46)} \quad (2.50)$$

$$\text{Eq. (2.44) = Eq. (2.46)} \quad (2.51)$$

$$D_z \text{ continuity Eq. (2.43) } \times \epsilon_0 \epsilon_{rd} = \text{Eq. (2.47) } \times \epsilon_0 \epsilon_{rm}, \quad (2.52)$$

$$\text{Eq. (2.45) } \times \epsilon_0 \epsilon_{rd} = \text{Eq. (2.47) } \times \epsilon_0 \epsilon_{rm} \quad (2.53)$$

Solving Eqs. (2.48) - (2.53) yields

$$k_{xd} = k_{xm} \quad (2.54)$$

$$\text{Exp}[-k_d w] = \frac{k_d / \epsilon_{rd} + k_m / \epsilon_{rm}}{k_d / \epsilon_{rd} - k_m / \epsilon_{rm}} \quad (2.55)$$

Eq. (2.55) is the *dispersion relation* of SPPs in symmetric MDM tri-layer structures.

Theoretically, k_d , k_m , k_{xd} and k_{xm} can be described in terms of ε_{rd} , ε_{rm} and w by solving Eq. (2.55) with Eqs. (2.28), (2.29) and (2.54) since four variables can be solved using four equations. However, it should be note that $\text{Exp}[-k_d w]$ in Eq. (2.55) is an infinite series so that the solutions of k_d , k_m , k_{xd} and k_{xm} are infinite series either. These kind of solutions are too complex to use directly in the future sections and chapters.

Fortunately, S. Collin et al. [63] had point out that if

$$\delta_d = \frac{1}{\text{Re}[k_d]} \gg w \quad (2.56)$$

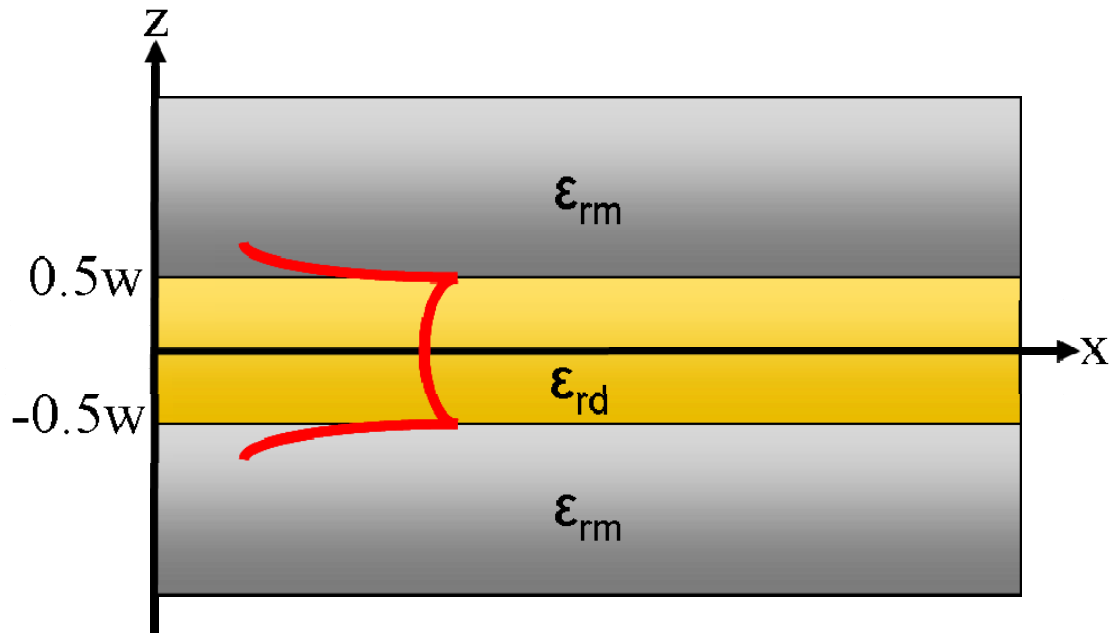
is satisfied, the SPPs in the two interfaces will couple together tightly as shown as the red lines in Fig. 2.3 (a). Once this tightly coupling occurs, the original tri-layer structure can be approximated to the two layer equivalent structure as shown in Fig.

2.3 (b). The refractive index of this effective dielectric is [63]

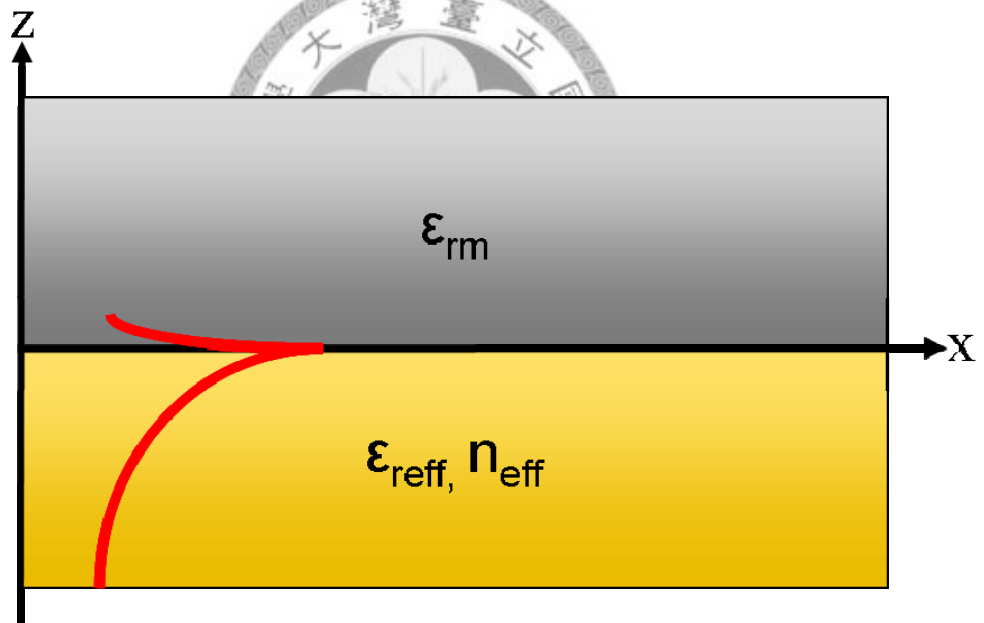
$$n_{\text{eff}} = \sqrt{\varepsilon_{\text{reff}}} = \sqrt{\varepsilon_{rd}} \times \left(1 + \frac{\lambda_0}{\pi w \sqrt{-\varepsilon_{rm}}} \sqrt{1 + \frac{\varepsilon_{rd}}{-\varepsilon_{rm}}} \right)^{1/2} \quad (2.57)$$

where $\varepsilon_{\text{reff}}$ is the effective relative dielectric constant, λ_0 is the wavelength of SPPs in the vacuum. Now, all formulas derived in Sec. 2.1.1.2 can be applied into Fig.

2.3 (b), and k_{xd} , k_{xm} , k_d and k_m of original MDM structure can be obtained easily by substituting Eq.(2.57) into Eqs. (2.31) - (2.33).



(a)



(b)

Fig. 2.3 (a) The metal/dielectric/metal (MDM) tri-layer structure, the thickness of dielectric is w . The red lines represent the intensity of SPPs of two interfaces and will couple together once Eq. (2.56) is satisfied; (b) the simpler equivalent structure of Fig. 2.3 (a) once Eq. (2.56) is satisfied.

2.2 Excitation of surface plasmon polaritons

The field distributions and dispersion curves of SPPs had been introduced in the previous sections without considering how the waves are generated or excited. Of course, SPPs are excited from some kind of methods [58], such as prisms coupling, near field scatterings and gratings coupling. Only gratings coupling will be discussed and used in this thesis.

For simplicity, consider y-polarized waves (TM mode) impinge on a one dimensional arbitrary shaped interface whose period is Λ as shown in Fig. 2.4. The coordination (x, z) of interface in space is $(x, h(x))$ where $h(x)$ is in period of Λ . The blue lines indicate the incident waves with common propagation directions (common k_{ix} and k_{iz}); the green lines and red lines represent the reflection and the transmission waves, respectively. Since the propagation directions of reflection and transmission waves may be different at each point of the interface, the final electromagnetic waves in any point of space (x, z) should be the superposition of waves come from all directions. Interference occurs and some of waves are canceled.

The theorem of gratings coupling which are based on linear algebra [Appendix, 64, 65] states that the final distributions of reflection waves and transmission waves can be spanned in the basis of infinite waves whose wavesvectors are discrete

$$\vec{H}_r(x, z) = \sum_{m=-\infty}^{+\infty} R_m e^{i(k_{rx}x + k_{rz}z)} \vec{y} \quad (2.58)$$

$$\vec{H}_l(x, z) = \sum_{m=-\infty}^{+\infty} T_m e^{i(k_{ix}x - k_{iz}z)} \vec{y} \quad (2.59)$$

$$k_{rx} = k_{ix} = k_x = k_{ix} + m \frac{2\pi}{\Lambda} \quad (2.60)$$

where m denotes the order of scattering waves.

Since

$$k_{rx}^2 + k_{rz}^2 = k_0^2 \mu_{r1} \varepsilon_{r1} \quad (2.61)$$

$$k_{tx}^2 + k_{tz}^2 = k_0^2 \mu_{r2} \varepsilon_{r2} \quad (2.62)$$

should be obeyed for all kinds of waves, large $\left| m \frac{2\pi}{\Lambda} \right|$ will enlarge k_{rx}^2 and k_{tx}^2 in

Eq. (2.60). Next, large k_{rx}^2 and k_{tx}^2 make negative k_{rz}^2 and k_{tz}^2 in Eq. (2.61)

and (2.62). Finally, k_{rz} and k_{tz} become imaginary number, the reflecting waves and

transmission waves in Eq. (2.58) and (2.59) become evanescent waves

$$\vec{H}_r^m(x, z) = R_m e^{i(k_{rx}x + k_{rz}z)} \vec{y} = R_m e^{ik_{rx}x} e^{-|\text{Im}[k_{rz}]z} \vec{y} \quad z \leq h(x) \quad (2.63)$$

$$\vec{H}_t^m(x, z) = T_m e^{i(k_{tx}x - k_{tz}z)} \vec{y} = T_m e^{ik_{tx}x} e^{+|\text{Im}[k_{tz}]z} \vec{y} \quad z \geq h(x) \quad (2.64)$$

Eq. (2.63) and (2.64) indicate that the scattering waves for large $\left| m \frac{2\pi}{\Lambda} \right|$ are

surface waves. These waves can be SPPs if medium 1 is dielectric and medium 2 is

metal. Let Eq. (2.60) = Eq. (2.31), the momentum conservation law used to excite

SPPs is obtained

$$k_{sp} = k_{ix} + m \frac{2\pi}{\Lambda} \quad (2.65)$$

where $k_{sp} = k_0 \sqrt{\frac{\varepsilon_{rd} \times \varepsilon_{rm}}{\varepsilon_{rd} + \varepsilon_{rm}}} = \frac{\omega}{c} \sqrt{\frac{\varepsilon_{rd} \times \varepsilon_{rm}}{\varepsilon_{rd} + \varepsilon_{rm}}}$.

Finally, since $\frac{2\pi}{\Lambda}$ is the reciprocal unit vector of 1D gratings according to solid state physics [59], Eq. (2.60) and (2.65) can be extended to the 2D grating in the form

$$\vec{k}_{r//} = \vec{k}_{t//} = \vec{k}_{i//} + i\vec{G}_x + j\vec{G}_y \quad (2.66)$$

$$\vec{k}_{sp} = \vec{k}_{i//} + i\vec{G}_x + j\vec{G}_y \quad (2.67)$$

where i, j are any integers, \vec{G}_x and \vec{G}_y are the reciprocal unit vectors of the grating.

$\vec{k}_{r//}$, $\vec{k}_{t//}$ and $\vec{k}_{i//}$ are the parallel component of the wavevector of reflection, transmission and incident light along the interface.

Eq. (2.67) is the momentum conservation law used to excite SPPs which will be used in chapter 3; Eq. (2.66) is the general momentum conservation law which will be utilized and discussed in chapter 4.

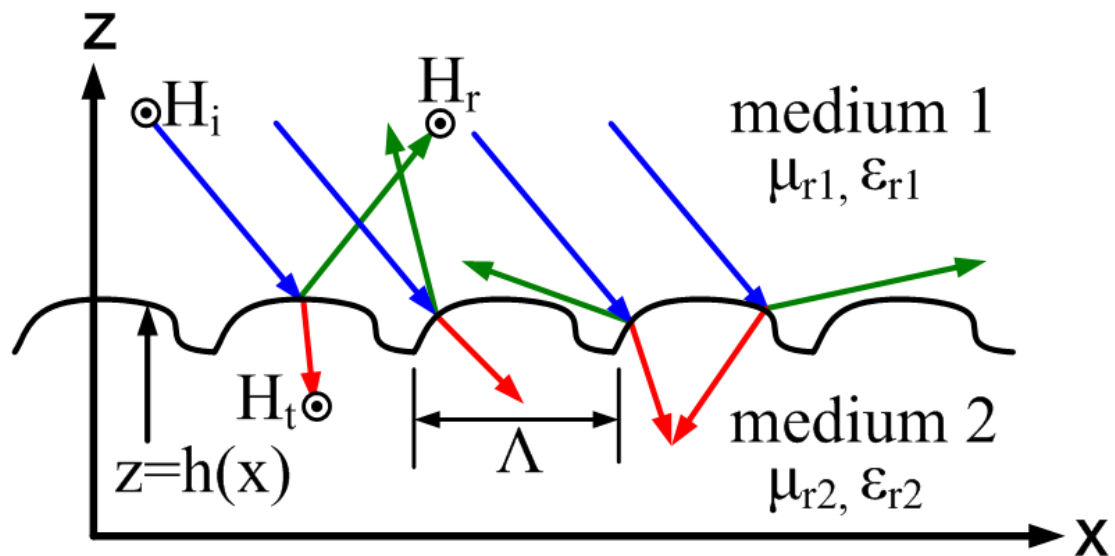


Fig. 2.4 Parallel polarization plane waves (TM mode) impinge on the one dimensional grating whose period is Λ . The blue lines, green lines and red lines represent the incident lights, reflection lights and transmission lights respectively.

2.3 The extraordinary light transmission and infrared thermal emitters

2.3.1 Extraordinary light transmission

Extraordinary transmission (EOT) of light discovered by Ebbesen in 1998 [2] is due to the SPPs. Consider a light is incident on a silicon substrate with a silver film on top perforated with hole array arranged in a rhombus lattice as shown in Fig. 2.5 (a) and (b) along the ΓK direction as defined in Fig. 2.5 (b). First, the incident lights is scattered by periodic structure and couple to the SPPs at interface according to Eq. (2.67). Next, the SPPs propagate along the interface and meet the holes. The SPPs tunnel through the holes and propagate along the outer interface. Finally, the SPPs on the outer interface reemit to the far field via scattering by periodic structure. The final transmission ratio of light is enhanced by the excitation of SPPs and tunneling process [36, 37].

The peaks of EOT can be calculated by Eq. (2.67) where $\vec{k}_{//} = |\vec{k}_0| \sin \varphi \vec{x}$, $|\vec{k}_0| = \frac{2\pi}{\lambda_0}$ is the wavevector of input light and output light; λ_0 is the wavelength in vacuum and θ is the incident angle as shown Fig. 2.5 (a). Detailed calculations and discussions will be given in chapter 3.

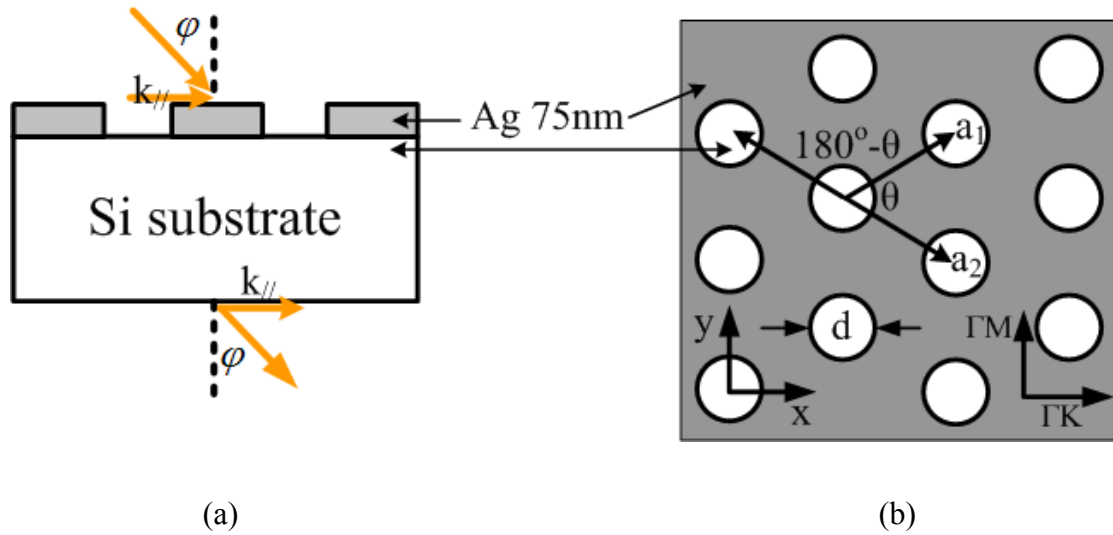


Fig. 2.5 The (a) side and (b) top view of a silicon substrate with a silver film on top perforated with hole array arranged in a rhombus lattice. φ is the incident and transmission angle, $k_{//}$ is the light wave vector component parallel to the sample surface along ΓK direction.



2.3.2 Infrared thermal emitters

Fig 2.6 displayed an infrared thermal emitter [38-41], Mo acts as a resistor. Once the current is passed through the Mo layer, the device is heated and the SPPs which are electromagnetic waves will be generated in the interface of Ag/SiO₂ by blackbody radiation and will couple back to the propagation waves if their wavevectors satisfy Eq. (2.67). The emission peaks can be calculated by Eq. (2.67) where $\vec{k}_{ix} = |\vec{k}_0| \sin \varphi \vec{x}$, $|\vec{k}_0| = \frac{2\pi}{\lambda}$ is the wavevector of the *incident light*; λ is the wavelength in vacuum, and θ is the incident angle. However, since Ag/SiO₂/Ag is a

tri-layer structure, the effective refractive index from Eq. (2.57) should be used in calculation. Detailed calculations and discussions will be given in chapter 3 and 4.

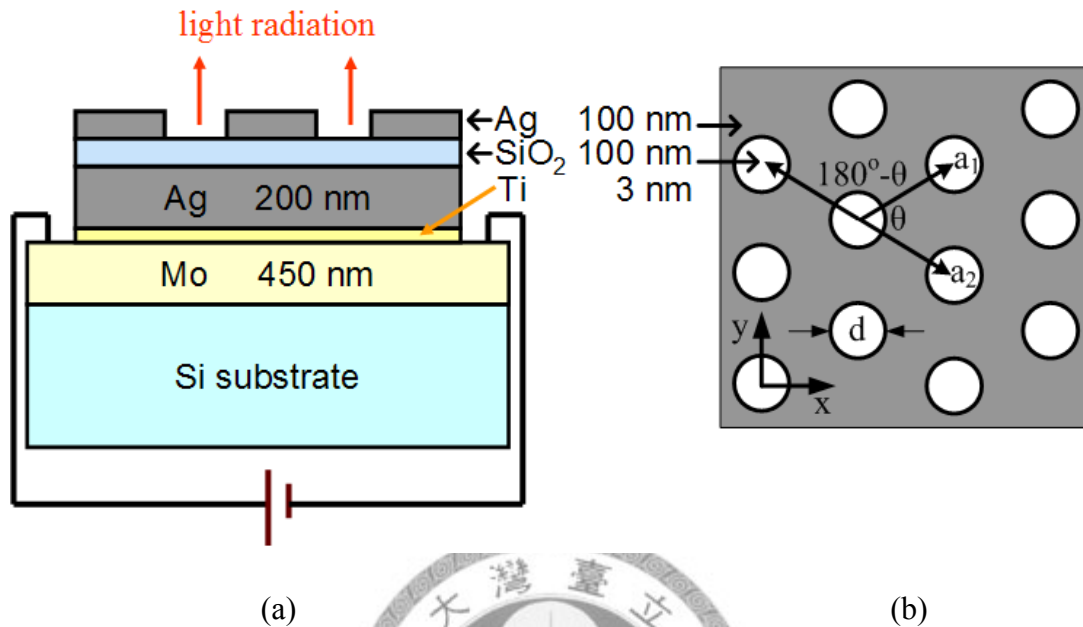


Fig. 2.6 (a) The side view and (b) top view of infrared thermal emitters.

2.4 Process flow

2.4.1 Fabrication processes of samples of metal hole arrays

(1) Surface cleaning

Cleaning is required to remove the undesired materials from the wafer surface. This is performed before all other processing steps to increase the reliability and performance of the device. These steps may employ organic solvents, vapor degreasing, and acids. The organic solvents were used to remove oils, greases, particles and organic material such as photoresists and to keep the surface clean. Table

2.1 lists the cleaning conditions and purposes of the solvent.

Table 2.1 Conditions and purposes of the cleaning solvents

Chemical Solution	Clean Time (min)	Purposes
Acetone (CH ₃ COCH ₃)	5	Clean photoresist, organic materials
Methanol (CH ₃ OH)	5	Clean Acetone
D.I water (H ₂ O)	5	Clean Methanol

(1) Photolithography

NR9-1000PY negative photoresist was spun and coated on the silicon wafer. Soft baking 1 minute is used to evaporate solvent contained in photoresist. The exposure system is the Karl Suss MJB3 Mask Aligner with 365 nm UV light. After the exposure, 2 minute and 30 seconds post-exposure bake is required. RD-6 development solution was used to remove the unexposed portion of negative photoresist. Table 2.2 lists the photolithography conditions.

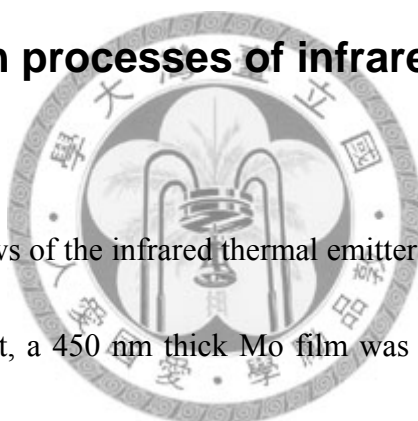
(3) Lift-off process

After thermally evaporating a layer of metal on the Si wafer with a patterned photoresist, remover 1165 which is an etchant, was used to lift-off the metal with the photoresist below. Then the periodic metal hole arrays are achieved.

Table 2.2 The photolithography conditions

Pattern Formation	Negative Photoresistor
Spinning and Coating	4000 rpm 40 sec
Soft Bake	150°C 1min
Exposure	50 sec
Post-Exposure Bake	100°C 2min 30sec
Development	4 sec

2.4.2 Fabrication processes of infrared thermal emitters



The side and top views of the infrared thermal emitters are depicted in Fig. 2.5(a) and (b), respectively. First, a 450 nm thick Mo film was deposited by sputtering on the Si substrate as a heating source. 3 nm Ti layer and 200 nm Ag metal films were deposited on the front side of the Si substrate followed by a 100nm SiO₂ layer deposited with electron beam evaporator. After photolithography a negative photoresist layer were patterned with grating array. Then a 100 nm Ag Film was deposited on to the patterned photoresist layer and lifted off to complete the processes. The pattern area of the sample is 1 x 1 cm².

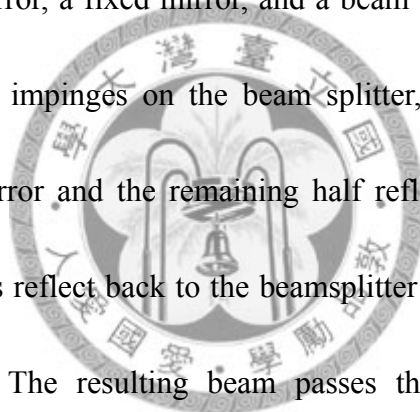
Finally, the fabrication processes of infrared thermal emitters used in chapter 4 are a little different than Fig. 2 and will be discussed later in chapter 4.

2.5 Measurement systems

2.5.1 Introduction of FTIR

Fourier Transform Infrared (FTIR) spectrometers are efficient instruments to measure the whole spectral response of samples in the infrared. The spectral response can be obtained simultaneously in one measurement in few seconds. The kernel of FTIR spectrometers are the Michelson interferometer.

Fig. 2.7 shows the schematic of the FTIR spectrometer. It consists of three active components a moving mirror, a fixed mirror, and a beam splitter. The radiation from the broadband IR source impinges on the beam splitter, and half of the IR beam transmits to the fixed mirror and the remaining half reflects to the moving mirror. Then those divided beams reflect back to the beamsplitter and recombine to generate the interference pattern. The resulting beam passes through sample and finally impinges upon the detector. First, consider a frequency f' component of IR source. The intensity of the interfered beam depends on the optical path difference between two split beams. The inset in Fig. 2.7 is the “interferogram”, which is the record of the interference signal. When the moving mirror is moved with a constant velocity, the intensity of radiation reaching the detector is a sinusoidal manner. The intensity of the sinusoidal wave will be reduced if the sample absorbs in this frequency f' . Then, the summation of superimposed sinusoidal waves is taken, each wave corresponding to a



signal frequency, to get the whole interference patterns [66].

The interferogram is a time domain spectrum. By using the Fourier transformation, the interferogram can be converted into a frequency domain spectrum to show the intensity as a function of frequency.

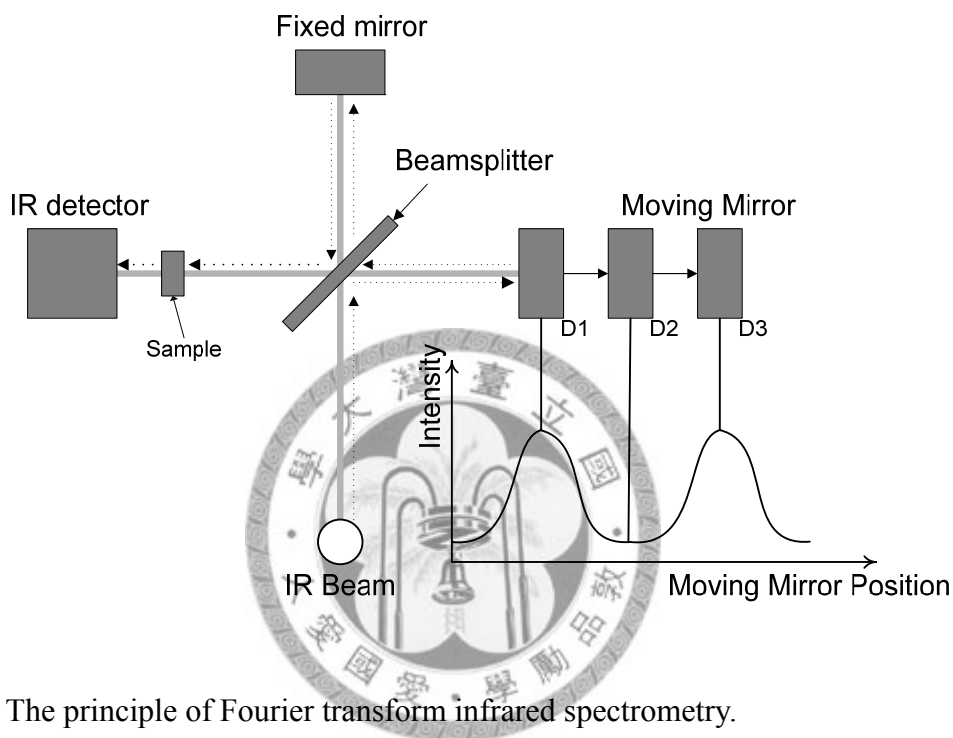


Fig. 2.7 The principle of Fourier transform infrared spectrometry.

2.5.2 Transmission measurement

A Bruker IFS 66 v/s system was adapted to measure the transmission spectra.

The red line is the optical path of measurement and the sample is placed in the middle with incline angle φ as shown in Fig. 2.5 (a). The wavenumber resolution of the measurement is 8 cm^{-1} . The beam size of incident infrared light is 3 mm.



Fig. 2.8 The experiment setup of transmission at incline incidence.

2.5.3 Reflection measurement

A PERKIN ELMER 2000 Fourier Transform Infrared Spectrometer (FTIR) was used to measure thermal radiation spectra above the samples with incline angle φ as defined Fig. 2.9. The wavenumber resolution of the measurement is 8 cm^{-1} . The beam size of incident infrared light is 3 mm. The entire system is shown in Fig. 2.10. Sample is lain down in the holder in the center of the system. Arms A and B with reflection mirrors can rotate from 12° to 65° with respect to the normal direction of sample surface. Incident light is first reflected by mirror A and impinges on the measurement sample. The reflection light from sample is then reflected by mirror B and goes out to the detector. The light path is displayed in Fig. 2.10 as red dashed lines.

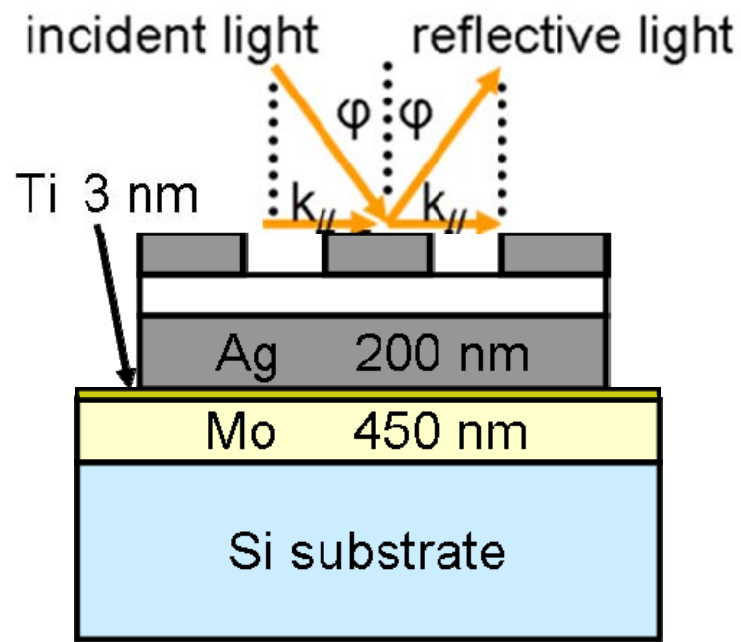


Fig. 2.9 Schematic diagram of reflection measurement in the angle ϕ from 12° to 65° .

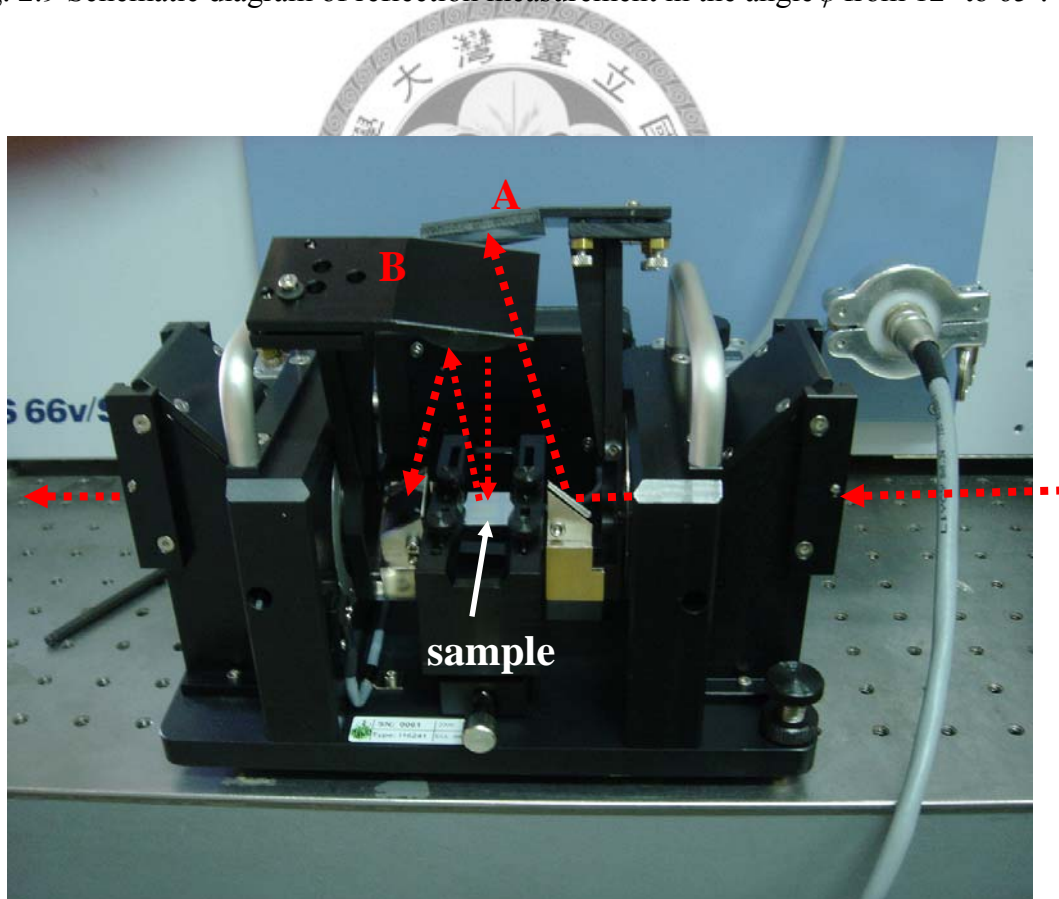
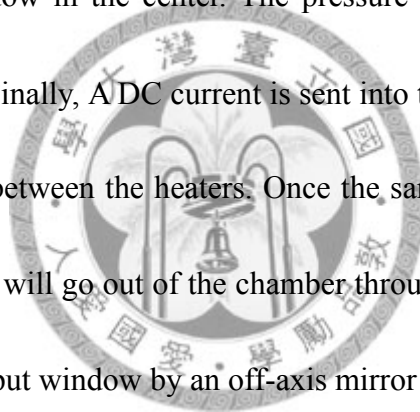


Fig. 2.10 The optical path and reflection mirrors of reflection measurement

2.5.4 Thermal emission measurement

A Perkin Elmer 2000 Fourier transform infrared spectrometer (FTIR) was adopted to measure the radiation spectra of thermal emitters. The wave number resolution of the measurement is 8 cm^{-1} . The radiation area of the sample is 1 cm^2 . The infrared thermal emitters which are shown in Fig. 2.9 are placed in the vacuum chamber as shown in Fig. 2.11 (a). A thermal couple is put on the top of the sample in order to measure the exact temperature on the surface. Next, the chamber is closed by a cover with a KBr window in the center. The pressure of the chamber is pumped down to about 2×10^{-3} . Finally, A DC current is sent into the heaters and heats up the sample which is clipped between the heaters. Once the sample is heated, the thermal radiation from the sample will go out of the chamber through the KBr window and be reflected into the FTIR input window by an off-axis mirror as shown in Fig. 2.11 (b).



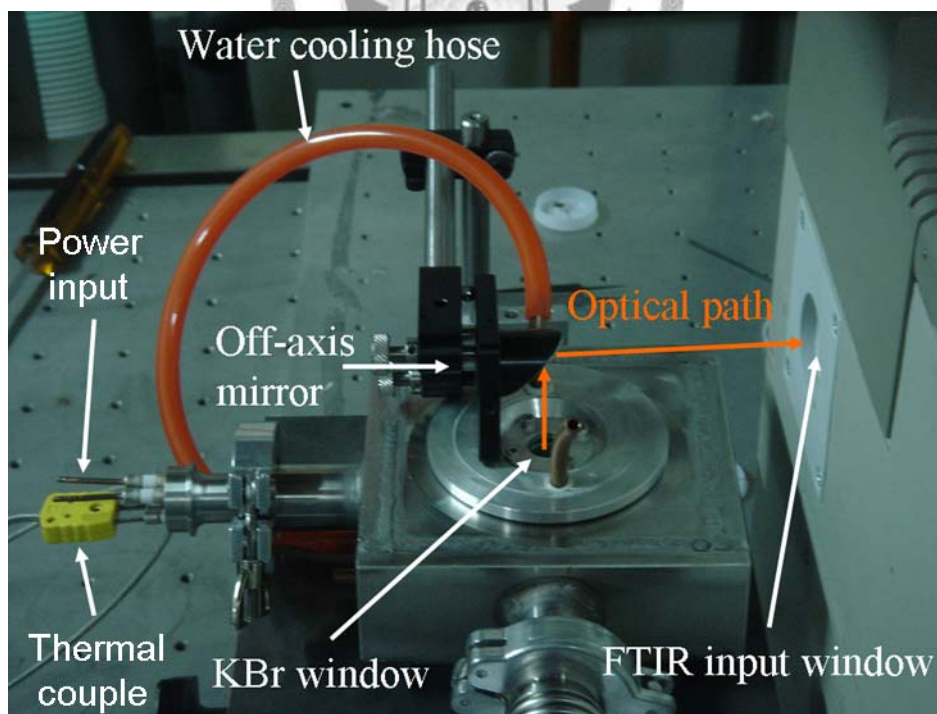
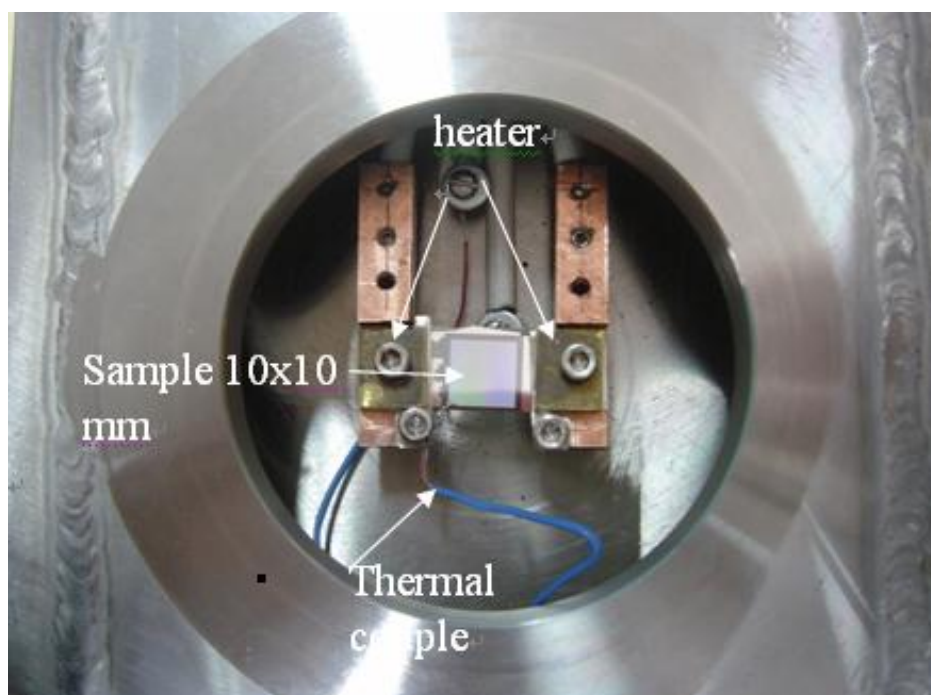
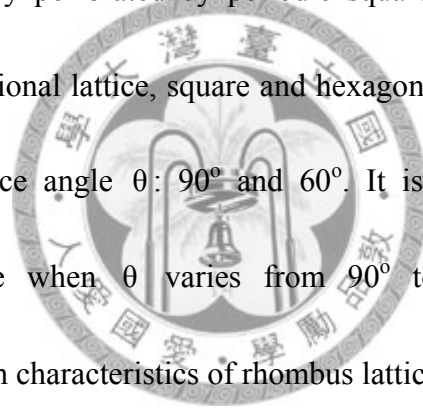


Fig. 2.11 The thermal emitter chamber, (a) top view (b) side view.

Chapter 3 Extraordinary transmission through a silver film perforated with hole arrays arranged in a rhombus lattice and its application in plasmonic thermal emitters

Metal/thin-dielectric/metal plasmonic thermal emitters which were first reported by Tsai et al. [38-41] had been proved to be able to realize the tunable mid-infrared light source with narrowband, high temperature operation and high output intensity. The top metal is typically perforated by periodic square or hexagonal hole array. However, for two dimensional lattice, square and hexagonal lattices are just rhombus lattice with specific lattice angle θ : 90° and 60° . It is interesting to know how emission spectra change when θ varies from 90° to 40° by 10° step. The extraordinary transmission characteristics of rhombus lattice are also investigated.



3.1 Extraordinary transmission through a silver film perforated with hole array arranged in a rhombus lattice

3.1.1 Experiments

A silicon substrate with a silver film on top perforated with hole array arranged in a rhombus lattice are shown in Fig. 3.1. Six samples A to F with lattice angle θ varying from 40° to 90° were prepared for experiments and their structure parameters

are summarized in Table 3.1. It should be noted that sample C is a hexagonal lattice and sample F is a square lattice. Besides, θ and $180^\circ-\theta$ denotes the same lattice structure.

The fabrication procedures were described in Sec. 2.4.1. After fabrication, the samples were placed in the Bruker IFS 66 v/s system to measure the transmission spectra with the same incident and transmission angles φ from 0° to 65° in 1° step along the ΓK direction as defined in Fig. 3.1 (b).

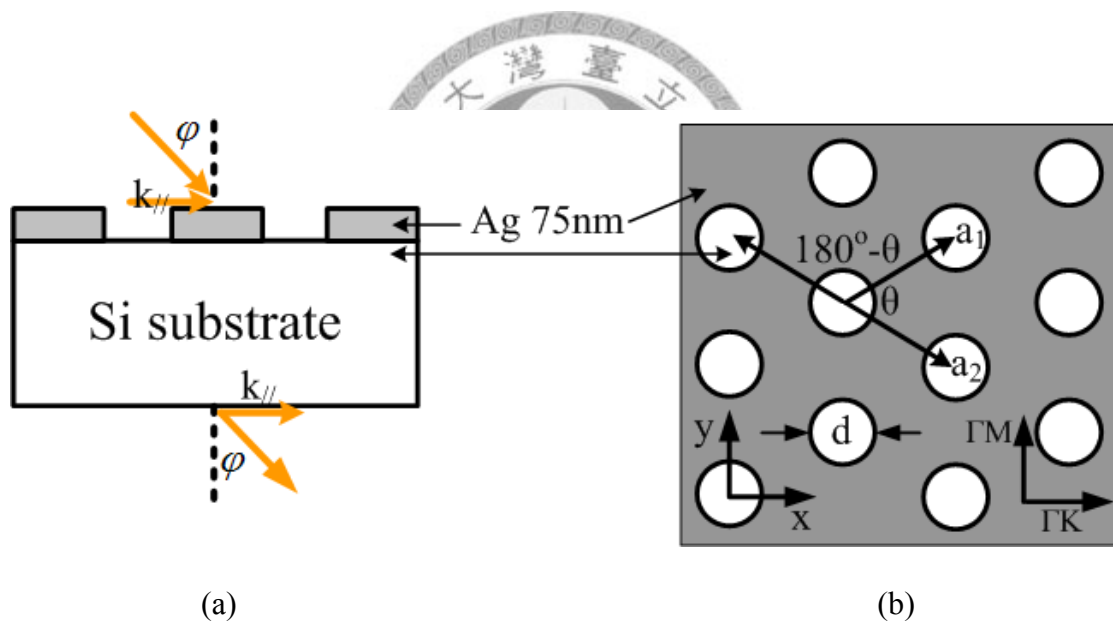


Fig. 3.1 The (a) side and (b) top view of a silicon substrate with a silver film on top perforated with hole array arranged in a rhombus lattice. $|\vec{a}_1| = |\vec{a}_2| = a = 5\mu\text{m}$ and $d = 2.5\mu\text{m}$. φ is the incident and transmission angle, $k_{||}$ is the light wave vector component parallel to the sample surface along ΓK direction.

Table 3.1 The structure parameters of samples A to F.

Sample	A	B	C	D	E	F
θ (degree)	40	50	60	70	80	90

3.1.2 Results and discussion

For a rhombus lattice whose unit vectors \vec{a}_1 and \vec{a}_2 are defined in Fig. 3.1 (b), their corresponding unit vectors in reciprocal lattice are given by [59]

$$\vec{G}_1 = (G_{1x}, G_{1y}) = \frac{\pi}{a} \times \left(\frac{1}{\cos \frac{\theta}{2}}, \frac{1}{\sin \frac{\theta}{2}} \right) \quad (3.1)$$

$$\vec{G}_2 = (G_{2x}, G_{2y}) = \frac{\pi}{a} \times \left(\frac{1}{\cos \frac{\theta}{2}}, \frac{-1}{\sin \frac{\theta}{2}} \right) \quad (3.2)$$

SPPs exist at the interfaces of Ag/Si and Ag/air, respectively, with dispersion relation from Eq. (2.31)

$$|\vec{K}_{sp}| = \frac{\omega}{c} \sqrt{\frac{\epsilon_{rd} \times \epsilon_{rm}}{\epsilon_{rd} + \epsilon_{rm}}} \quad (3.3)$$

where ω is the angular frequency of wave, c is the speed of light in vacuum, ϵ_{rm} and ϵ_{rd} are the relative dielectric constants of silver and dielectric (silicon or air for Ag/Si modes or Ag/air modes), respectively. SPPs would scatter with periodic hole array according to the momentum conservation laws from Eq. (2.67)

$$\vec{k}_{sp} = \vec{k}_{//} + i\vec{G}_1 + j\vec{G}_2 \quad (3.4)$$

where $\vec{k}_{//}$ is the wave vector of light parallel to sample surface as defined in Fig. 3.1

(a). i, j , are any integers;

When the light are incident along ΓK direction with incident angle φ shown in Fig. 3.1 (a), the parallel component of wave vectors $\vec{k}_{//}$ is given by

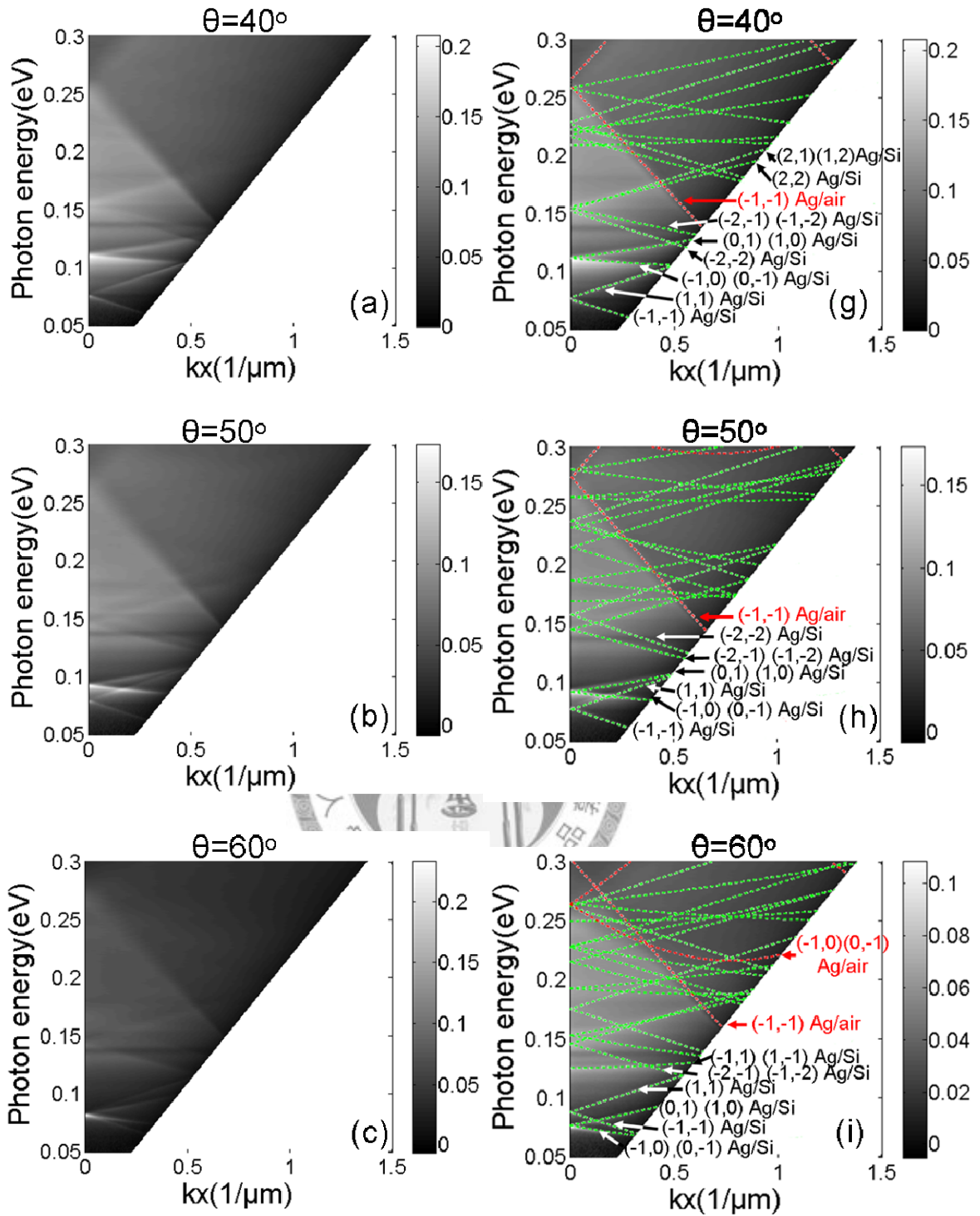
$$\vec{k}_{//}=(k_x,0,0)=(k_0 \times \text{Sin}\varphi,0,0) \quad (3.5)$$

where $k_0 = \frac{\omega}{c}$

Substituting Eqs. (3.1)-(3.3) and (3.5) into Eq. (3.4) yields

$$\frac{\omega}{c} \times \sqrt{\frac{\epsilon_{rd} \times \epsilon_{rm}}{\epsilon_{rd} + \epsilon_{rm}}} = \sqrt{(iG_{1x} + jG_{2x} + k_x)^2 + (iG_{1y} + jG_{1y})^2} \quad (3.6)$$

In the mid-infrared, $\text{Re}[-\epsilon_{rm}] \gg \epsilon_{rd}$ [52, 60, 61]. Using this approximation and ignoring the image part of ϵ_{rm} , Eq. (3.6) can be plotted on the dispersion relation diagram extracted from transmission spectra for comparison. Figs. 3.2 (a)-(f) and (g)-(l) show the measured and theoretical dispersion relation diagrams for samples A to F, respectively. The common dark horizontal lines in each diagram around 0.14eV is the Si phonon absorption modes [52]. The symbols (i,j) Ag/Si denoted in the figures represent the SPPs modes whose i, j satisfy Eq. (3.6) and $\epsilon_{rd} \approx 11.9$ is the relative dielectric constant of silicon; similarly, (i,j) Ag/air denote the SPPs modes whose i and j satisfy Eq. (3.6) and $\epsilon_{rd} = 1$ is the relative dielectric constant of air. The green and red dashed lines are the theoretical dispersion curves of Ag/Si and Ag/air modes according to Eq. (3.6), respectively. Compared Figs. 3.2 (a)-(f) with Figs. 3.2 (g)-(l),



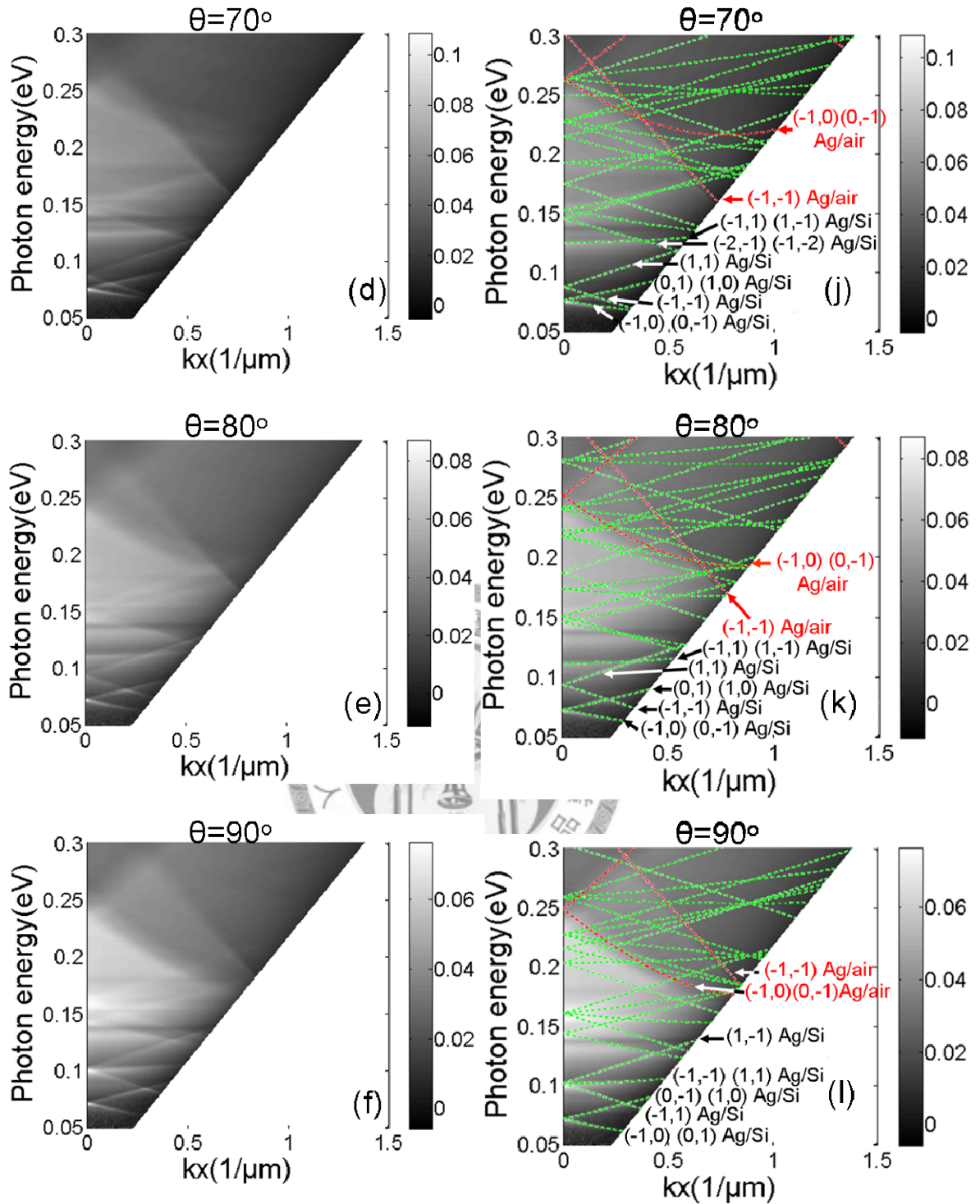
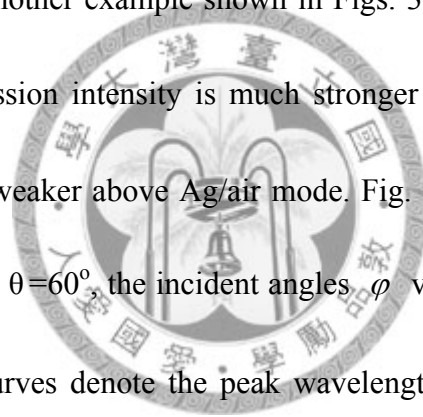


Fig. 3.2 The dispersion relation extracted from transmission spectra for samples (a) A, (b) B, (c) C, (d) D, (e) E, (f) F and their modes analyses for samples (g) A, (h) B, (i) C, (j) D, (k) E, (l) F. The green and red dashed lines are the calculated dispersion curves of Ag/SiO₂ and Ag/air modes, respectively.

highly agreements of theoretical and experimental curves are obtained. However, it can be noticed that the dispersion curves of Ag/air modes are the boundary curves for transmission intensity for all spectra, the transmission intensity would become stronger in the lower energy part below the Ag/air curves and weaker above the Ag/air curves. For example, in Figs. 3.2 (a) and (g) for sample A with $\theta=40^\circ$, it could be found that (-1,-1) Ag/air mode is the boundary line for transmission intensity, bright (2,1) (1,2) (2,2) Ag/Si modes becomes unclear in the spectra if their energy are higher than (-1,-1) Ag/air. For another example shown in Figs. 3.2 (d) and (j) for sample D with $\theta=70^\circ$, the transmission intensity is much stronger in the energy band below (-1,-1) Ag/air and much weaker above Ag/air mode. Fig. 3.3 shows the transmission spectra of sample C with $\theta=60^\circ$, the incident angles ϕ varies from 0° to 60° by 10° step, the black dashed curves denote the peak wavelengths of (-1,-1) Ag/air mode, there is almost no Ag/Si modes was found in the wavelength range shorter than (-1,-1) Ag/air mode.



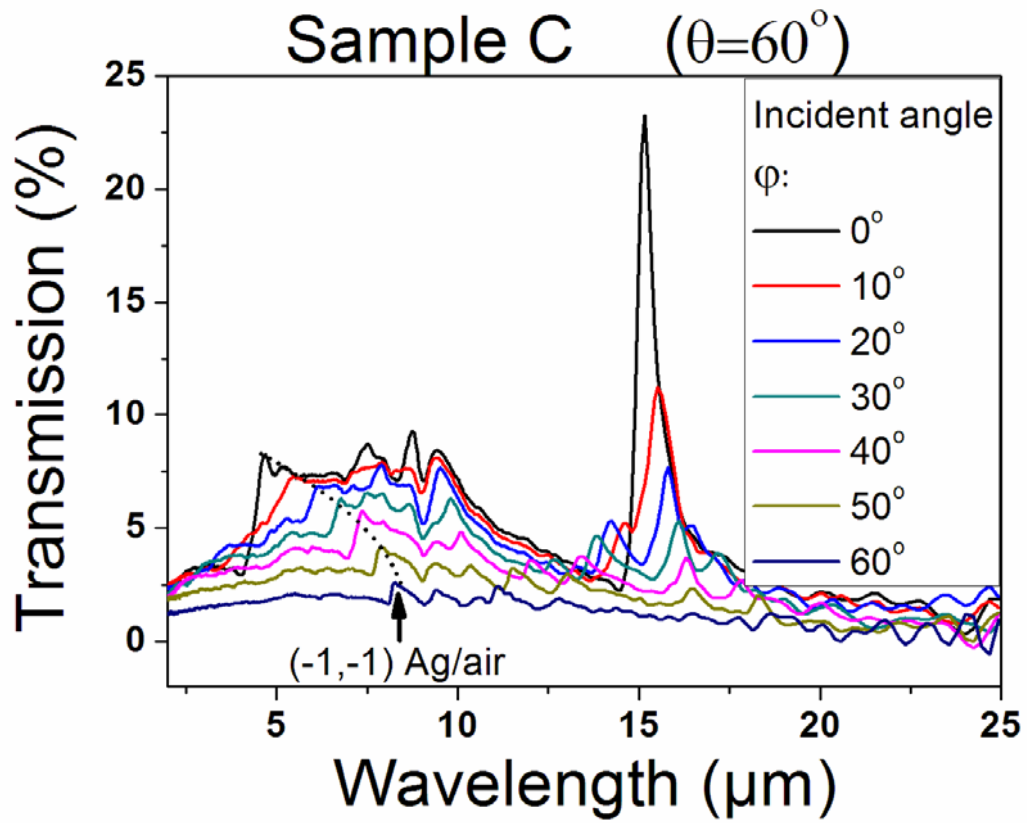


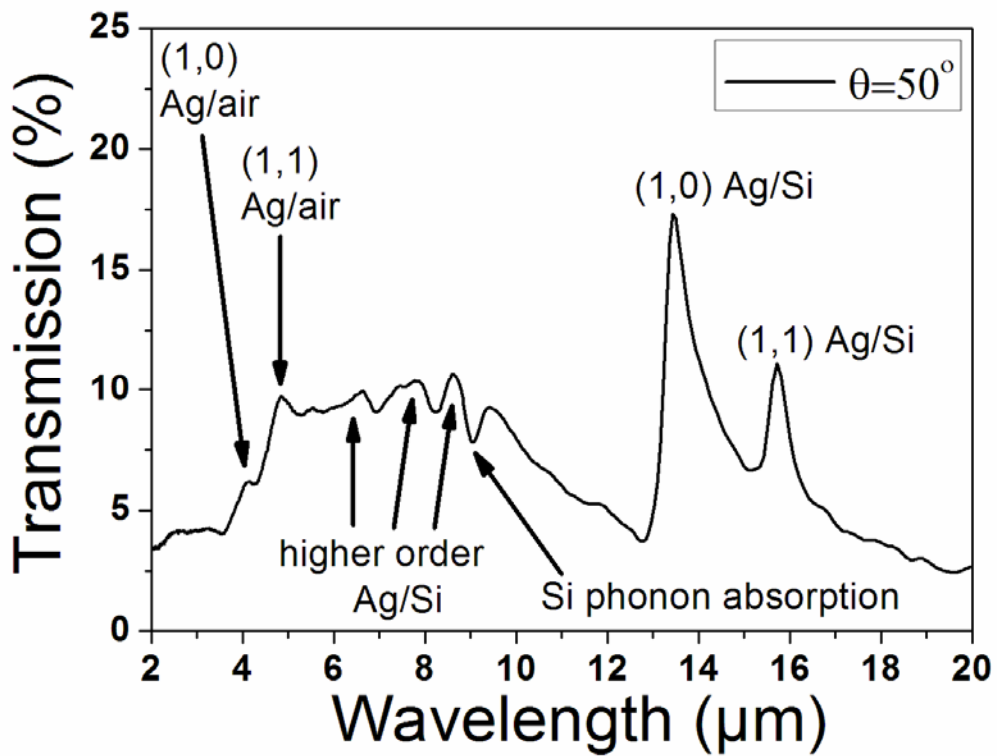
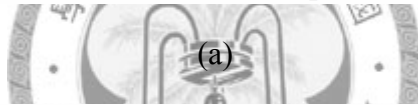
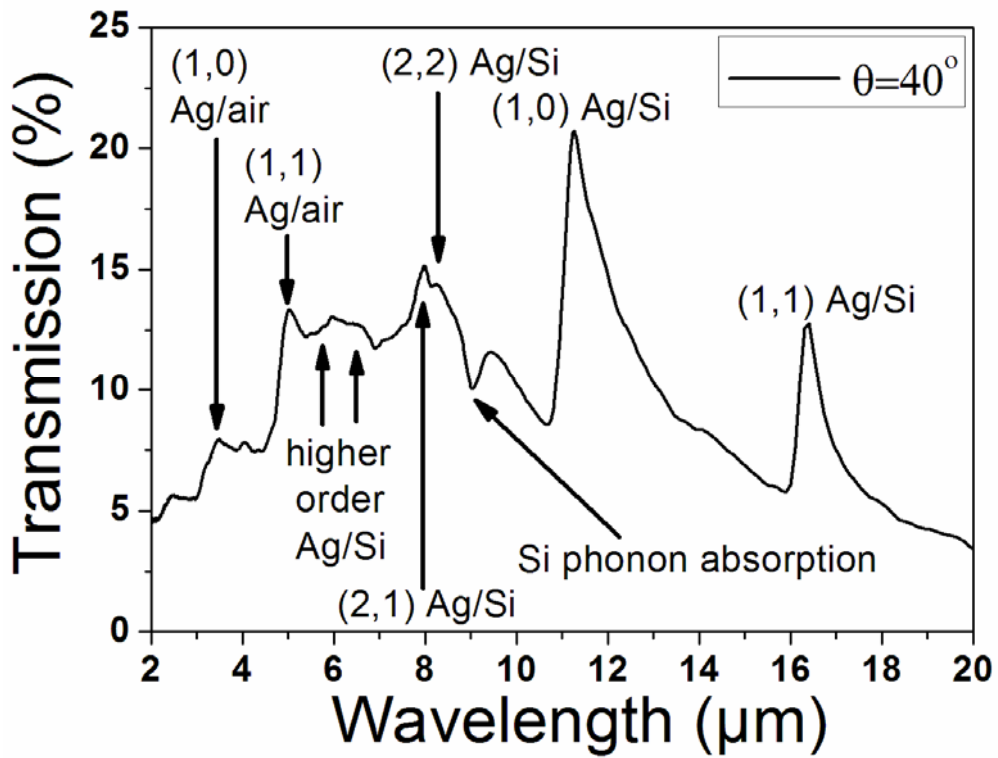
Fig. 3.3 The transmission spectra of sample C with incident angle ϕ varying from 0° to 60° by 10° step.



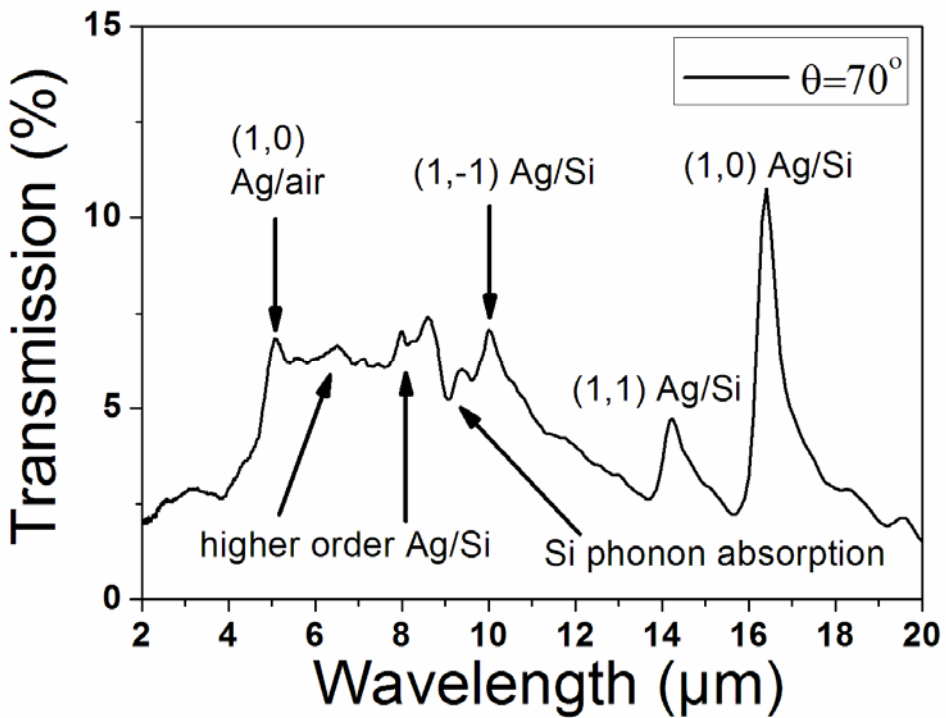
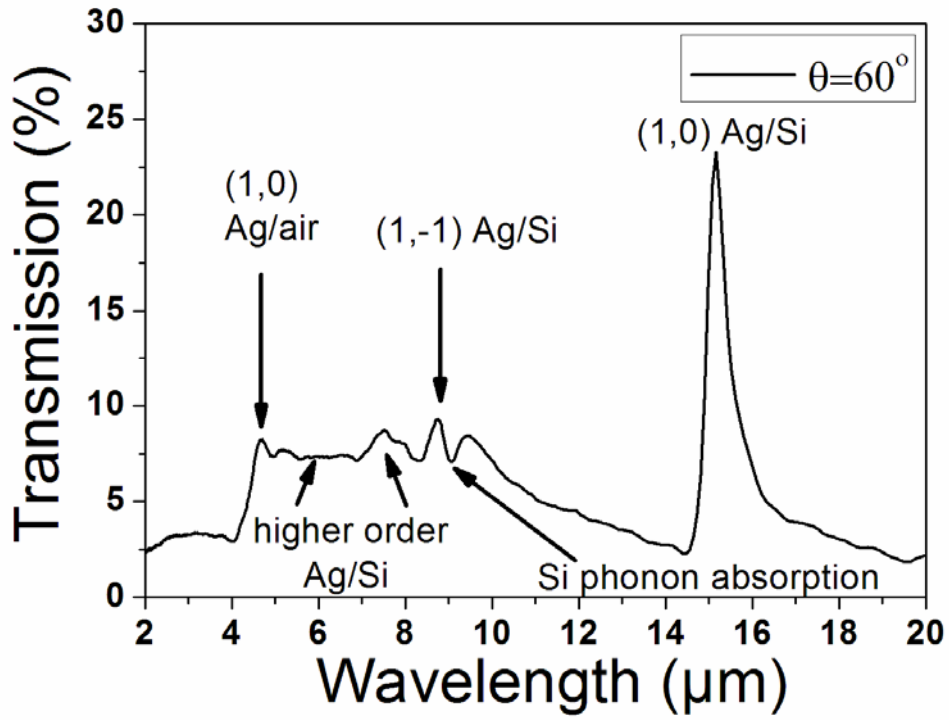
For normal incident angle $\varphi = 0^\circ$, Eqs. (3.5) and (3.6) can be simplified to

$$\lambda_0 = \frac{a \times \text{Sin}\theta}{\sqrt{i^2 + j^2 - 2 \times i \times j \times \text{Cos}\theta}} \times \sqrt{\varepsilon_{rd}} \quad (3.7)$$

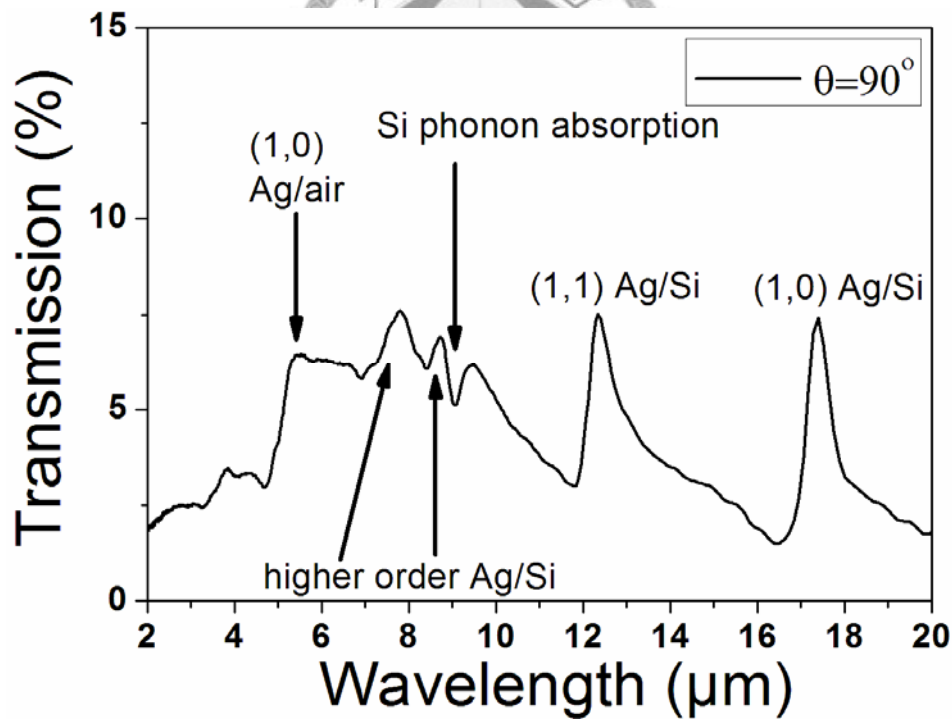
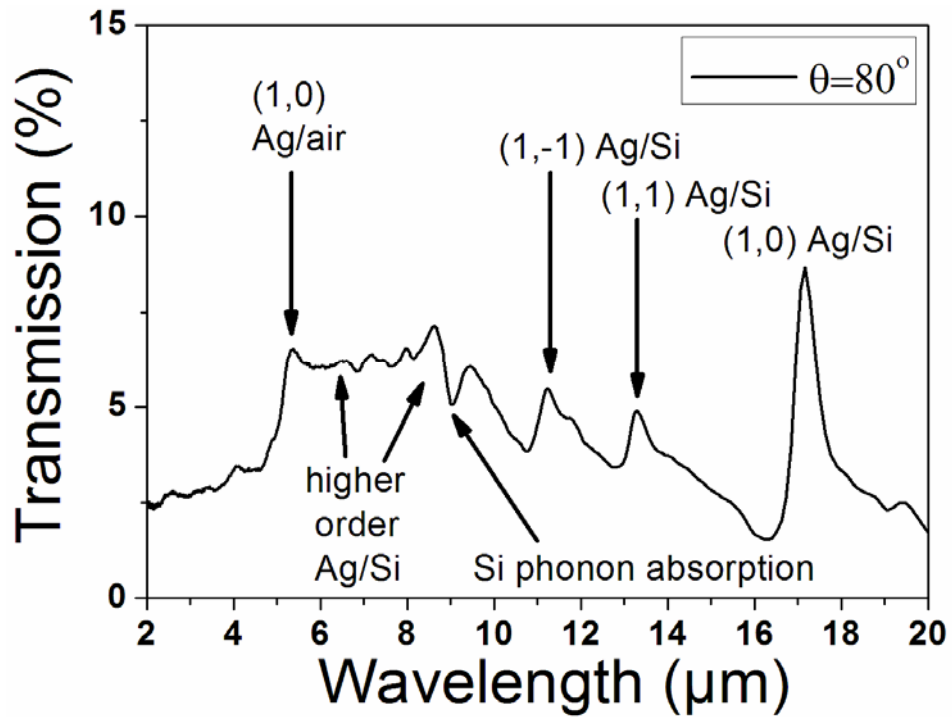
where λ_0 is the peak wavelengths of SPP. For (i,j) Ag/air modes, $\varepsilon_{rd} = 1$ and for (i,j) Ag/Si modes, $\varepsilon_{rd} \approx 11.9$. Figs. 3.4 (a)-(f) show the transmission spectra for samples A ($\theta = 40^\circ$) to F ($\theta = 90^\circ$) in the normal direction ($\varphi = 0^\circ$). The common deeps around $9 \mu\text{m}$ are the Si phonon absorption modes [52]. For each (i,j) Ag/air and (i,j) Ag/Si modes denoted in the Figs. 3.4, they are composed of two to six degenerated modes as indicated in Table 3.2. Table 3.2 also summarizes the measured transmission intensities, the theoretical and measured wavelengths of each mode in the transmission spectra of Figs. 3.4. For all spectra shown in Figs. 3.4, the transmission peaks are strong in the wavelength larger than $10 \mu\text{m}$, the transmission intensities of these peaks are approximately linearly dependent on the numbers of degenerated modes in the lattice with lattice angle θ . For $\theta = 40^\circ, 50^\circ$ and 70° shown in Fig. 3.4 (a), (b) and (d) and Table 3.2, the transmission intensities of (1,0) Ag/Si modes are about twice stronger than that of the (1,1) Ag/Si modes since their degenerated mode ratio is 4:2. For $\theta = 60^\circ$ shown in Fig. 3.4 (c) and Table 3.2, the (1,0) Ag/Si mode has the maximum peak transmission intensity than those of all other samples since it has the maximum six degenerated modes. For $\theta = 80^\circ$ shown in Fig. 3.4 (e) and Table 3.2, the transmission intensity of (1,0) Ag/Si mode is about twice stronger than (1,1) and



(b)



(d)



(f)

Fig. 3.4 The transmission spectra for samples (a) A, (b) B, (c) C, (d) D, (e) E and (f) F

in the normal direction $\varphi=0^\circ$.

Table 3.2 The theoretical and measured parameters of EOT in the normal direction for silicon substrates with top silver film perforated with hole array arranged in rhombus lattice.

Sample (θ)	modes name	numbers of degenerated modes	degenerated modes	T (μm)	M (μm)	Measured peak intensity (%)
A (40°, 140°)	(1,0) Ag/air	4	(-1,0) (0,-1) (0,1) (1,0)	3.2	3.5	7.9
	(1,1) Ag/air	2	(1,1) (-1,-1)	4.7	5	13.3
	(2,1) Ag/Si	4	(2,1) (-2,-1) (1,2) (-1,-2)	8	8	15.2
	(2,2) Ag/Si	2	(2,2) (-2,-2)	8.1	8.2	14.4
	(1,0) Ag/Si	4	(-1,0) (0,-1) (0,1) (1,0)	11.1	11.3	20.7
	(1,1) Ag/Si	2	(1,1) (-1,-1)	16.2	16.4	12.8
B (50°, 130°)	(1,0) Ag/air	4	(-1,0) (0,-1) (0,1) (1,0)	3.8	4.1	6.1
	(1,1) Ag/air	2	(1,1) (-1,-1)	4.5	4.8	9.7
	(1,0) Ag/Si	4	(-1,0) (0,-1) (0,1) (1,0)	13.2	13.4	17.3
	(1,1) Ag/Si	2	(1,1) (-1,-1)	15.6	15.7	11.1
C (60°, 120°)	(1,0) Ag/air	6	(1,1) (-1,-1) (1,0) (0,1) (-1,0) (0,-1)	4.3	4.7	8.2
	(1,-1) Ag/Si	6	(-2,-1) (2,1) (-1,-2) (1,2) (-1,1) (1,-1)	8.6	8.8	9.3
	(1,0) Ag/Si	6	(1,1) (-1,-1) (1,0) (0,1) (-1,0) (0,-1)	14.9	15.2	23.3
D (70°, 110°)	(1,0) Ag/air	4	(-1,0) (0,-1) (0,1) (1,0)	4.7	5.1	6.8
	(1,1) Ag/Si	2	(1,1) (-1,-1)	14.1	14.2	4.7
	(1,0) Ag/Si	4	(-1,0) (0,-1) (0,1) (1,0)	16.2	16.4	10.8
E (80°, 100°)	(1,0) Ag/air	4	(1,0) (0,1) (-1,0) (0,-1)	4.9	5.4	6.5
	(1,-1) Ag/Si	2	(1,-1) (-1,1)	11.1	11.2	5.5
	(1,1) Ag/Si	2	(1,1) (-1,-1)	13.2	13.3	4.9
	(1,0) Ag/Si	4	(1,0) (0,1) (-1,0) (0,-1)	17	17.2	8.7
F (90°)	(1,0) Ag/air	4	(-1,1) (1,-1) (-1,-1) (1,1)	5	5.4	6.4
	(1,1) Ag/Si	4	(-1,1) (1,-1) (-1,-1) (1,1)	12.2	12.3	7.5
	(1,0) Ag/Si	4	(-1,1) (1,-1) (-1,-1) (1,1)	17.3	17.4	7.4

M and T denotes the measured and theoretical peak wavelengths of SPP modes, respectively.

(1,-1) Ag/Si mode since their degenerated mode ratio is 4:2:2, respectively. For $\theta=90^\circ$ shown in Fig. 3.4 (f) and Table 3.2, the transmission of (1,0) and (1,1) Ag/SiO₂ modes are equal since their degenerated modes are all the same as 4.

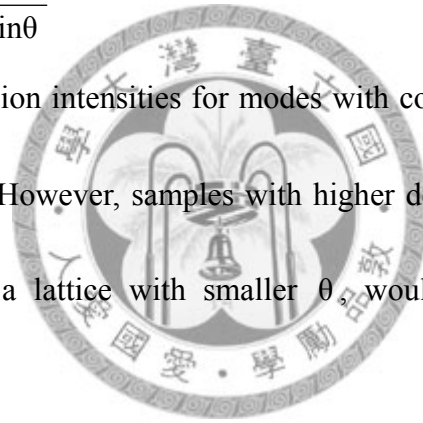
Table 3.3 summarizes the normalized transmission intensities of each mode with respect to unit area of holes in the following rules

$$\text{Normalized transmission} = \frac{\text{Transmission}}{\text{Numbers of degenerated mode} \times \text{Fill factor}} \quad (3.8)$$

where the fill factor is the ratio of total hole area to total measurement area

$$\text{Fill factor} = \frac{1.25^2 \times \pi}{25 \times \text{Sin}\theta} \approx \frac{0.196}{\text{Sin}\theta} \quad (3.9)$$

The normalized transmission intensities for modes with common lattice angle θ are approximately the same. However, samples with higher density of holes or large fill factor, which occurs in a lattice with smaller θ , would have larger normalized transmission intensity.



In the wavelength range smaller than 10 μm for all transmission spectra shown in Fig. 3.4 (a) to (f), it can be found that each Ag/air mode acts as a boundary in the spectra, the transmission intensity becomes larger in the wavelength longer than the Ag/air mode but weaker otherwise. It is noticed that almost no clear transmission peak is observed in the wavelength range smaller than 10 μm although there should be some peaks according to Eq. (3.7) and Figs. 3.2 (g)-(l). For wavelength smaller than 10 μm , the transmission intensity is almost constant and equal to the intensity of the

Table 3.3 The comparisons of normalized transmission intensities for wavelength larger than $10\mu\text{m}$

Sample (θ)	Fill factor (%)	modes name	numbers of degenerated modes	Measured Peak intensity (%)	Normalized peak intensity
A ($40^\circ, 140^\circ$)	30.5	(1,0) Ag/Si	4	20.7	16.9
		(1,1) Ag/Si	2	12.8	21.0
B ($50^\circ, 130^\circ$)	25.6	(1,0) Ag/Si	4	17.3	16.9
		(1,1) Ag/Si	2	11.1	22.0
C ($60^\circ, 120^\circ$)	22.7	(1,0) Ag/Si	6	23.3	17.1
D ($70^\circ, 110^\circ$)	20.9	(1,1) Ag/Si	2	4.7	11.2
		(1,0) Ag/Si	4	10.8	12.9
E ($80^\circ, 100^\circ$)	19.9	(1,-1) Ag/Si	2	5.5	13.8
		(1,1) Ag/Si	2	4.9	12.3
		(1,0) Ag/Si	4	8.7	10.9
F (90°)	19.6	(1,1) Ag/Si	4	7.5	9.5
		(1,0) Ag/Si	4	7.4	9.4

nearest Ag/air modes in the shorter wavelengths no matter whether Ag/Si modes exist or not and how many degenerated modes each Ag/Si mode has. For example, for sample A shown in Fig. 3.4 (a), the transmission intensities of (2,1) and (2,2) Ag/Si modes are almost the same as the (1,1) Ag/air modes although they have four, two and two degenerated modes, respectively, as listed in Table 3.2. Some kind of coupling between higher order Ag/Si modes and Ag/air modes are believed to occur.

The theoretical works of Darmanyan et al. [67] had pointed out that the Ag/Si

and the Ag/air modes which excites on the either side of the silver film would couple together by the tunneling of SPPs through subwavelength holes. Since the shape of the transmission peak for all SPPs modes has a sharper slope at the lower wavelength side and flatter slope at longer wavelength side due to Wood's anomaly [2,68] and different density of SPPs modes [67], the flatter decay of the Ag/air modes in the longer wavelength will couple the Ag/air mode to the nearby higher order Ag/Si modes and suppress their transmission intensities. This explains the step characteristic of Ag/Si modes which has stronger transmission in the wavelength range longer than the Ag/air modes and a quick decay in the wavelength smaller than the Ag/air modes. Previous studies on the influence of hole size on the EOT [17, 69] had indicated that the maximum coupling wavelength is strongly dependent on the hole size, the larger hole size would have longer maximum coupling wavelength due to larger bandwidth of transmission peaks, the bandwidth of Ag/Si steps are longer so that fewer clear Ag/Si peaks are observed.

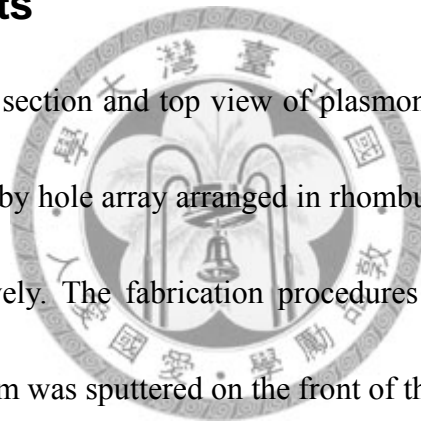
In conclusion, the transmission characteristics of silicon substrates with silver films on top perforated with hole array arranged in a rhombus lattice have been investigated, it is found that the transmission of Ag/Si modes are approximately linearly dependent on the numbers of degenerated modes in the longer wavelength range where the couplings between Ag/Si and Ag/air modes are weak. In the shorter

wavelength range where Ag/Si and Ag/air are coupled together, the transmission intensities are approximately constant without apparent peaks in the wavelength range longer than the Ag/air modes and decay rapidly in the wavelength smaller than the Ag/air modes due to asymmetric slope of the Ag/air mode in the spectra.

3.2 Plasmonic thermal emitters with top metal perforated by hole array arranged in rhombus lattice

3.2.1 Experiments

The schematic cross section and top view of plasmonic thermal emitters (PTEs) with top metal perforated by hole array arranged in rhombus lattice are shown in Figs. 3.5 (a) and (b), respectively. The fabrication procedures of PTEs are described as followed: a 450nm Mo film was sputtered on the front of the Si substrate. Next, a 3nm Ti layer was deposited on the surface of Mo for adhesion followed by a 200 nm Ag layer and a 100nm SiO₂ layer sequentially by e-gun evaporation. Five samples with a 100 nm-thick Ag film perforated with hole array arranged in rhombus lattice with lattice angle θ changing from 50° to 90° in 10° step were produced by thermal evaporation and lift-off. Finally, the edges of the Ag and SiO₂ films were etched by wet etchant. The samples then were placed in a vacuum chamber and a current was sent into the Mo layer to heat it to 240° C. A PERKIN ELMER 2000 Fourier



Transform Infrared Spectrometer (FTIR) was used to measure thermal radiation spectra above the samples in the normal direction. The wavenumber resolution of the measurement was 8 cm^{-1} .

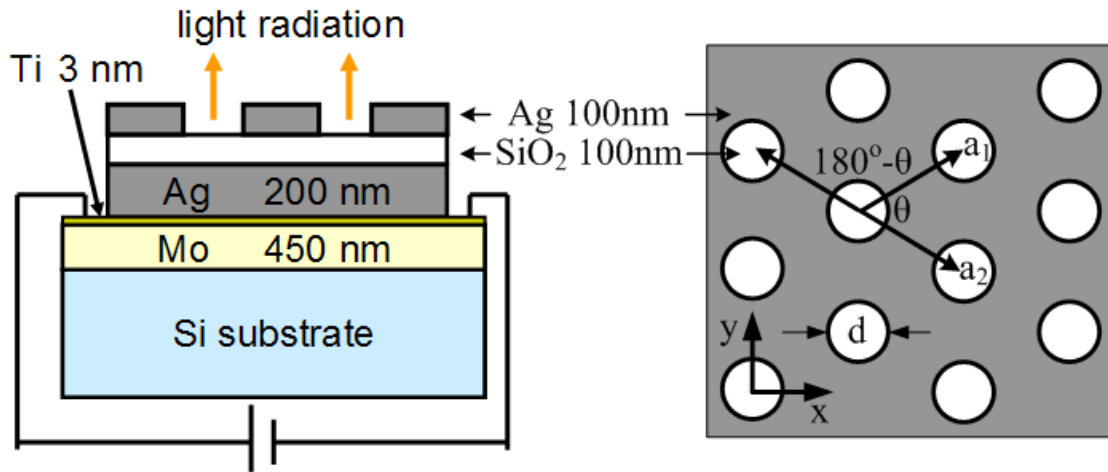


Fig. 3.5 (a) The schematic cross section and (b) top view of PTEs with top metal perforated by hole array arranged in rhombus lattice with $|\vec{a}_1| = |\vec{a}_2| = a = 5 \mu\text{m}$ and $d = 2.5 \mu\text{m}$.

3.2.2 Results and discussion

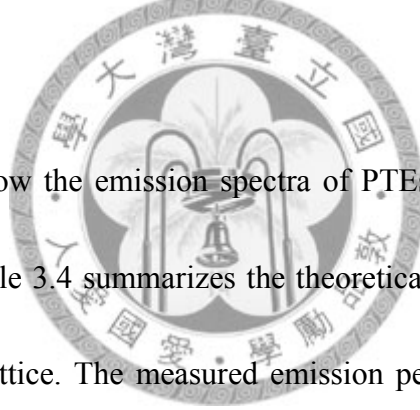
For PTEs, once the current is passed through the Mo layer, the device is heated and the SPPs which are electromagnetic waves would be generated in the interface of Ag/SiO₂ by blackbody radiation and will couple back to the propagation waves if their wavevectors satisfy Eq. (3.4). The wavelengths of emission peaks in the normal direction are similar to Eq. (3.7) except the dielectric constant ϵ_{rd} in Eq. (3.7) should be replaced by the effective dielectric constant ϵ_{reff} due to coupling of SPPs on the top and bottom Ag/SiO₂ interface as introduced in the Eq. (2.57) of Sec. 2.1.2

$$\epsilon_{\text{reff}} = \epsilon_{\text{rd}} \times \left(1 + \frac{\lambda_0}{\pi w \sqrt{-\epsilon_{\text{rm}}}} \sqrt{1 + \frac{\epsilon_{\text{rd}}}{-\epsilon_{\text{rm}}}} \right) \quad (3.10)$$

Replacing ϵ_{rd} in Eq. (3.7) with the ϵ_{reff} in the Eq. (3.10) yields

$$\lambda_0 = \frac{a \times \text{Sin}\theta}{\sqrt{i^2 + j^2 - 2 \times i \times j \times \text{Cos}\theta}} \times \sqrt{\epsilon_{\text{rd}}} \times \left(1 + \frac{\lambda_0}{\pi w \sqrt{-\epsilon_{\text{rm}}}} \sqrt{1 + \frac{\epsilon_{\text{rd}}}{-\epsilon_{\text{rm}}}} \right)^{1/2} \quad (3.11)$$

where λ_0 is the emission peak wavelength, $w=100\text{nm}$ is the thickness of SiO_2 , ϵ_{rd} and ϵ_{rm} are the dielectric constants of SiO_2 and Ag, respectively [52,60,61]. i and j are integers denoting the orders of SPPs modes. Five samples were prepared with $\theta=50^\circ$, 60° , 70° , 80° and 90° . It should be noted that θ and $180^\circ-\theta$ denotes the same lattice structure.

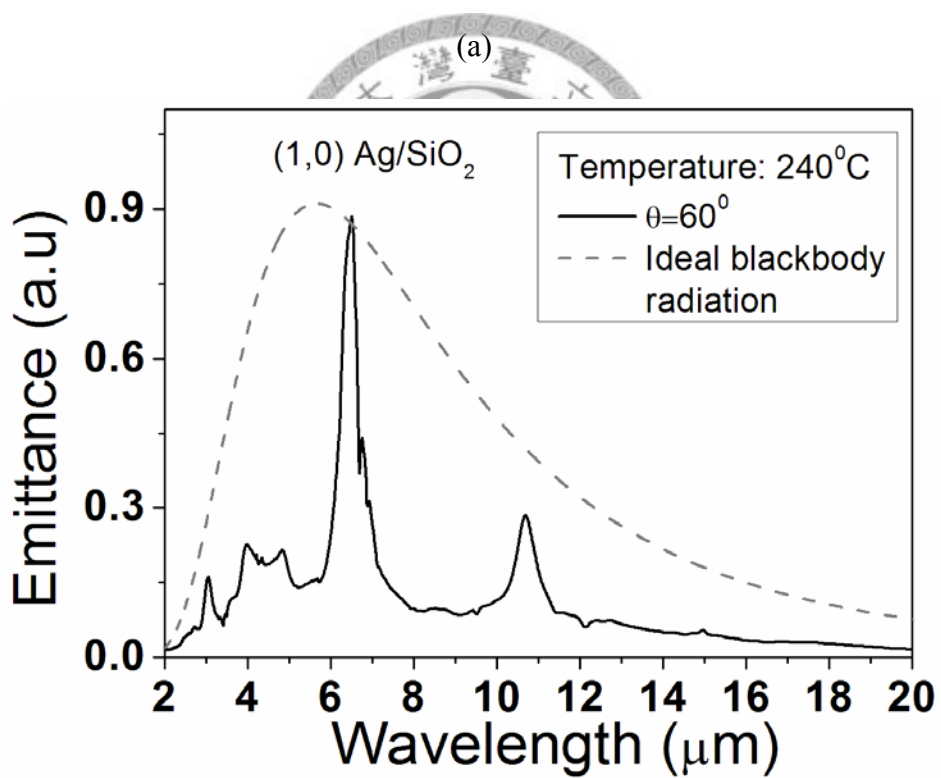
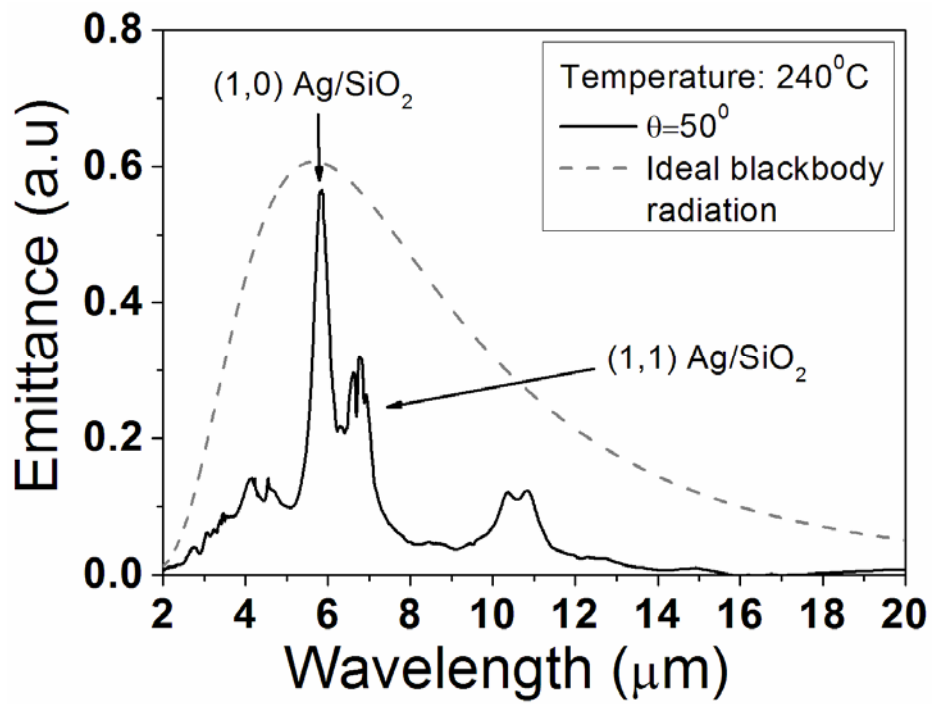


Figs. 3.6 (a) to (e) show the emission spectra of PTEs with $\theta=50^\circ$, 60° , 70° , 80° and 90° , respectively. Table 3.4 summarizes the theoretical and measured parameters of PTEs with rhombus lattice. The measured emission peak wavelengths were very close to the theoretical calculation from Eq. (3.11) and no Ag/air mode was observed. The common emission peaks around $6.7\mu\text{m}$ were the absorption of moisture since that the optical path between chamber and FTIR was not totally in vacuum. The common emission peaks around $10\mu\text{m}$ were optical phonon modes of the SiO_2 .

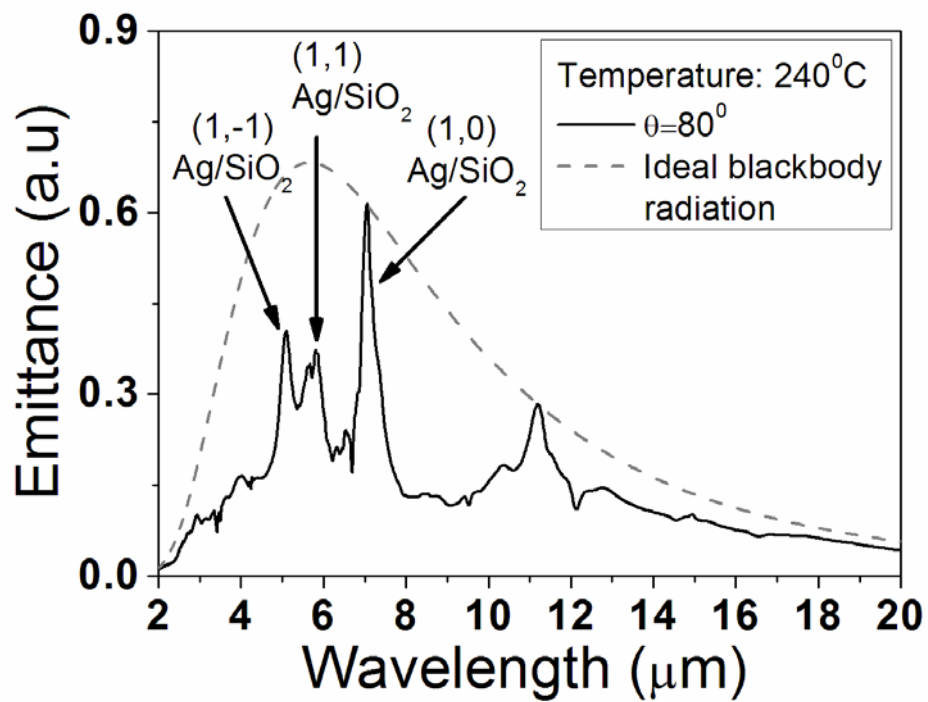
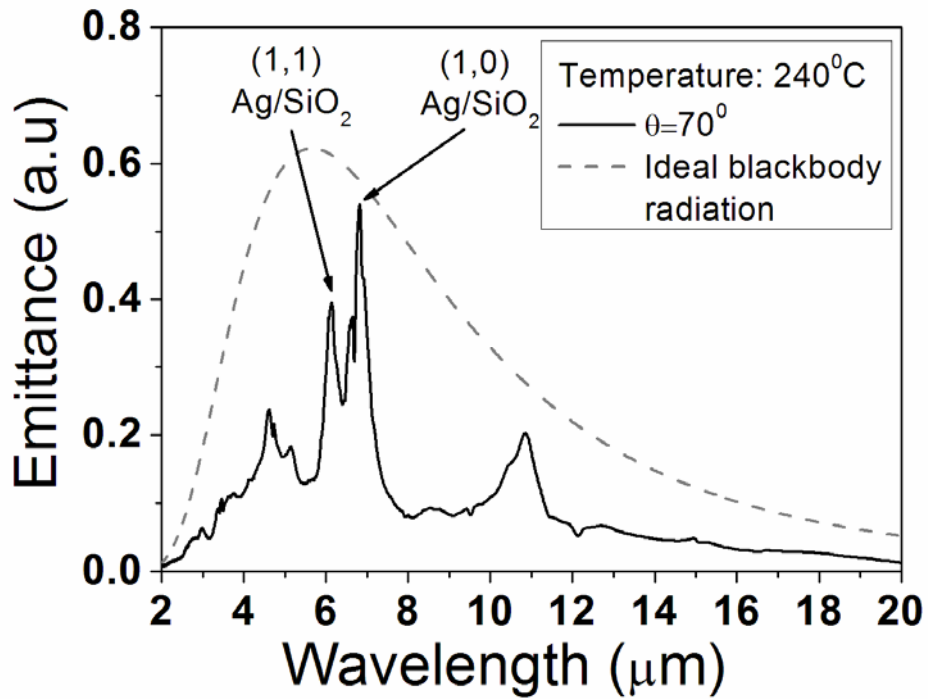
For all spectra, it is clear that the intensities of emission peaks follow the blackbody emission curve multiplying the transmission efficiency of top silver film which is linear dependent on the numbers of degenerated modes. For $\theta=50^\circ$ and 70°

shown in Figs. 3.6 (a) and (c), the emission intensities of (1,0) Ag/SiO₂ modes are about twice stronger than that of the (1,1) Ag/SiO₂ modes since their degenerated mode ratio is 4:2. For $\theta=60^\circ$ shown in Fig. 3.6 (b), the (1,0) Ag/SiO₂ mode has the maximum peak emission intensity than those of all other samples since it has the maximum six degenerated modes. For $\theta=80^\circ$ shown in Fig. 3.6 (d), the emission intensity of (1,0) Ag/SiO₂ mode is about twice stronger than (1,1) and (1,-1) Ag/SiO₂ mode since their degenerated mode ratio is 4:2:2, respectively. For $\theta=90^\circ$ shown in Fig. 3.6 (e), the transmission of (1,0) and (1,1) Ag/SiO₂ modes are equal and the corresponding emission intensities follow the blackbody radiation distribution since their degenerated modes are all the same as 4.

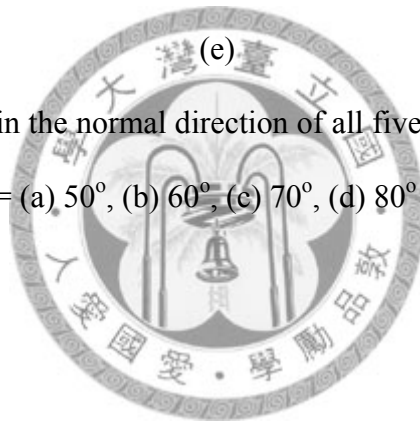
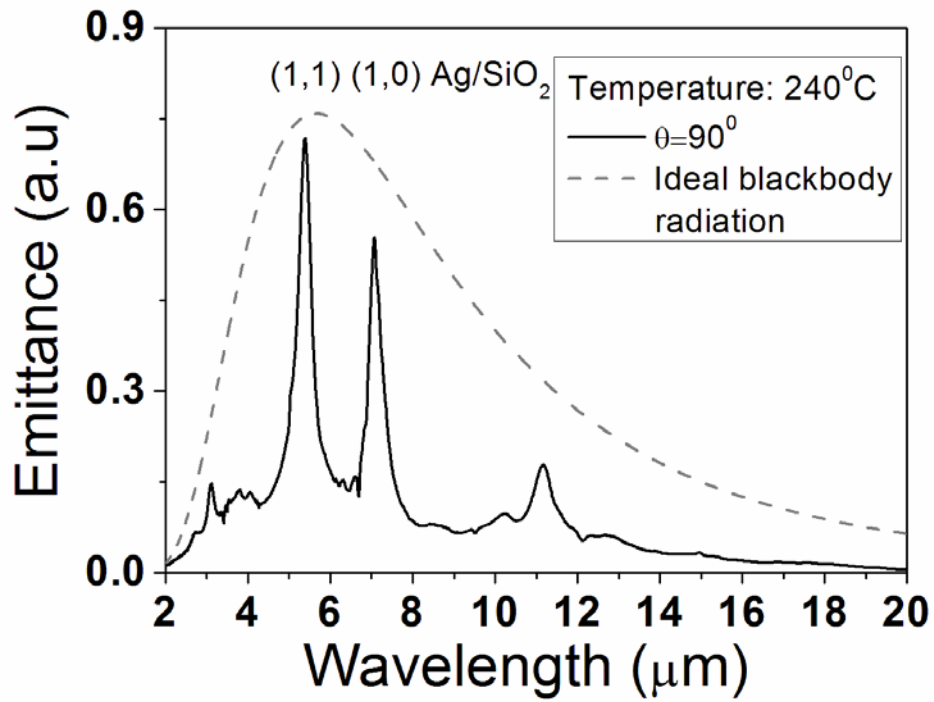
In conclusion, PTEs with rhombus lattice had been investigated experimentally and theoretically. Only hexagonal lattice ($\theta=60^\circ$) produce the strongest radiation peak due to largest degenerated modes. The peak intensities follow the blackbody radiation curve multiplying transmission efficiency of the top metal film which is dependent on the numbers of degenerated modes.



(b)



(d)



(e)
 Fig. 3.6 Emission spectra in the normal direction of all five PTEs with rhombus lattice.

The lattice angle $\theta =$ (a) 50^o, (b) 60^o, (c) 70^o, (d) 80^o and (e) 90^o.

Table 3.4 The theoretical and measured parameters of EOT for PTEs with rhombus lattice.

Sample (θ)	modes name	numbers of degenerated modes	degenerated modes	T (μm)	M (μm)
(50°, 130°)	(1,0) Ag/SiO ₂	4	(-1,0) (0,-1) (0,1) (1,0)	5.88	5.81
	(1,1) Ag/SiO ₂	2	(1,1) (-1,-1)	6.45	6.81
(60°, 120°)	(1,0) Ag/Si O ₂	6	(1,1) (-1,-1) (1,0) (0,1) (-1,0) (0,-1)	6.45	6.51
	(1,1) Ag/SiO ₂	2	(1,1) (-1,-1)	6.67	6.82
(70°, 110°)	(1,0) Ag/SiO ₂	4	(-1,0) (0,-1) (0,1) (1,0)	6.15	6.13
	(1,-1) Ag/SiO ₂	4	(1,-1) (-1,1)	5.13	5.1
(80°, 100°)	(1,1) Ag/SiO ₂	2	(1,1) (-1,-1)	5.9	5.8
	(1,0) Ag/SiO ₂	4	(1,0) (0,1) (-1,0) (0,-1)	6.8	7.06
	(1,1) Ag/SiO ₂	4	(-1,1) (1,-1) (-1,-1) (1,1)	5.56	5.39
90°	(1,0) Ag/SiO ₂	4	(-1,1)(1,-1) (-1,-1)(1,1)	7.07	6.85

M and T denotes the measured and theoretical wavelengths of SPP modes according to Eq. (3.11), respectively.

Chapter 4 The characteristic of cavity modes in the plasmonic thermal emitters and the fabrication of narrow-band cavity thermal emitters

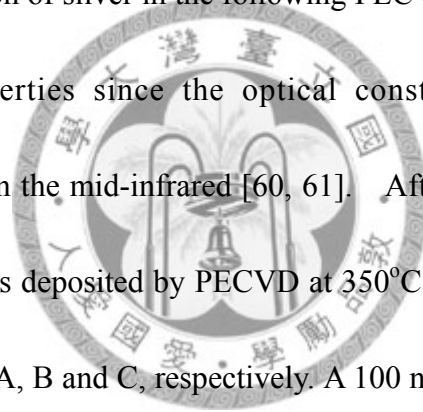
In this chapter, the SiO₂ thickness of PTEs is increased to the order of μm, it is found that not only SPPs modes but also parallel-plate waveguide modes (which are also known as Fabry-Perot resonance modes or simply cavity modes) exist in the reflection and emission spectra. The cavity modes (CMs) would be scattered by the periodic hole array and result in many Bragg scattered CMs in the spectra. Since CMs exhibit narrower full width at half maximum (FWHM) than SPPs modes, they have potential to be applied in mid-infrared thermal emitters with better performance than traditional PTEs. Cavity thermal emitters (CTEs) with randomly distributed hole array (RDHA) and with short period of hole array (SPHA) are proposed to use the CMs to realize narrower-band mid-infrared thermal emitters with purer spectra. The influence of hole size to the CMs is also investigated.

4.1 The characteristic of cavity modes in tri-layer Ag/SiO₂/Au plasmonic thermal emitters

4.1.1 Experiments

The schematic cross section and top view of Ag/SiO₂/Au PTEs with thick SiO₂

layer used in this section are shown in Figs. 4.1(a) and (b), respectively. The fabrication procedures of PTEs with thick SiO₂ are described as followed: a 450nm Mo film was sputtered on the back side of the Si substrate. A 3nm Ti film, 120nm Ag film, 30nm Au film and 3 nm Ti film were deposited on the front side of Si substrate sequentially by E-gun evaporation. The Ti films are used for adhesions which are too thin to affect the optical properties of the SiO₂ cavity. The bottom reflector under the SiO₂ was formed by 30 nm Au/120nm Ag hybrid layers instead of a single 150nm Ag layer to avoid the oxidation of silver in the following PECVD process. This would not affect the optical properties since the optical constants of Au and Ag are approximately the same in the mid-infrared [60, 61]. After the formation of bottom Au layer, a SiO₂ layer was deposited by PECVD at 350°C with the thickness of 0.55, 2 and 2.6μm for samples A, B and C, respectively. A 100 nm-thick Ag film perforated with circular holes arranged in hexagonal lattice was produced by thermal evaporation on patterned photoresist and lifted-off. The samples then were placed in the Bruker IFS 66 v/s system to measure the reflection spectra with incident angles φ to the normal direction of the sample surface from 12° to 65° in 1° step along the ΓK direction as defined in Fig. 4.1(b). Finally, the devices were placed in a vacuum chamber and electric current was sent into the Mo layer to heat the device to measure the thermal radiation in the normal direction ($\varphi = 0^\circ$) using PERKIN ELMER 2000



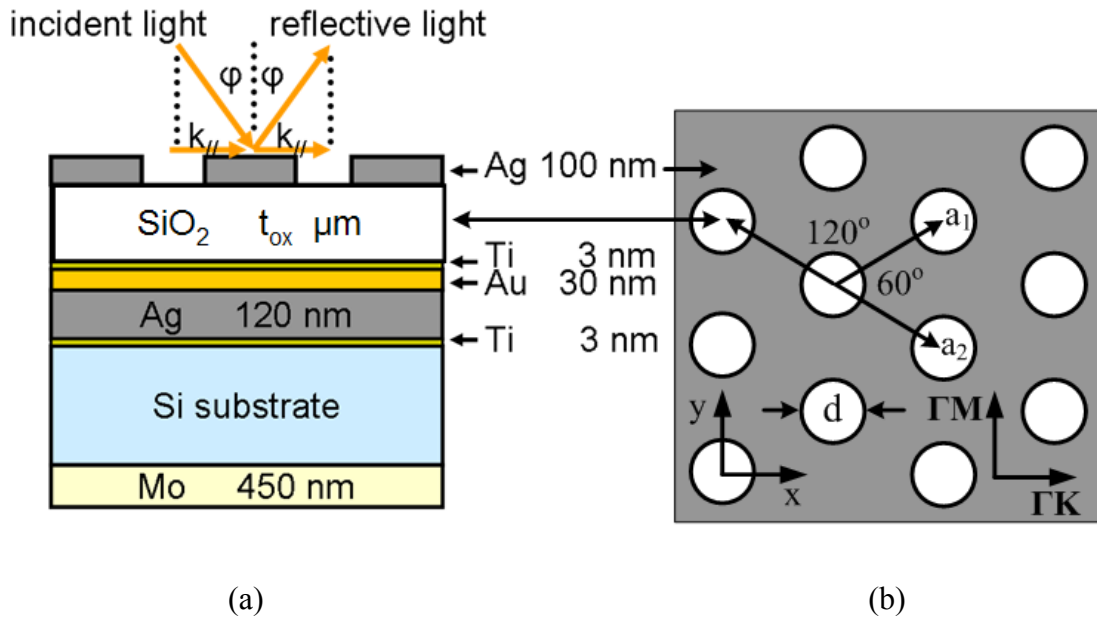


Fig. 4.1 (a) The side view and (b) top view of PTEs with the thickness of SiO₂ $t_{ox}=0.55, 2\mu\text{m}$ and $2.6\mu\text{m}$ for samples A, B and C, respectively. The surface silver films are perforated with hole array in hexagonal lattice with $|\vec{a}_1|=|\vec{a}_2|=a=3\mu\text{m}$ and $d=1.5\mu\text{m}$. φ is the incident and reflective angle, $k_{//}$ is the parallel component of wave vectors of lights.

Fourier Transform Infrared Spectrometer (FTIR). The wavenumber resolutions of both measurements were 8 cm^{-1} .

It should be noted that the fabrication process and device structures for PTEs with thick SiO₂ are a little different from what had been described in Sec. 2.4.2. The Mo layers are moved from top of silicon to the bottom of silicon. Although the output intensity will be stronger if one put the Mo layers in the front of silicon as shown in Fig. 2.6 (a), this process can not be used for the PTEs with the SiO₂ thickness larger

than 1.5 μm . In the traditional process of PTEs whose Mo layers are on the top of silicon wafer, the edges of samples should be immersed sequentially into the silver, buffer oxide and gold etchants to etch the edges of Ag, SiO₂ and Au layers, respectively, to expose the Mo layer and form the electrodes. For thick SiO₂, the capillary effect in the SiO₂ layer sandwiched between Ag and Au layers becomes so serious that the SiO₂ layer absorbs more buffer oxide etchants and is etched deeper; this makes surface Ag layer crack without the support of SiO₂.

4.1.2 Results and discussion

Fig. 4.2 (a) to (c) shows emission spectra of samples A to C, respectively, in the normal direction ($\varphi = 0^\circ$) at temperature 300°C. From traditional theorem of PTEs [38, 40], the wavelengths of emission peaks excited by SPPs are given by

$$\lambda_{\text{SPP}} = \frac{\sqrt{3}}{2} \times \frac{a \times n_{\text{eff}}}{\sqrt{i^2 + j^2} - i \times j} \quad (\text{for SPPs}) \quad (4.1)$$

where λ_{SPP} is the wavelength of (i, j) Ag/SiO₂ SPPs modes in vacuum, n_{eff} is the effective refractive index of the cavity dielectric material and $n_{\text{eff}} \approx n_{\text{SiO}_2}$ for $t \geq 500\text{nm}$ according to the calculation of Eq. (2.57); n_{SiO_2} is the refractive index of SiO₂. From above discussion, the emission peak of (1,0) Ag/SiO₂ should not change once the thickness of SiO₂ is increased to the order of μm . However, the experimental result shown in Fig. 4.2 (b) indicate that once the SiO₂ thicknesses is increased to 2 μm , the (1,0) Ag/SiO₂ SP shown in Fig. 4.2(a), becomes unapparent,

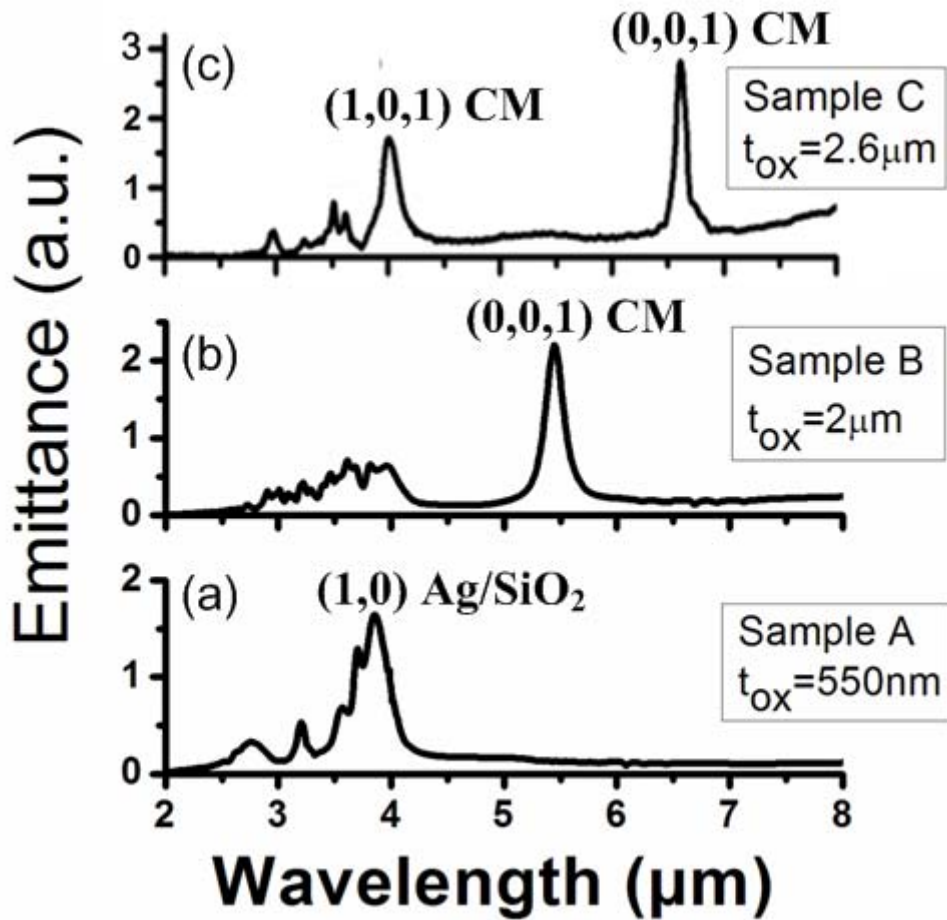


Fig. 4.2 Emission spectra of samples (a) A, (b) B and (c) C at temperature 300°C.

the dominant mode changes from (1,0) Ag/SiO₂ SP to the (0,0,1) cavity mode (CM) at 5.45 μm. The symbol (k, ℓ, m) for cavity mode is defined in Eq. (4.9) which will be discussed later. For the emission spectra of sample C shown in Fig. 4.2(c), the (0,0,1) CM shifts to the 6.61 μm and another (1,0,1) CM appear in the spectra at 3.65 μm. Actually, these SiO₂-thickness-dependent CMs are the propagating plane waves guided in the Ag/SiO₂/Au parallel-plate waveguide [57] and were observed in the

far-field by tunneling through the subwavelength holes perforated in the surface silver films. They are also known as Fabry-Perot resonance mode [45] or simply cavity mode (CM).

In the mid-infrared, the optical constants of Au and Ag are approximately the same [60, 61]; their skin depths [64] are $\delta = \frac{1}{\sqrt{\omega^2 \mu_0 \epsilon_0 \text{Sin}^2 \varphi - \omega^2 \mu_{\text{rm}} \epsilon_{\text{rm}}}} \approx 20 \text{ nm}$ which

are much smaller than the thickness of SiO₂ and the wavelengths of interested so that can be ignored. CMs can be approximated as the waves guided in the pefrect-conductor/SiO₂/perfect-conductor parallel-plate waveguide whose dispersion relation are [57]

$$|\overline{k}_{\text{cm}}| = \sqrt{\left(\frac{\omega}{c} n_{\text{SiO}_2}\right)^2 - \left(\frac{m\pi}{t_{\text{ox}}}\right)^2} \quad (\text{for CMs}) \quad (4.2)$$

where ω is the angular frequency of wave, c is the speed of light in vacuum, m is any integer denotes the order of CMs, t_{ox} is the thickness of SiO₂. Besides CMs,

SPPs exist in the Ag/SiO₂/Au cavity either with dispersion relation from Eq. (2.31)

$$|\overline{K}_{\text{sp}}| = \frac{\omega}{c} \sqrt{\frac{n_{\text{eff}}^2 \times \epsilon_{\text{rm}}}{n_{\text{eff}}^2 + \epsilon_{\text{rm}}}} \quad (\text{for SPPs}) \quad (4.3)$$

where ϵ_{rm} is the relative dielectric constant of metals which can be gold or silver, the difference of choice of metals to the final calculation is very tiny. Both CMs and SPPs would be scattered by the periodic hole array according to the momentum conservation laws from Eq. (2.66) and (2.67)

$$\vec{k}_{\text{cm}} = \vec{k}_{//} + k\vec{G}_1 + \ell\vec{G}_2 \quad (\text{for CMs}) \quad (4.4)$$

$$\vec{k}_{\text{sp}} = \vec{k}_{//} + i\vec{G}_1 + j\vec{G}_2 \quad (\text{for SPPs}) \quad (4.5)$$

where $\vec{k}_{//}$ is the parallel component of wave vector of lights as shown in Fig. 4.1 (a).

$i, j, k,$ and ℓ are any integers; \vec{G}_1 and \vec{G}_2 are the reciprocal lattice vectors of hexagonal lattice as described in Eqs. (3.9) - (3.10)

$$\vec{G}_1 = (G_{1x}, G_{1y}) = \frac{\pi}{a} \times \left(\frac{1}{\cos \frac{\theta}{2}}, \frac{1}{\sin \frac{\theta}{2}} \right) \quad (4.6)$$

$$\vec{G}_2 = (G_{2x}, G_{2y}) = \frac{\pi}{a} \times \left(\frac{1}{\cos \frac{\theta}{2}}, \frac{-1}{\sin \frac{\theta}{2}} \right) \quad (4.7)$$

where $\theta=60^\circ$ for hexagonal lattice, $a=3\mu\text{m}$ as described in Fig. 4.1 (b).

When the lights are measured along ΓK direction with angle φ normal to the surface as shown in Fig. 4.1 (b), the parallel component of wave vectors of lights are

$$\vec{k}_{//} = (k_x, 0, 0) = (k_0 \times \sin \varphi, 0, 0) \quad (4.8)$$

where $k_0 = \frac{\omega}{c}$

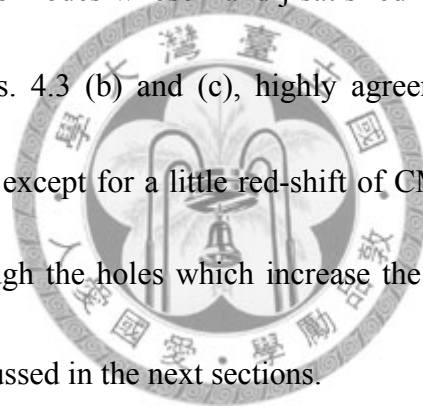
Substituting Eqs. (4.2), (4.3) and (4.6) - (4.8) into Eqs. (4.4) - (4.5) yields

$$\sqrt{\left(\frac{\omega}{c} n_{\text{SiO}_2}\right)^2 - \left(\frac{m\pi}{t_{\text{ox}}}\right)^2} = \sqrt{(kG_{1x} + \ell G_{2x} + k_x)^2 + (kG_{1y} + \ell G_{2y})^2} \quad (\text{for CMs}) \quad (4.9)$$

$$\frac{\omega}{c} \times \sqrt{\frac{n_{\text{eff}}^2 \times \epsilon_{\text{rm}}}{n_{\text{eff}}^2 + \epsilon_{\text{rm}}}} = \sqrt{(iG_{1x} + jG_{2x} + k_x)^2 + (iG_{1y} + jG_{2y})^2} \quad (\text{for SPPs}) \quad (4.10)$$

In the mid-infrared, $\text{Re}[-\epsilon_{\text{rm}}] \gg n_{\text{SiO}_2}^2 \approx n_{\text{eff}}^2$ [52, 60, 61]. Use this approximation

and ignore the imaginary part of ε_{m} , Eq. (4.9) and (4.10) can be plotted on the dispersion relation of reflection spectra for comparison. Figs. 4.3 (a)-(c) show the experimental dispersion relation of reflection spectra with measuring angle φ from 12° to 65° for samples A to C. Figs. 4.3 (d) and (e) show the comparison between theoretical and experimental results for samples B and C, respectively. The blue dashed lines are the calculation results of Eq. (4.9). The symbol (k, ℓ, m) CM denoted in the figures represent the CMs whose k , ℓ and m satisfies Eq. (4.9). Similarly, (i, j) Ag/SiO₂ denotes the SPPs modes whose i and j satisfied Eq. (4.10). Compared Figs. 4.3 (d) and (e) with Figs. 4.3 (b) and (c), highly agreements between theory and experiments are obtained except for a little red-shift of CMs. This red-shift is due to the leakage of light through the holes which increase the effective thickness t_{ox} in Eq. (4.9) and will be discussed in the next sections.



In the normal direction ($\varphi = 0^\circ$), the wavelengths of emission peaks in vacuum can be obtained by solving Eq. (4.9) and (4.10) with $\varphi = 0^\circ$

$$\lambda_{\text{CM}} = \frac{2n_{\text{SiO}_2}}{\sqrt{\frac{16}{3 \times a^2} (k^2 - k \times \ell + \ell^2) + \left(\frac{m}{t_{\text{ox}}}\right)^2}} \quad (\text{for CMs}) \quad (4.11)$$

$$\lambda_{\text{SPP}} = \frac{\sqrt{3}}{2} \times \frac{a \times n_{\text{SiO}_2}}{\sqrt{i^2 + j^2 - i \times j}} \quad (\text{for SPPs}) \quad (4.12)$$

Table 4.1 summarizes the theoretical peak wavelengths and experimental results of samples A to C shown in Fig. 4.2. Highly agreements between theoretical and

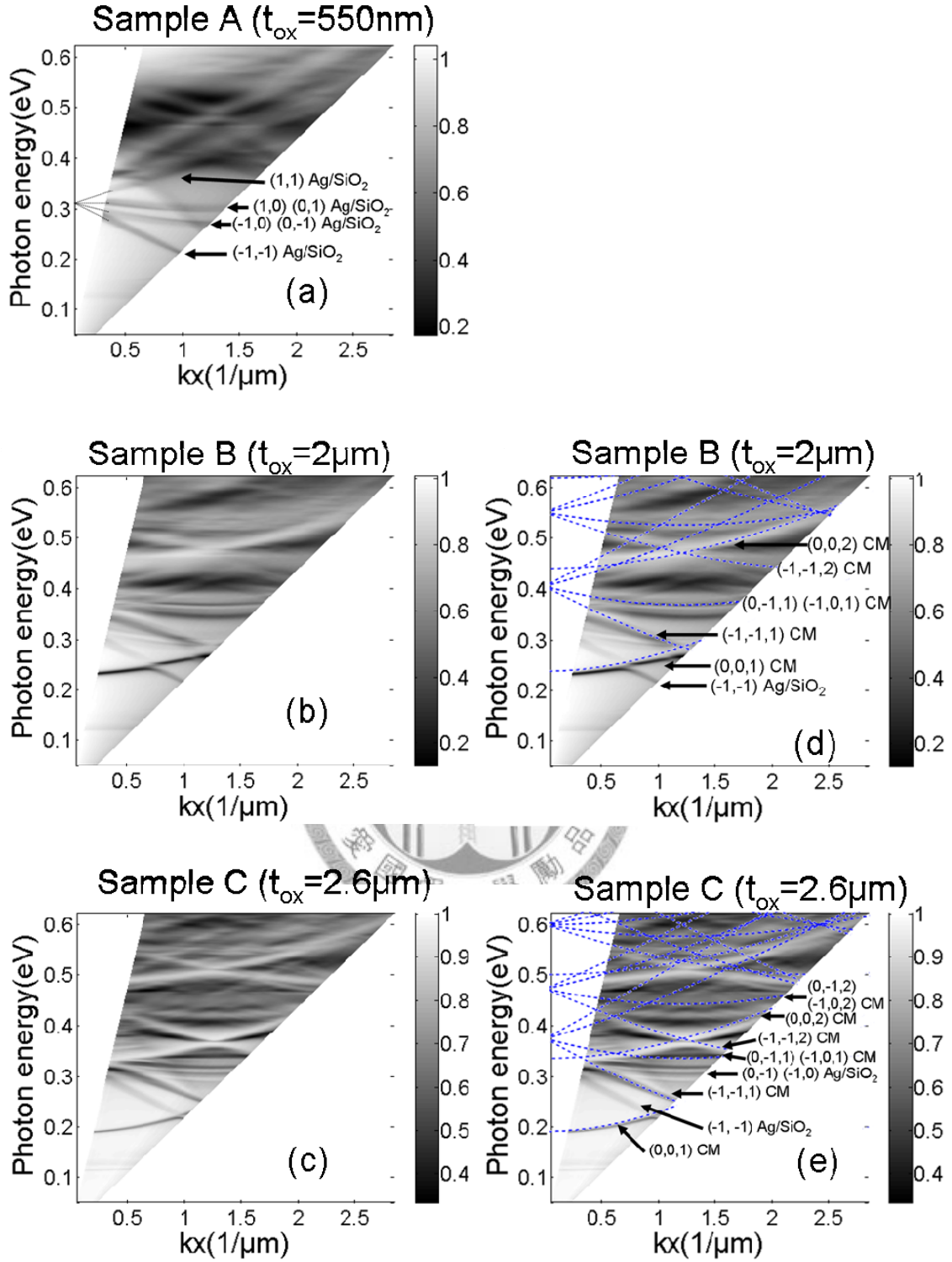


Fig. 4.3 The dispersion relation of reflection spectra for samples (a) A, (b) B, (c) C and their modes analysis for samples (d) B and (e) C. The blue dashed lines are the calculated results of Eq. (4.9).

experimental results are obtained except a little red-shift of CMs. CMs exhibit narrower FWHM, narrower $(\Delta\lambda)/\lambda$ and higher Q factors than SPPs modes, especially for longer wavelengths as listed in Table 4.2.

Eqs. (4.9) and (4.11) indicate that CMs can be divided into two category: intrinsic CMs whose $(k, \ell)=(0,0)$ and Bragg scattered CMs whose k and ℓ are not all zero. For intrinsic CMs whose $k=\ell=0$, Eq. (4.9) reduces to Eq. (4.2), the intrinsic CMs can be viewed as propagating waves guided in the parallel-plate waveguide without scattering by the surface hole array. The wavelengths of intrinsic CMs are determined by the thickness of cavity t_{ox} and the measuring angle φ only. For Bragg scattered CMs, the waves are associated with the surface periodic hole array, not only t_{ox} and φ but also lattice parameters such as θ and a will affect the wavelengths of CMs. Besides, incident lights along different direction will result in the different peak wavelengths. For example, if the lights are incident in the ΓM direction as defined in Fig. 4.1(b). The Eq. (4.9) should be rewritten as

$$\sqrt{\left(\frac{\omega}{c}n_{SiO_2}\right)^2 - \left(\frac{m\pi}{t_{ox}}\right)^2} = \sqrt{(kG_{1x} + \ell G_{2x})^2 + (kG_{1y} + \ell G_{2y} + k_y)^2} \quad (4.13)$$

$$\text{where } k_y = k_0 \times \text{Sin}\varphi \quad (4.14)$$

Figs. 4.4 (a) and (b) show the measured dispersion relation of reflection spectra in the ΓM direction and their mode analysis according to Eqs. (4.13) and (4.14). Compared with the ΓK direction as shown in Figs. 4.3 (b) and (d), the dispersion

Table 4.1 The comparisons between theoretical peak wavelengths and measured results of emission spectra of samples A, B and C in $\varphi = 0^\circ$ direction.

Modes name	Sample A		Sample B		Sample C	
	T (μm)	M (μm)	T (μm)	M (μm)	T (μm)	M (μm)
(1,0) Ag/SiO ₂	3.77	3.85	3.7	none clear	3.7	none clear
(0,0,1) CM	1.6	not in MIR	5.24	5.45	6.28	6.61
(1,0,1) CM	0.8	not in MIR	2.82	none clear	3.65	4.01

T denotes the theoretical values and M denotes the measured values.

Table 4.2 The comparisons between theoretical values and measured results of emission spectra of samples A to C.

	Sample A	Sample B	Sample C	
Dominant mode	(1,0) Ag/SiO ₂	(0,0,1) CM	(0,0,1) CM	(1,0,1) CM
λ (μm)	3.85	5.45	6.61	4.01
FWHM (μm)	0.35	0.2	0.12	0.12
$(\Delta\lambda)/\lambda$	0.09	0.037	0.018	0.03
Q factor	11	26.9	56	33
Output power (mW/cm ²)	130	145	210	137

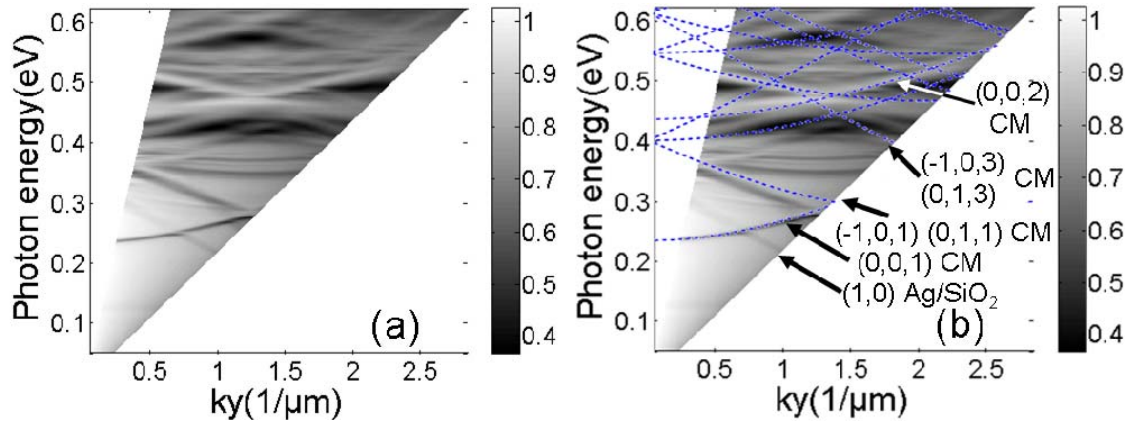


Fig. 4.4 (a) The measured dispersion relation of reflection spectra and (b) corresponding modes analysis for sample B. The blue dashed lines are the calculations results of Eq. (4.13).

curves of Bragg scattered CMs are different. However, the dispersion curves of intrinsic CMs are the same since intrinsic CMs are not associated with surface period.

In conclusions, not only SPPs modes but also CMs would exist in the PTEs, Both of them would be scattered by surface periodic structures according the momentum conservation laws. The characteristic of FWHM, $(\Delta\lambda)/\lambda$, Q factor of CMs are all better than the characteristic of SPPs modes.

4.2 Cavity thermal emitters with randomly distributed hole array and the influence of hole size to the cavity modes

CMs exhibited better performance than SPPs in the emission spectra of a PTE. It can be used to fabricate better thermal emitters if Bragg scattered CMs and SPPs

modes can be filtered out. In this section, CTEs with randomly distributed hole array (RDHA) are proposed to eliminate these unwanted modes which are associated with surface periodic structures. Beside, the influence of hole size to the emission peaks and reflection spectra is investigated.

4.2.1 Experiments

The schematic cross section and top view of CTEs with RDHA are shown in Figs. 4.5 (a) and (b), respectively. The fabrication processes are the same as described in previous section, eleven samples D to N were prepared for experiments and their structure parameters are summarized in Table 4.3. The reflection spectra of sample N is measured along ΓK direction with angle ϕ normal to the surface as defined in Fig. 4.1 (b). For samples D to F, there are no holes perforated in the surface metals so that

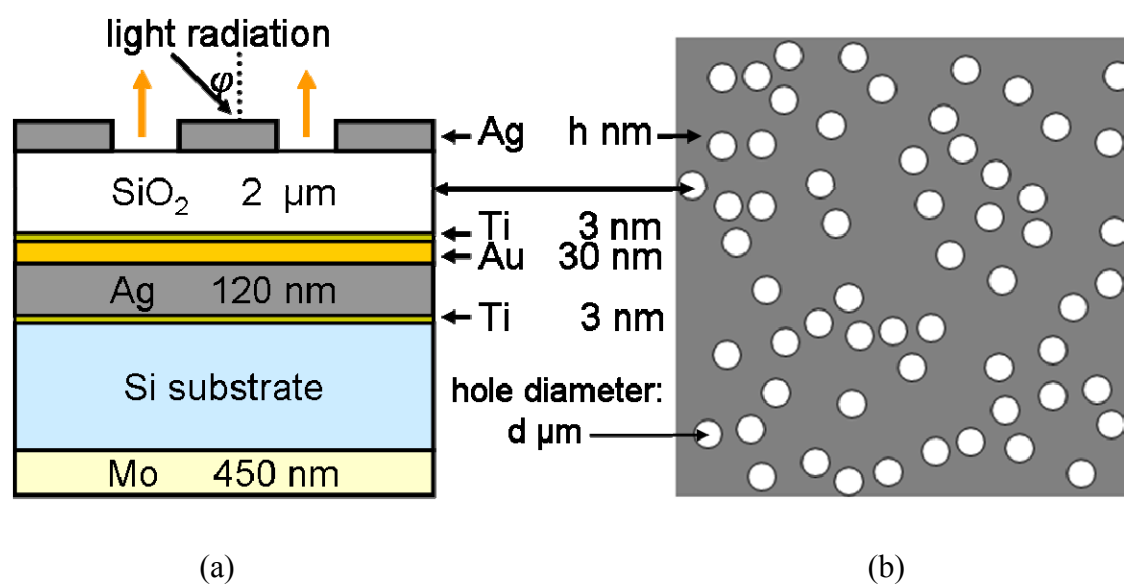
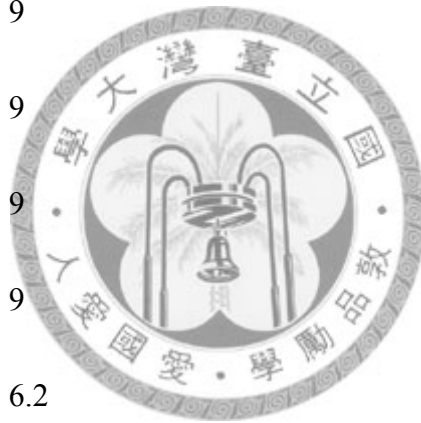


Fig. 4.5 (a) The side view and (b) top view of CTEs with RDHA.

Table 4.3 The structure parameters of samples with randomly distributed hole array, d

denotes the diameters of holes and h denotes the thickness of to silver film.

Sample	d (μm)	h (nm)	DH* (%)
D	0	12.5	0
E	0	15	0
F	0	20	0
G	1	100	6.2
H	1.5	100	9
I	2.5	100	9
J	3.5	100	9
K	4.5	100	9
L	2	100	6.2
M	2	100	9
N**	2	100	40.3



*DH: Density of holes: total hole area over total area of pattern

**Sample N is a CTE with hole array arranged in hexagonal lattice instead of RDHA

in order to offer maximum density of holes for comparison. The period of hole

array for sample N is $a=3\mu\text{m}$.

there is no need of lithography and lift-off in the fabrication processes. Simulations [45, 51] suggest that once the thicknesses h of top Ag layers are in the order of skin depth ($\sim 20\text{nm}$), intrinsic CMs can be excited in the cavity and radiate to the far-field by leaking through surface thin film and vice versa. These kind of structures can be viewed as one kind of CTEs with zero hole size.

The masks of RDHA used for lithography were designed by the computer program. A unit basis of $500\mu\text{m} \times 500\mu\text{m}$ RDHA was generated and then spanned into the size of $1\text{cm} \times 1\text{cm}$ by periodic mapping for all samples. The nearest edge-to-edge distance allowed for holes is $1\mu\text{m}$. The distribution of the nearest center-to-center distance for all holes are calculated and recorded in the step of mask-design by counting the nearest center-to-center distance from one hole to all other holes within the area of unit basis. The distributions of numbers of holes as a function of the nearest center-to-center distance are chosen to be as decentralized as possible without a peak at certain wavelengths. This is because large number of holes with common nearest center-to-center distance makes the distribution of the lattice momentum in the reciprocal lattice concentrate in some point $(\overline{G}_1, \overline{G}_2)$. These high weight of \overline{G}_1 and \overline{G}_2 would contribute into the Eqs. (4.4) and (4.5) even if surface holes are distributed randomly without period [70].

All patterns of RDHA are checked in the extraordinary transmission. The

fabrication and measurement methods are the same as those described in Sec 3.1. Fig. 4.6 compares the distribution of the nearest center-to-center distance of holes with the transmission of RDHA in normal direction for sample I. The relation of transmission maximum to the distribution maximum follow the following equation

$$\lambda_T = \frac{\sqrt{3}}{2} \times \frac{a_{\text{eff}} \times n}{\sqrt{i^2 + j^2 - i \times j}} \quad (4.15)$$

where λ_T is the wavelength of the maximum transmission. a_{eff} is the nearest center-to-center distance of all holes whose weight are the largest. $n=3.45$ is the refraction index of the Si substrate. Eq. (4.15) is the same as Eq. (4.12) so that a_{eff} can be viewed as effective period of hole array. However, due to highly decentralized distribution of the nearest center-to-center distance among holes, the transmission is very weak and there is no apparent EOT observed in the spectra. Not only the RDHA patterns used for sample I but also other RDHA patterns had been checked in the transmission experiments to make sure that all RDHAs are random enough without effective period for all samples. The maximum density of holes for sample G is 6.2% which can not be elevated further without reducing the minimum distance between neighboring holes.

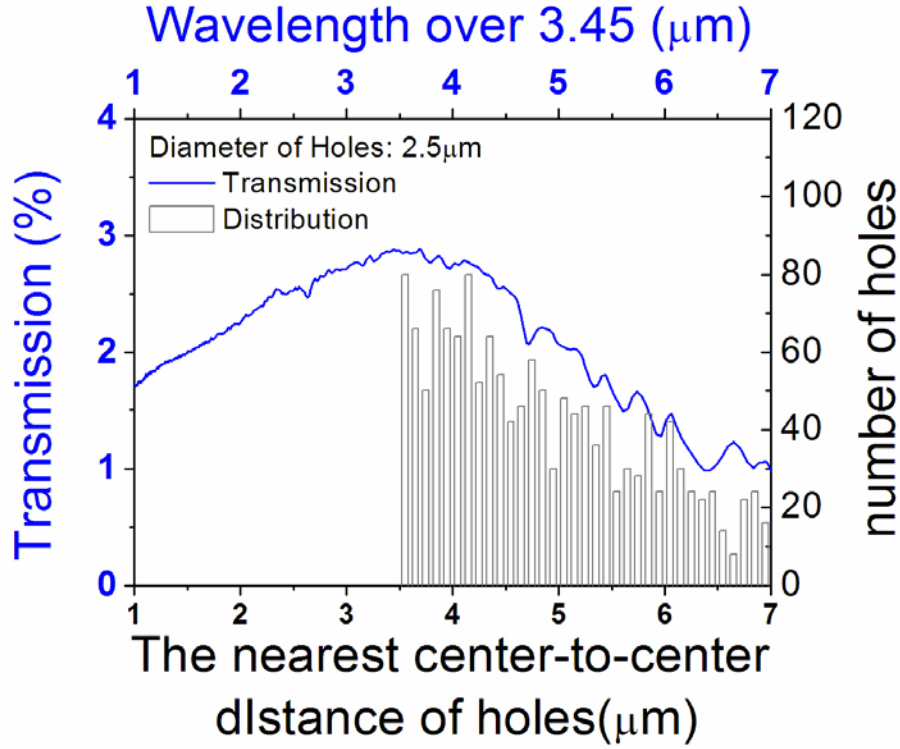


Fig. 4.6 The relation between transmission and the distribution of the nearest center-to-center distance of holes for sample I.



4.2.2 Results and discussion

For CTEs with RDHA, the SPPs modes can not be excited due to lack of periodicity coupling as discussed in Sec 2.2. RDHA can be viewed as a periodic structure with period of infinite; substituting Eqs. (4.6) and (4.7) into Eq. (4.4) with $a = \infty$ yields

$$\sqrt{\left(\frac{\omega}{c} n_{\text{SiO}_2}\right)^2 - \left(\frac{m\pi}{t_{\text{ox}}}\right)^2} = |k_{//}| \quad (\text{for CMs}) \quad (4.16)$$

For zero order measurement ($\varphi = 0^\circ$), the wavelengths of emission peaks in vacuum can be obtained by solving Eq. (4.16) with $k_{//} = 0$

$$\lambda_{\text{CM}} = \frac{2 \times t_{\text{ox}} \times n_{\text{SiO}_2}}{m} \quad (\text{for CMs}) \quad (4.17)$$

Eqs. (4.16) and (4.17) are identical with Eqs. (4.9) and (4.11) in the condition of $k=\ell=0$, this means that only intrinsic CMs without SPPs and Bragg scattered CMs can be excited in the cavity. The emission spectra should be pure and narrow-band with the intrinsic CMs only. The theoretical dispersion curves according to Eq. (4.16) are shown in Fig. 4.7. The SiO₂ thickness used in the calculation is 2 μm .

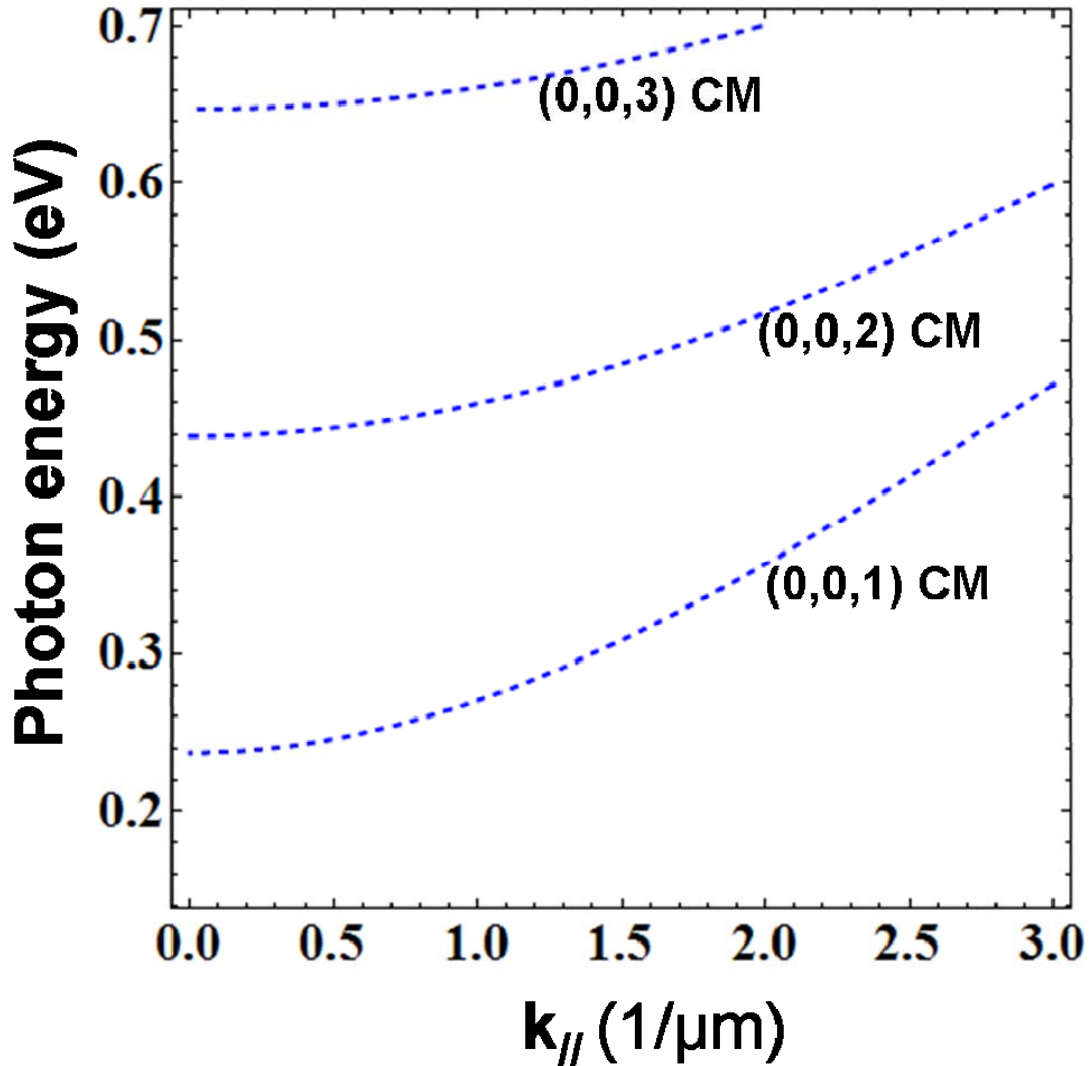
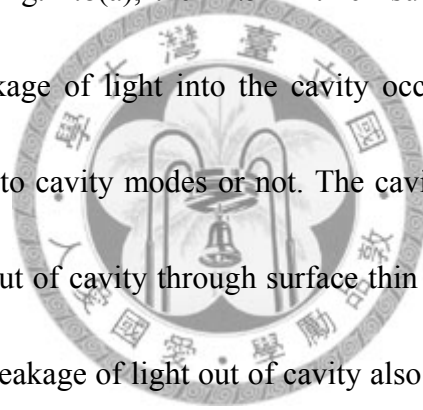


Fig. 4.7 Theoretical dispersion curves of CM for CTEs with RDHA. $t_{\text{ox}}=2 \mu\text{m}$

Figs. 4.8 (a)-(c) show the experimental dispersion relation of reflection spectra with measuring angle φ from 12° to 65° for samples D to F where no holes exist in the surface silver film. Figs. 4.8 (d)-(f) show the comparison of theoretical and experimental results for samples D to F, respectively. The blue dashed lines are the calculated results of Eq. (4.9). The symbol $(0,0,m)$ CM denoted in the figures represent the CMs whose $k=l=0$ and m satisfies Eq. (4.9). The spectra are much cleaner compared with CTEs with periodic hole array as shown in Figs. 4.3 and 4.4.

For sample D shown in Fig. 4.8(a), the 12.5nm thick surface thin film is not thick enough so that large leakage of light into the cavity occurs no matter whether the incident light can couple to cavity modes or not. The cavity modes can propagate in the waveguide and leak out of cavity through surface thin film and results in a bright band in Fig. 4.8 (a). The leakage of light out of cavity also increases the bandwidth of resonance modes. For sample E shown in Fig. 4.8 (b), the bandwidth of CMs become much smaller and the reflections are still very low. For sample F shown in Fig. 4.8(c), the thickness of top thin film is 20 nm which is too thick to enable the light leaking from surface into the cavity if it is not a cavity mode, therefore, the reflection coefficient is almost one; however, for light coupled to cavity mode, the reflection becomes weak and dark line appears, the reflections of $(0,0,1)$ CM and $(0,0,2)$ CM for sample F are higher than the reflections of $(0,0,1)$ CM and $(0,0,2)$ CM for sample E



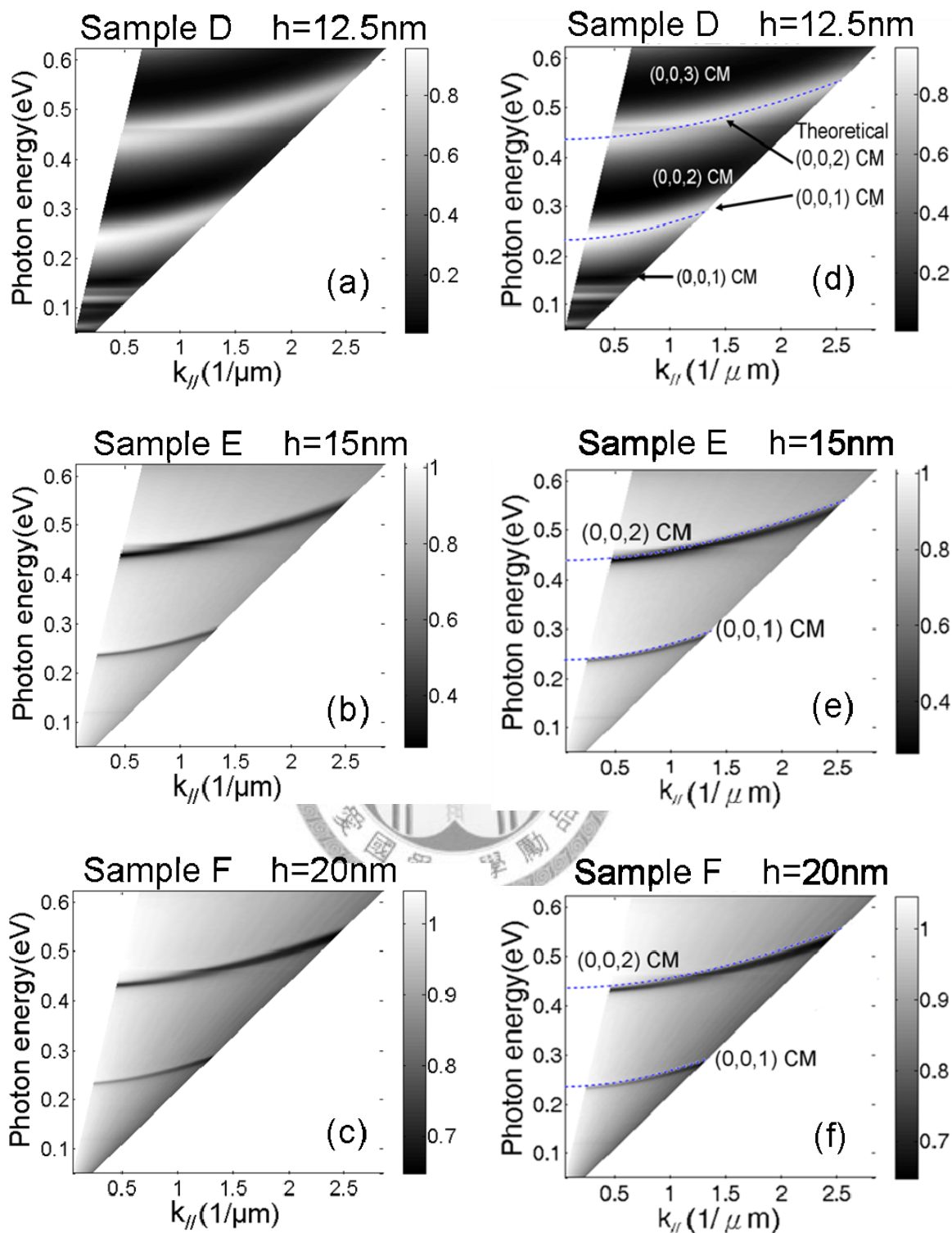


Fig. 4.8 The dispersion relation of reflection spectra for sample (a) D, (b) E, (c) F and their modes analysis for sample (d) D, (e) E and (f) F. The blue dashed lines are the calculated results of Eq. (4.9).

due to lower coupling efficiency of light to CMs whose surface silver film is thicker.

Figs. 4.9 (a)-(c) show the dispersion relation of reflection spectra for samples G to I, respectively, not only the upward curved intrinsic CMs but also the horizontal dark lines and bright lines are observed for all spectra as denotes as $(0,0,m)$ LCM which indicate the characteristic that horizontal $(0,0,m)$ LCMs always intersect with $(0,0,m)$ CMs at $k_{||}=0$. The horizontal lines act as the localized cavity modes (LCMs) independent on the direction of incident light. Beside, a broad band horizontal dark lines below $(0,0,1)$ LCM is observed either for Sample I denoted as FP-hole,

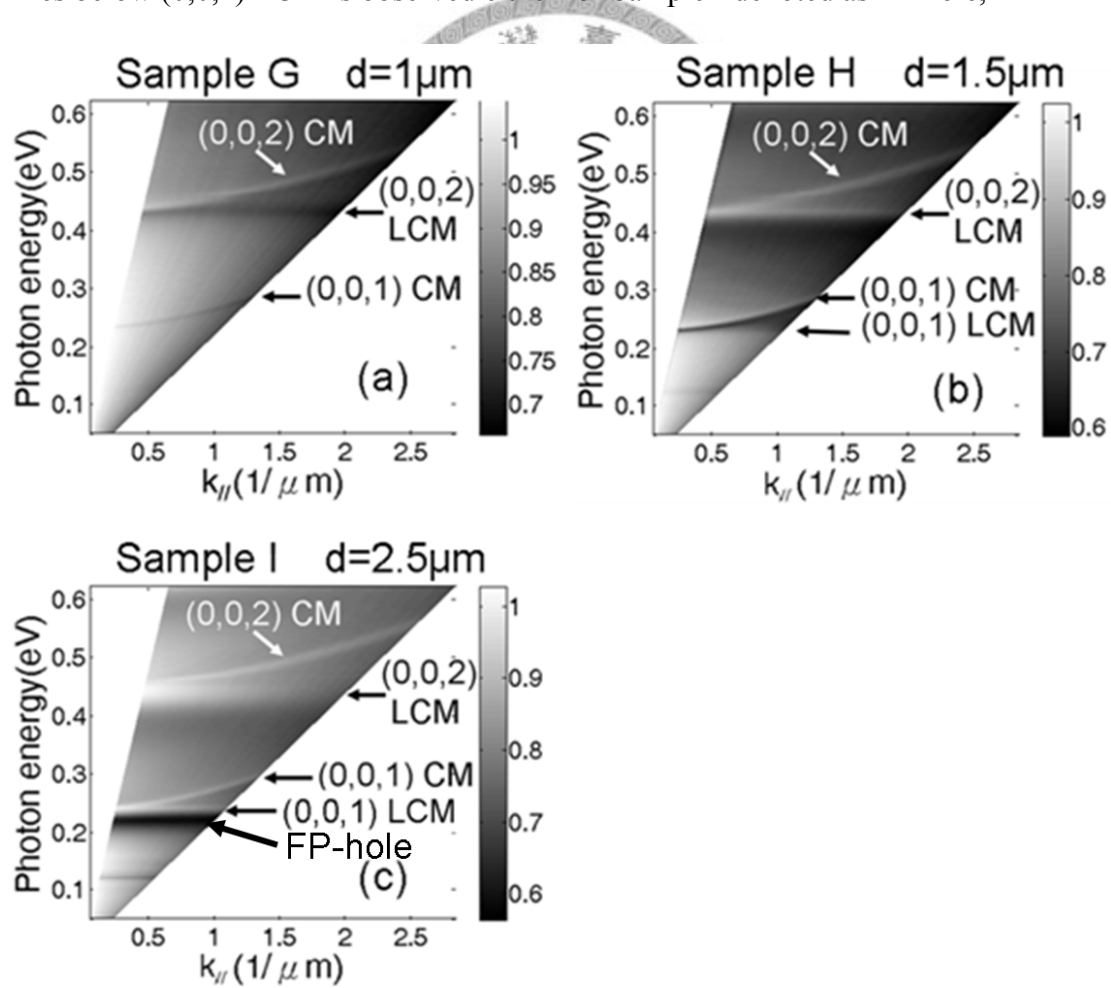


Fig. 4.9 The dispersion relation of reflection spectra of samples (a) G, (b) H and (c) I.

Actually, these LCMs are the localized standing waves resonated in the cavity in the direction normal to samples in the cutoff frequency

$$\frac{\omega}{c} n_{\text{SiO}_2} = \frac{m\pi}{t_{\text{ox}}} \quad (4.18)$$

The incident lights are scattered by the holes once the wavelengths of LCMs are smaller than three times of hole diameters. Fig. 4.10 shows the theoretical dispersion curves of CMs and LCMs according to the Eq. (4.16) and (4.18). Two curves with common m value would interest at $k_{\parallel}=0$. Consider the dispersion relation of reflection spectra for samples G to I as shown in Figs. 4.9 (a)-(c), respectively. For sample G, the hole diameter is $1 \mu\text{m}$, $(0,0,1)$ LCM does not appear since the theoretical wavelength of $(0,0,1)$ LCM is $5.4 \mu\text{m}$ which is three times larger than the hole diameter. The hole diameter is too small to scatter the incident light to form the $(0,0,1)$ LCM. For $(0,0,2)$ LCM, the wavelength of $(0,0,2)$ LCM is $2.87 \mu\text{m}$ which is smaller than the three times of hole diameter, the holes scatter incident lights so that forms the $(0,0,2)$ LCM.

For sample H, the hole diameter is $1.5 \mu\text{m}$, very weak $(0,0,1)$ LCM seems to appear in the theoretical position, The theoretical wavelength of $(0,0,1)$ LCM is $5 \mu\text{m}$ which is larger than three times of hole diameter but the difference is small, very weak $(0,0,1)$ LCM are formed due to low scattering efficiency of holes. For sample H, the hole diameter is $2.5 \mu\text{m}$, both $(0,0,1)$ and $(0,0,2)$ LCM appear clearly since the wavelengths of $(0,0,1)$ and $(0,0,2)$ LCM are $5 \mu\text{m}$ and $2.87 \mu\text{m}$, respectively, which

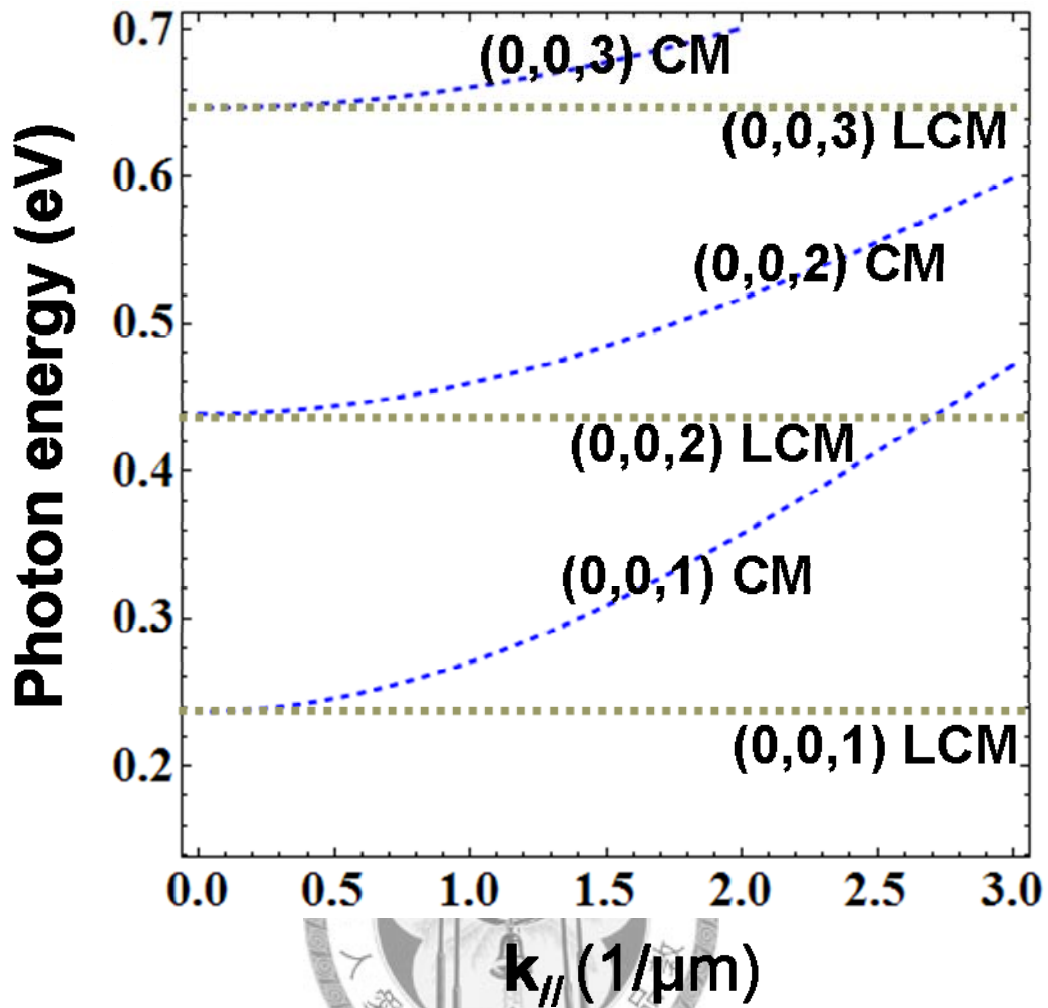


Fig. 4.10 The theoretical dispersion curves of CMs and LCMs.

are all smaller than three times of hole diameter.

It is expected that when the hole diameter is small ($1\mu\text{m}$), only the incident light coupled to the cavity modes can have extraordinary transmission through top metal film into the cavity, this leads to a weak reflection and dark lines. However, when the hole diameter becomes large ($2.5\mu\text{m}$), the transmission of incident light with different wavelengths also becomes significant, only those light coupled to cavity

mode can propagate in the cavity, all others are scattered away. These cavity modes will re-emit from the holes to the far-field and enhance the reflection spectra (bright lines).

Consider the dispersion relation of reflection spectra for samples J and K whose diameters are 3.5 and 4.5 μm , respectively as shown in Fig. 4.11 (a) and (b), respectively. For larger hole size and shorter wavelengths, the LCMs gradually disappear, this is because the leakage of light resonated in the cavity through surface hole array becomes too large to be ignored. Highly leakage of light for larger hole size breaks the resonance condition in the direction normal to the surface of samples. This makes the dispersion relation of reflection spectra for large holes gradually approach to the dispersion relation of reflection spectra for sample D whose leakage of light in the cavity is larger either, as shown in Fig. 4.8 (a).

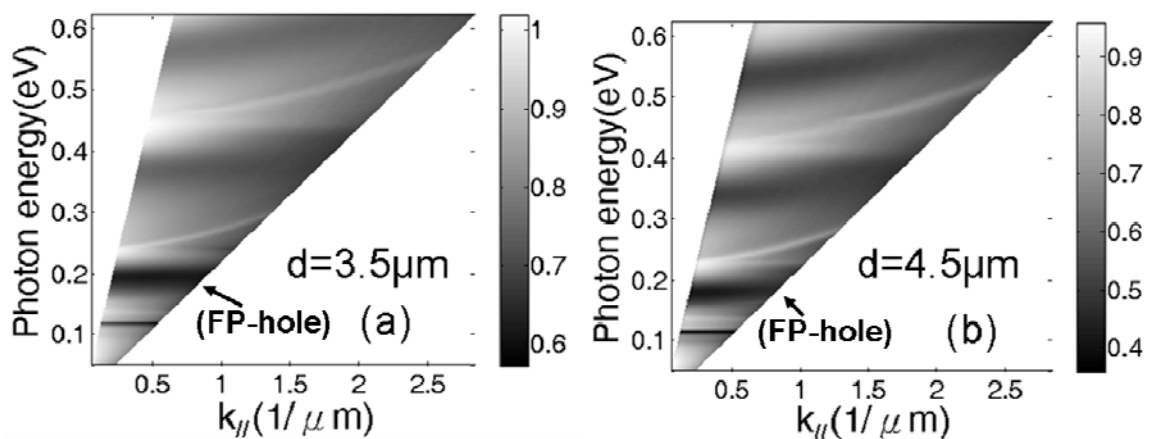


Fig. 4.11 The dispersion relation of reflection spectra of samples (a) J and (b) K.

The wavelengths of CM and LCMs are independent of hole diameter. However, the wavelengths of the other horizontal broad-band dark modes denoted as FP-hole in Fig. 4.9 (c) and Fig. 4.11(a) and (b) are not. They are the Fabry-Perot hole shape resonance (FP-hole) modes resonated in the edges of the holes and whose wavelengths are linear dependent with the hole diameter. Fig. 4.12 shows the measured wavelength of FP-hole modes to the hole diameter with the incident angle $\varphi=12^\circ$ for samples I to K and another CTE sample with $d=t_{\text{ox}}=2\mu\text{m}$. The linear fit curve of measured points is

$$\lambda=4.14+0.64d$$

(4.19)

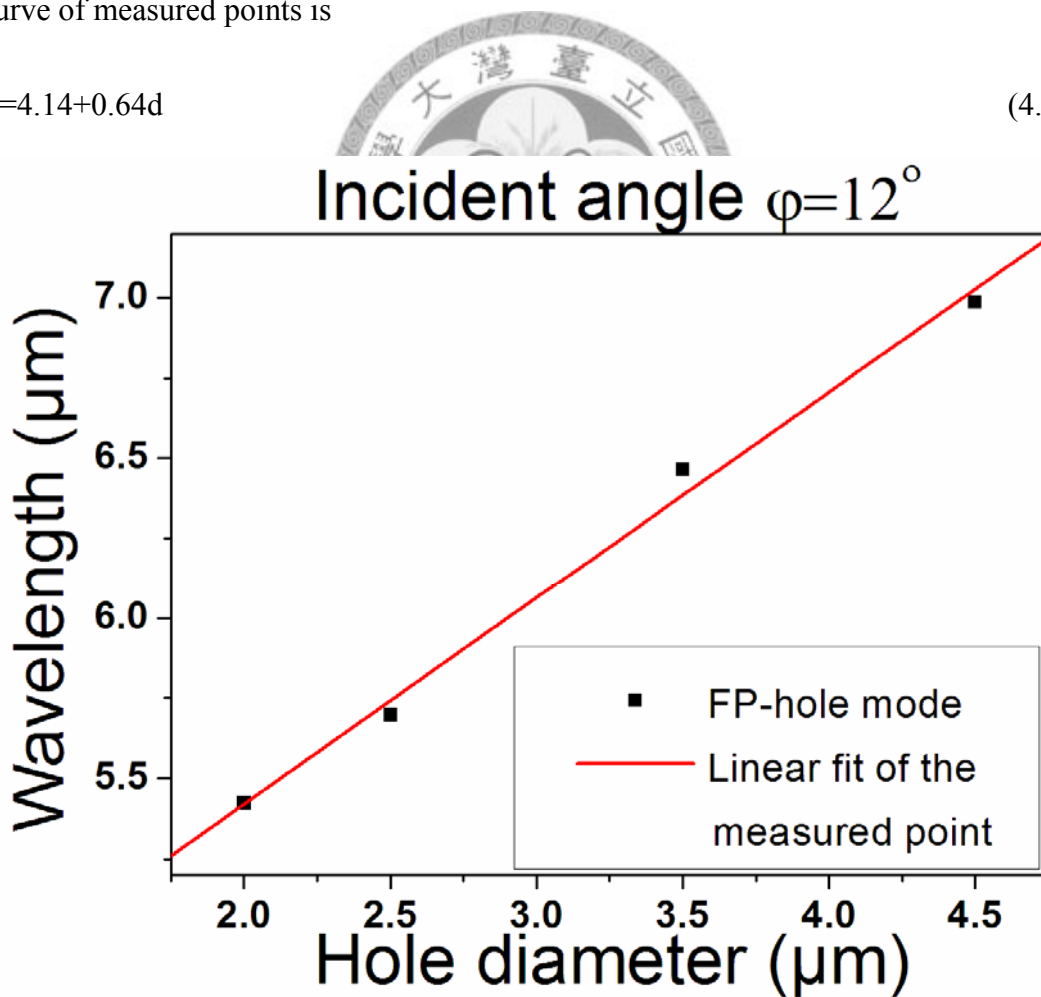


Fig. 4.12 The relation of the wavelength of FP-hole modes to the hole diameter

Fig. 4.13 shows the reflection spectra at $\varphi=12^\circ$ for samples L to N whose diameters of holes are fixed at $2\mu\text{m}$ but the densities of total hole area are different. The holes of sample N are arranged in hexagonal lattice instead of RDHA in order to offer the maximum values of density of total hole area to 40% for wide range comparison. Without considering the SPPs and Bragg scattered CMs of sample N, it can be seen that the wavelengths of dark modes (0,0,1) and (0,0,2) CMs are almost the same except a tiny red-shift for larger densities of total hole area. Higher densities of holes only lower the reflection intensity of modes.

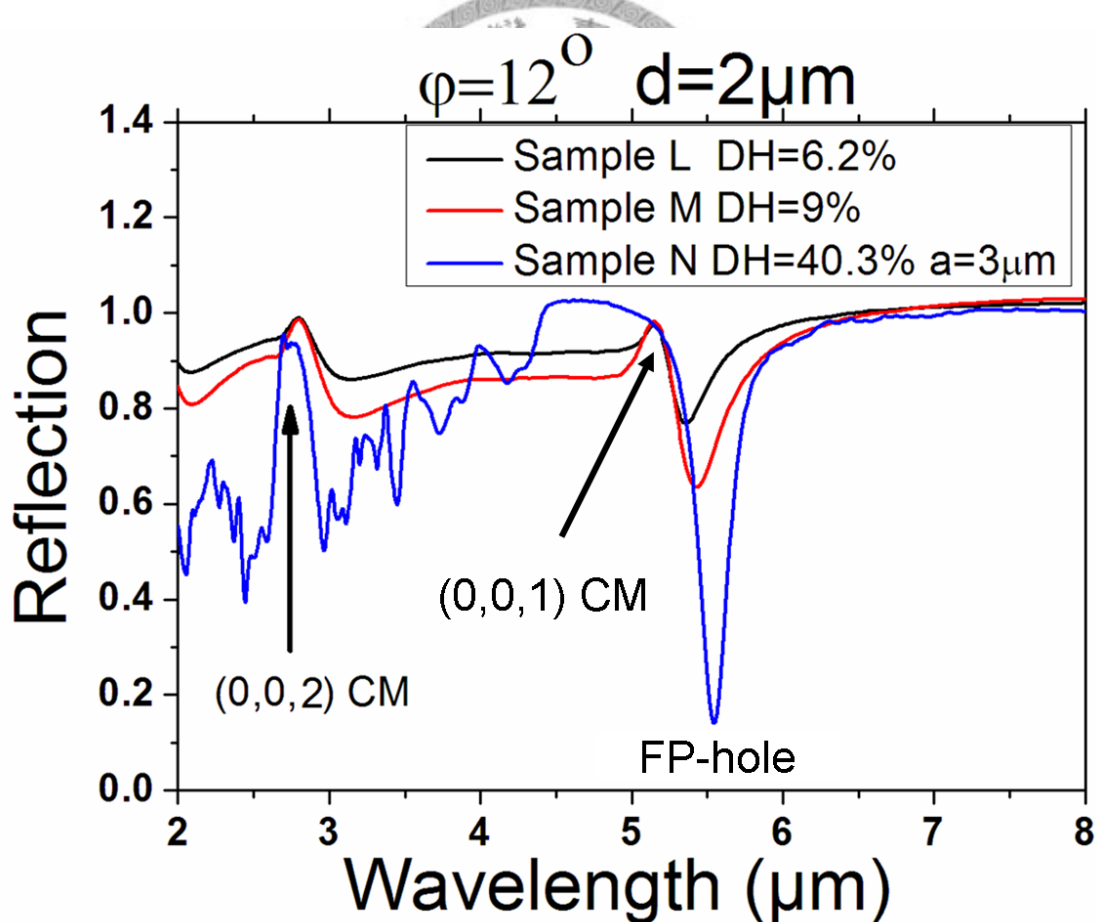
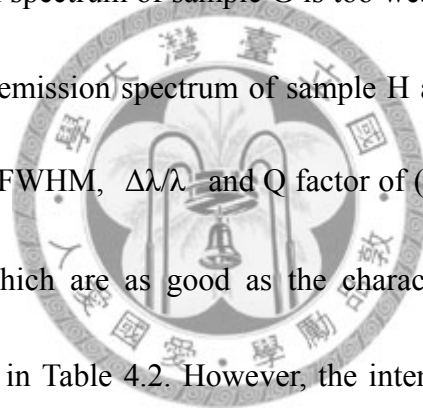
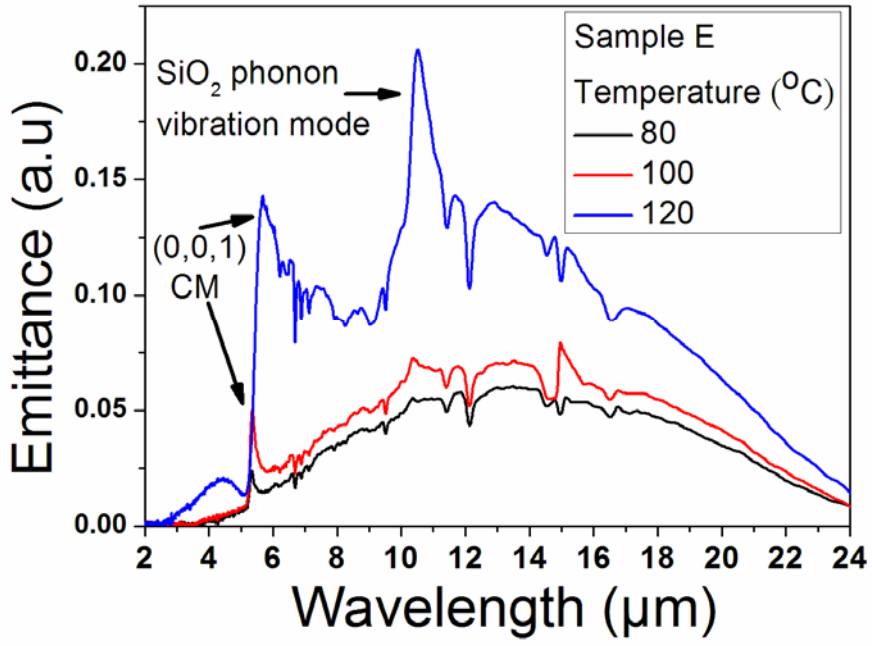


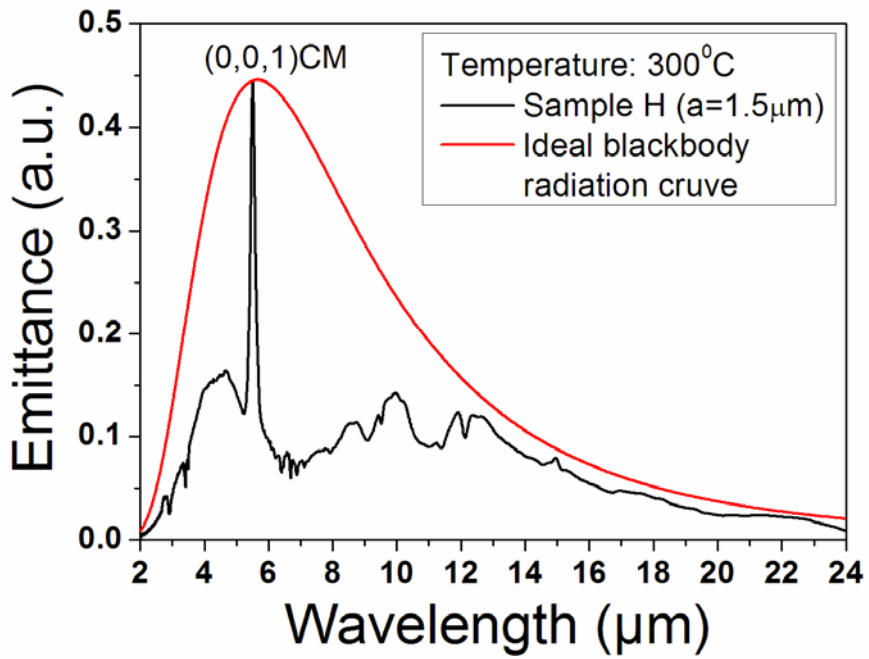
Fig. 4.13 The reflection spectra of sample L to N with the fixed incident and reflective angles $\varphi = 12^\circ$ and the fixed diameters of holes $d=2\mu\text{m}$.

Finally, the emission spectra of samples D to J were investigated; none of CTEs with top thin silver films without holes (samples D to F) can offer good emission spectra in the temperature over 140° C. Fig. 4.14(a) shows the emission spectrum of sample E. Once the temperature was elevated from 80° to 100° C, the quality of surface thin film degenerates so that the background thermal radiation of SiO₂ phonon vibration modes around 10 μm [53] can not be suppressed the surface thin films are too thin to offer the good thermal stability in high-temperature operation. For CTEs with RDHA, the emission spectrum of sample G is too weak to be ignored due to low density of holes. For the emission spectrum of sample H at 300° C as shown in Figs. 4.14 (b), the wavelength, FWHM, $\Delta\lambda/\lambda$ and Q factor of (0,0,1) CM is 5.51 μm, 0.17, 0.03, 33, respectively, which are as good as the characteristics of (0,0,1) CM of sample B as summarized in Table 4.2. However, the intensity of (0,0,1) CM is very weak due to low density of total hole area by comparing Fig. 4.14 (b) with Fig. 4.2 (b). For the emission spectra of samples I and J at 300° C as shown in the Fig. 4.14 (c) and (d), respectively, larger hole size broaden the bandwidth of resonance modes so that the difference between emissions spectra and background blackbody radiation gradually smears out. It should be noted that the maximum density of total hole area can not be enlarged too much in order to maintain the random degree of holes. Low output intensity is the main drawback of CTEs with RDHA.

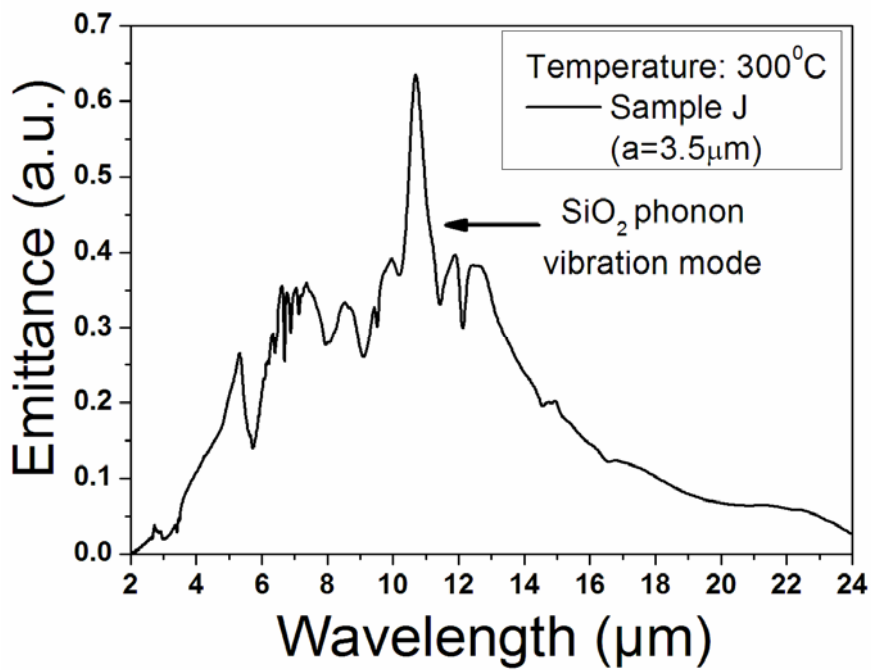
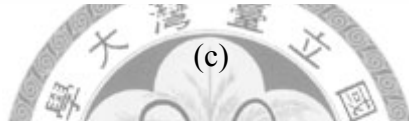
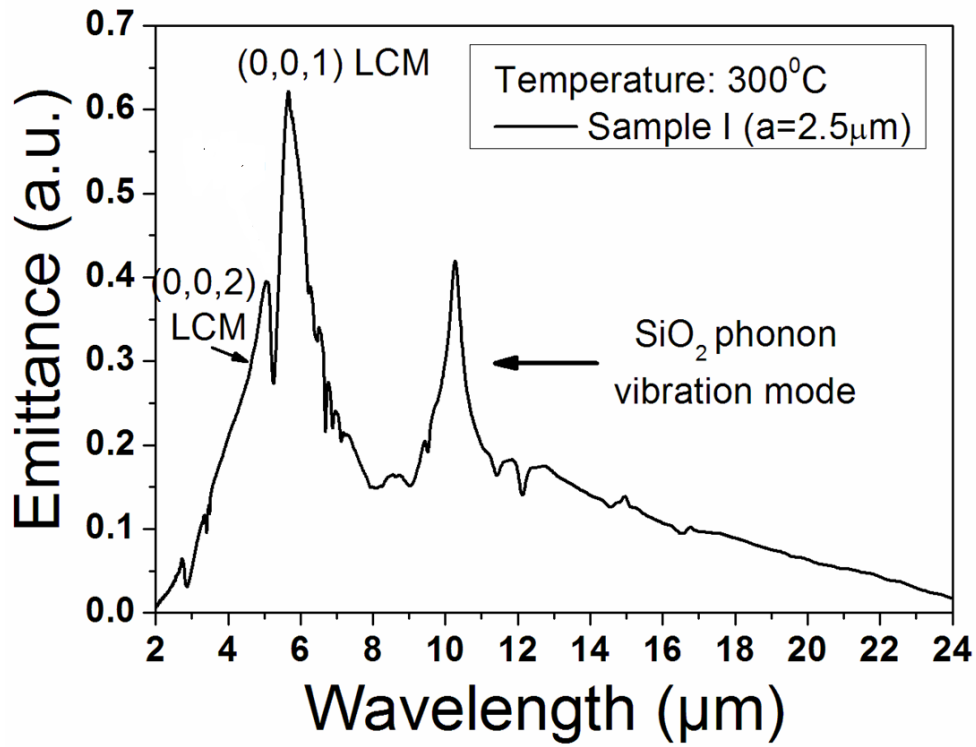




(a)



(b)



(d)

Fig. 4.14 The emission spectra of samples (a) E, (b) H, (c) I and (d) J in the normal direction ($\varphi = 0^\circ$).

In conclusions, CTEs with RDHA had been realized successfully, by analyzing the hole size effect on the resonant modes in the dispersion relation of reflection spectra, it is found that larger scattering of light through larger surface holes array would form the LCMs and FP-hole. When the hole diameter is small, only the incident light coupled to the CMs and LCMs can have extraordinary transmission through top metal film into the cavity, this leads to a weak reflection and dark lines. When the hole diameter becomes large, the transmission of incident light with different wavelengths becomes significant, only those light coupled to CMs and LCMs can propagate or resonate in the cavity and re-emit from the holes to the far-field so that changes the reflection spectra from dark lines into white lines. When the hole diameter is larger than or equal to $2.5\ \mu\text{m}$, the FP-hole modes appear and the wavelengths of FP-hole modes are linear dependent on the hole size. Finally, the emission spectra of CTEs with RDHA are pure and narrow-band if the hole size is small. However, their output intensities are very weak due to low density of total hole area.

4.3 Cavity thermal emitters with short period of hole array

Although CTEs with RDHA could offer pure emission spectra without SPPs modes and Bragg scattered CMs, their emission intensities are much weaker due to

low densities of holes. In this section, novel CTEs with short period of hole array (SPHA) are proposed to overcome the intensity problem. High output intensities, high temperature stability, low FWHM of emission peaks and pure emission spectra without SPPs modes and Bragg scattered CMs could be achieved simultaneously. Besides, non-ideal effects such as LCMs are weak either.

4.3.1 Experiments

The side view, top view and fabrication processes of CTEs with short period hole array (SPHA) are identical as those described in Sec. 4.1.1. The structure parameters of all samples O, P and Q are summarized in Table 4.4. The reflection spectra are measured along ΓK direction with angle ϕ normal to the surface as shown in Fig. 4.1 (b).

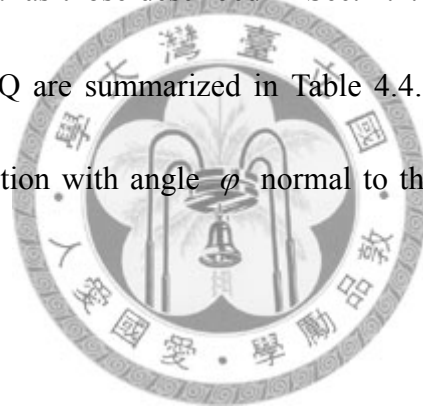


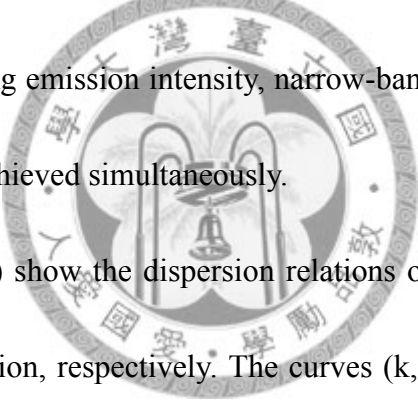
Table 4.4 The structure parameters and emission peaks of samples O, P and Q, d

denotes the diameters of holes and h denotes the thickness of to silver film.

Sample	a (μm)	d (μm)	t_{ox} (μm)
O	2.3	1.15	2
P	1.7	1	2
Q	1.7	1	1.6

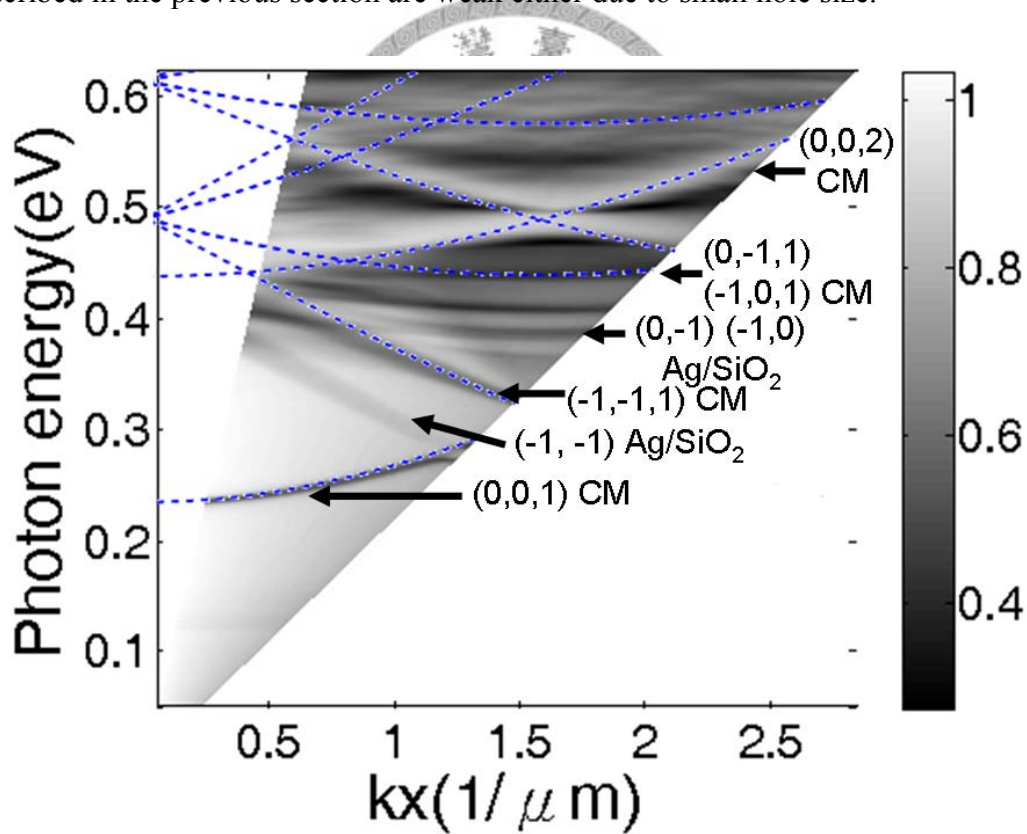
4.3.2 Results and discussion

The design principle of CTEs with SPHA is very simple. In order to get high output intensities, holes are arranged in the highest packed form: hexagonal lattice. In order to reduce the FWHM of emission peaks and eliminate non-ideal effect such as LCMs, the diameters of holes were chosen as small as possible. Finally, the period of hole array is shrunk as small as possible in order to place more holes inside the top Ag layer to increase the overall output intensities. Interesting enough, once these three criteria are satisfied, high performance cavity thermal emitters with good high temperature stability, strong emission intensity, narrow-band emission peaks and pure emission spectra can be achieved simultaneously.



Figs. 4.15 (a) and (b) show the dispersion relations of reflection for samples O and P along the ΓK direction, respectively. The curves (k, ℓ, m) CM denote the CMs whose wave vectors satisfy Eq. (4.9) with (k, ℓ, m) . Similarly, the curves (i, j) Ag/SiO₂ denotes the SPPs modes whose wave vectors satisfy Eq. (4.10). For small period of hole array, G_1 and G_2 of Eq. (4.6) and (4.7) becomes large due to small values of a . Substituting large G_1 and G_2 into Eq. (4.9) and (4.10) yields higher ω so that moves the SPPs modes and Bragg scattered CMs to the higher energy in the dispersion relation of reflection spectra. Compared Fig. 4.15 (a) with Figs. 4.3 (b) and 4.3 (d), when the period of hole array shrinks from $3\mu\text{m}$ to $2.3\mu\text{m}$, all Bragg scattered CMs

and SPPs modes are shifted from the energies above 0.4eV at $k_x=0$ as shown in Fig. 4.3 (d) to the higher energies above 0.48eV at $k_x=0$ as shown in Fig. 4.15 (a); once the period of hole array continue shrinks to the 1.7 μm as shown in Fig. 4.15 (c), all Bragg scattered modes and SPPs modes are shifted to the even higher energy above 0.6eV at $k_x=0$. The reflection spectra becomes purer for smaller period, gradually approach the reflection spectra of CTE with RDHA by comparing Figs. 4.15 (a) and (b) with Fig. 4.9 (a). Besides, the non-ideal effect such as localized cavity modes as described in the previous section are weak either due to small hole size.



(a)

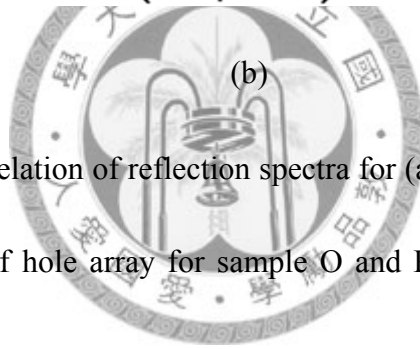
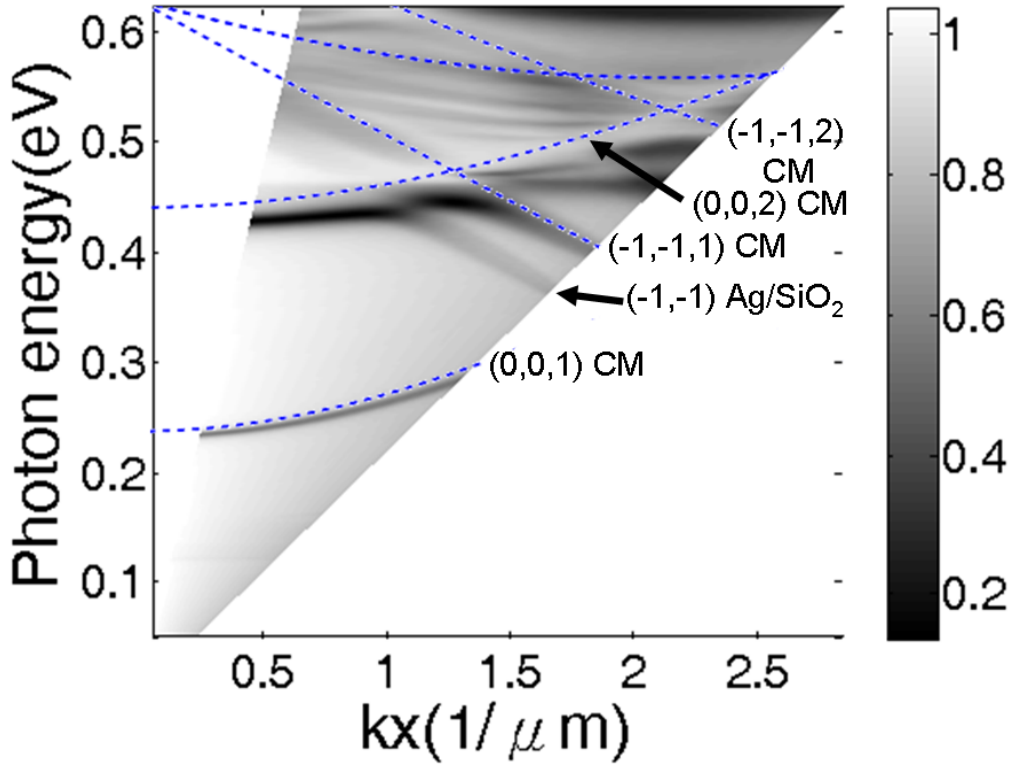
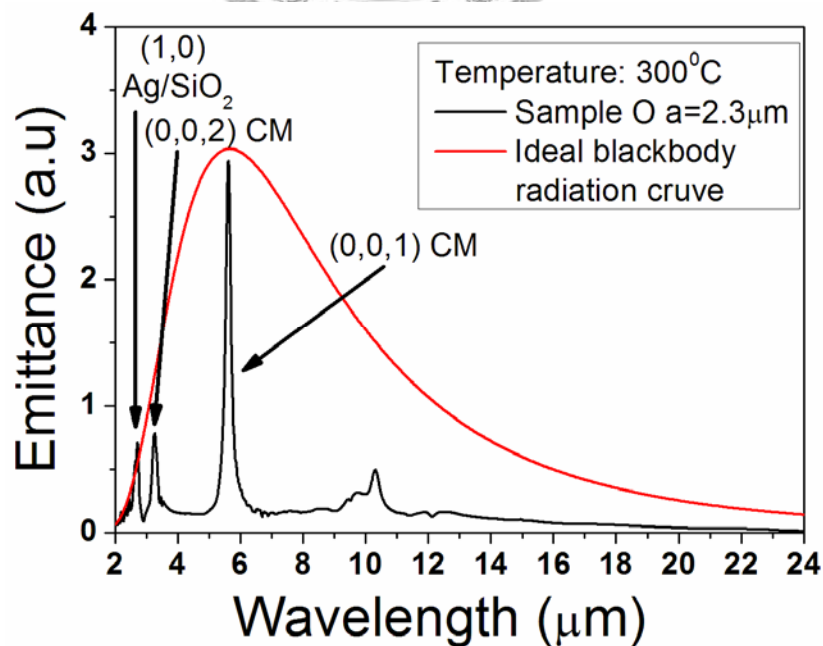


Fig. 4.15 The dispersion relation of reflection spectra for (a) sample O and (b) sample P. The period of hole array for sample O and P are $2.3 \mu\text{m}$ and $1.7 \mu\text{m}$, respectively.

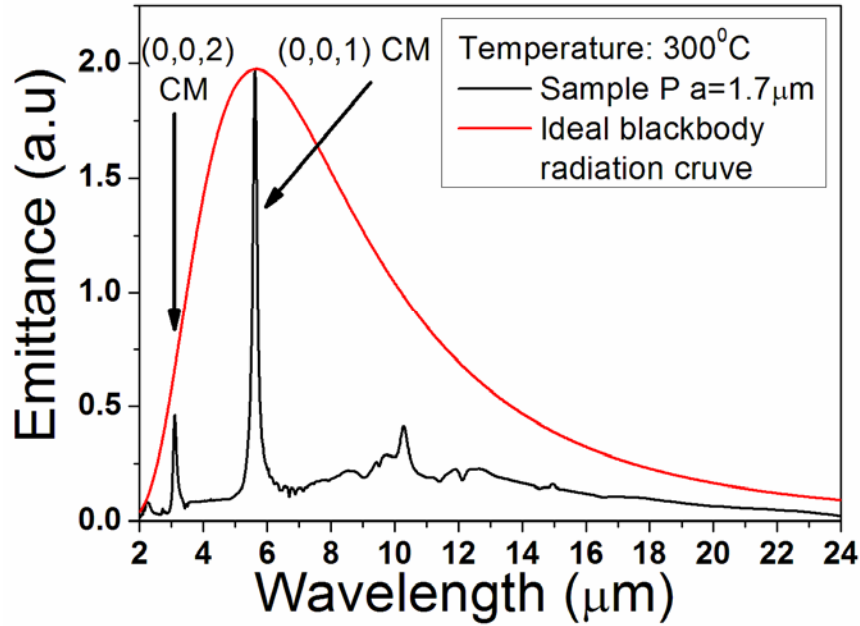
Figs. 4.16 (a) and (b) display the emissions spectra for samples O and P in the normal directions, $(1,0) \text{ Ag/SiO}_2$ denotes the $(1,0) \text{ Ag/SiO}_2$ degenerated modes whose wave vectors satisfy Eq. (4.12) with $(i,j) = (\pm 1,0), (0,\pm 1)$ or $(\pm 1,\pm 1)$, respectively. Compared Fig. 4.16 (a) with Fig. 4.3(b), when the period of hole array shrinks from 3 to $2.3 \mu\text{m}$, the $(1,0) \text{ Ag/SiO}_2$ degenerated mode are shifted from $3.86 \mu\text{m}$ to $2.72 \mu\text{m}$, the Bragg scattered $(1,0,1)$ CMs composed of six degenerated cavity modes with

$(k, \ell, m) = (\pm 1, 0, m), (0, \pm 1, m)$ or $(\pm 1, \pm 1, m)$ are shifted from $3.1 \mu\text{m}$ to $2.58 \mu\text{m}$ where blackbody radiation is too weak to be observed. For the emission spectrum of sample P whose period of hole array shrinks to $1.7 \mu\text{m}$ as shown in Fig. 4.16 (b), all SPPs and Bragg scattered CMs are shifted to the shorter wavelength where blackbody radiation are too weak to be observed although there are still reflection dips observed in the reflection spectra for such modes as shown in Fig. 4.15 (b).

Compared the emission spectra of sample P shown in Fig. 4.16 (b) with the emission spectra of sample H shown in Fig. 4.14 (b), it can be found that the emission spectra of CTEs with SPHA can be as pure as CTEs with RDHA, but the output intensity of CTEs with SPHA are much stronger than CTEs with RDHA due to high density of holes.



(a)



(b)

Fig. 4.16 The emission spectra in the normal direction $\varphi=0^\circ$ for (a) sample O and (b) sample P. The period of hole array for sample O and P are $2.3\mu\text{m}$ and $1.7\mu\text{m}$, respectively. The thicknesses of SiO_2 of both samples are $2\mu\text{m}$.

The FWHM, $(\Delta\lambda)/\lambda$, Q factors and the output powers of (0,0,1) CM for samples O and P are $(0.2\mu\text{m}, 0.17\mu\text{m})$, $(0.035, 0.03)$, $(28.6, 33)$ and $(186\text{mW}/\text{cm}^2, 137\text{mW}/\text{cm}^2)$, respectively. All of them are better than those of the traditional plasmonic thermal emitters (PTEs) could achieve as summarized in Table 4.3. Another advantage of CTEs is that CMs of CTEs in the direction other than normal direction would not split into four branches across wide energy band as the SPPs modes of PTEs as shown in Fig. 4.3 (a) but would exhibit only slight blue shift in the

narrow energy band as shown in Fig. 4.15 (b), especially for large k_x (large φ).

The dispersion curves and the emission peaks of the CTEs with SPHA are tunable simply by changing the thickness of SiO_2 according to Eqs. (4.16) and (4.17).

Fig. 4.17 shows emission spectrum in the normal direction ($\varphi=0^\circ$) for sample Q with the SiO_2 thickness of $1.6\ \mu\text{m}$, the wavelength of (0,0,1) CM is $4.69\ \mu\text{m}$. The FWHM, $(\Delta\lambda)/\lambda$, Q factor and output power of (0,0,1) CM are $0.119\ \mu\text{m}$, 0.0253, 39 and $140\text{mW}/\text{cm}^2$, respectively.

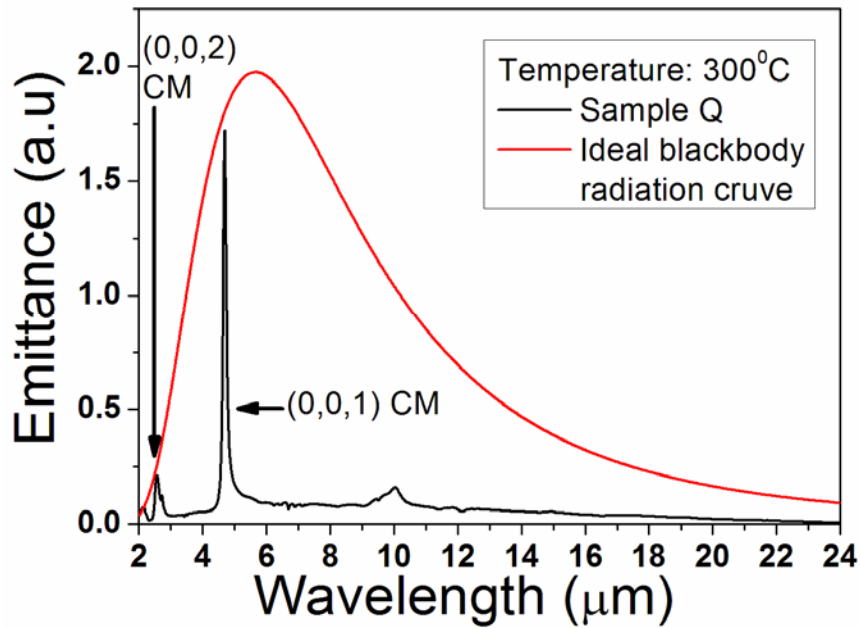


Fig. 4.17 The emission spectrum for sample Q. The thickness of SiO_2 is $1.6\ \mu\text{m}$.

Finally, compared the emission spectra of sample P as shown in Fig. 4.16 (b) to sample E as shown in Fig. 4.14(a), the CTE with top thin silver film can not work well in the high temperature due to the stability of top thin film, the key point is that

the surface thin film can not be thicker than the skin depth of silver ($\sim 20\text{nm}$) too much in order to let the light resonated in the cavity to leak out the thin silver film to outside. However, such thin thicknesses can not offer good thermal stability in high temperature operation. For CTEs with SPHA, the surface reflective mirror of the Fabry-Perot resonance cavity is formed by the subwavelength circular holes, the minimum skin depth of subwavelength holes in normal direction $\varphi = 0^\circ$ is [71]

$$\delta_h = \frac{1}{\sqrt{\left(\frac{2\pi}{\lambda_c}\right)^2 - \left(\frac{2\pi}{\lambda_0}\right)^2}} \quad (4.20)$$

where $\lambda_c = \frac{\pi d}{1.841}$ is the maximum cutoff wavelength of subwavelength holes, λ_0 is the wavelength of radiation modes guided in the subwavelength circular holes.

Fig. 4.18 shows the calculation of minimum skin depth of subwavelength holes in normal direction $\varphi = 0^\circ$. Since the skin depths of subwavelength holes are much larger than the skin depth of silver, the thickness of surface silver film can be elevated from 15nm of sample E to the 100nm of sample P. Fig. 4.19 shows the comparison of reflection spectra for sample P and sample E at $\varphi = 12^\circ$, almost the same reflection spectra are obtained except at the wavelength smaller than $2.5\mu\text{m}$ where SPPs and Bragg scattered CMs of sample P appear. However, CTEs with SPHA could offer better thermal stability in the high-temperature operation where CTEs with top thin silver film could not achieved.

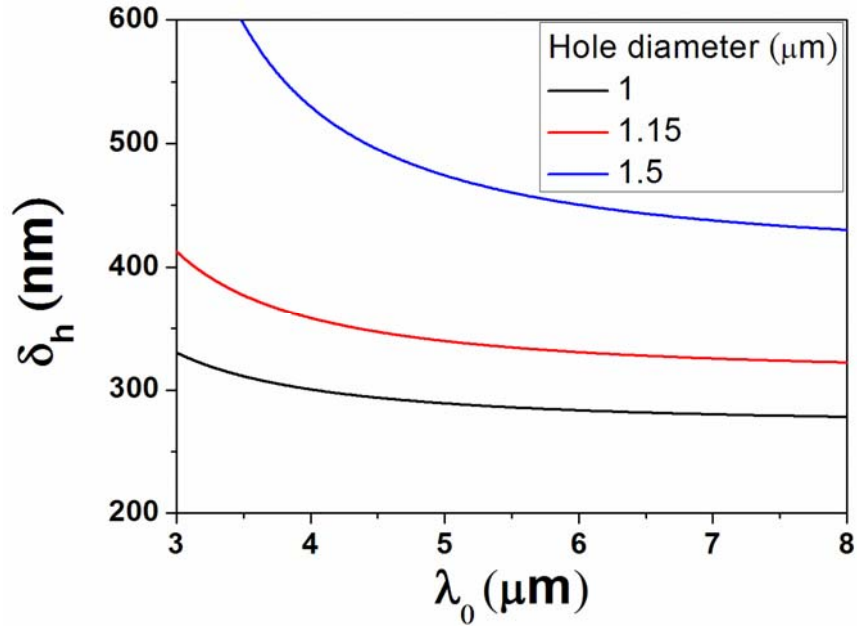


Fig. 4.18 The calculation of minimum skin depth of subwavelength holes to the wavelengths of lights guided inside the holes according to Eq. (4.23).

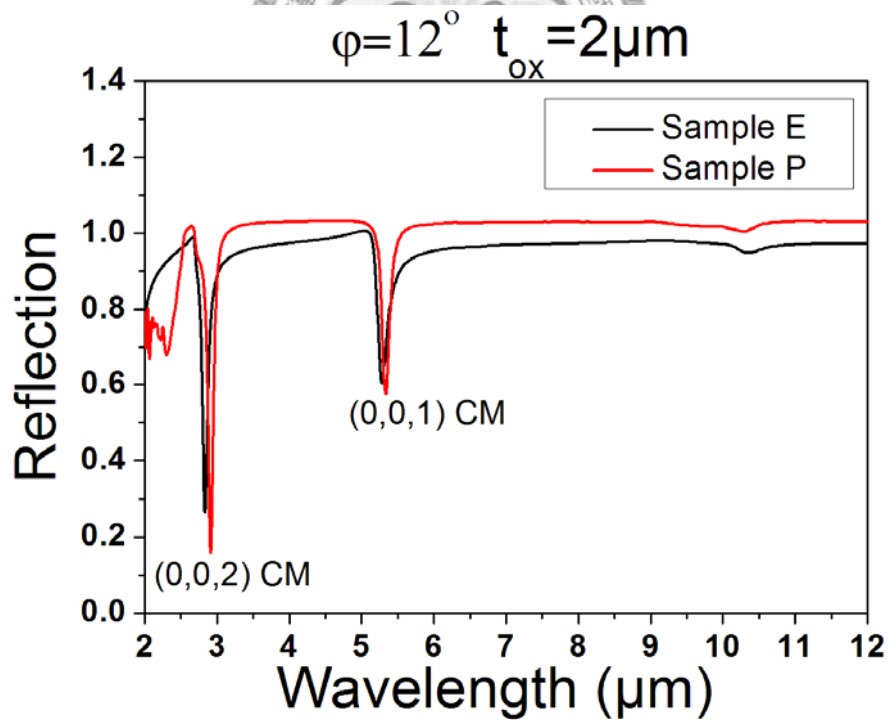
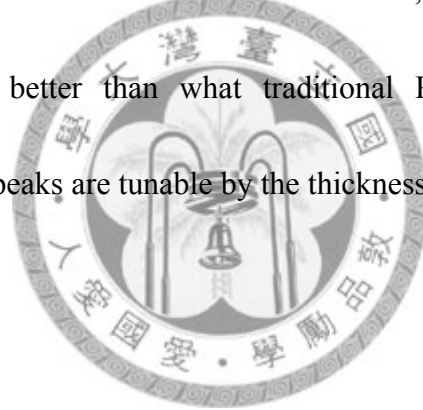


Fig. 4.19 The reflection spectra at $\varphi=12^\circ$ for sample E which is a CTE with 15nm top thin silver film and sample P which is a CTE with SPHA. The period and diameter of hole array of sample P are 1.7 μm and 1 μm , respectively.

In conclusions, high performance mid-infrared narrow-band CTEs with SPHA have been realized successfully. The SPPs modes and Bragg scattering CMs are shifted to the short wavelengths by short period where blackbody radiations are too weak to be observed. Small hole size eliminates non-ideal effects such as LCMs and FP-hole modes and offers narrower bandwidth emission peaks with small FWHM, The thickness of top silver film is thick enough to offer good thermal stability in high temperature operation. High density surface hole array offer strong emission intensity where CTEs with RDHA could not achieve. The FWHM, $(\Delta\lambda)/\lambda$ and Q factors are demonstrated to be all better than what traditional PTEs could achieve. The wavelengths of emission peaks are tunable by the thickness of the cavity.



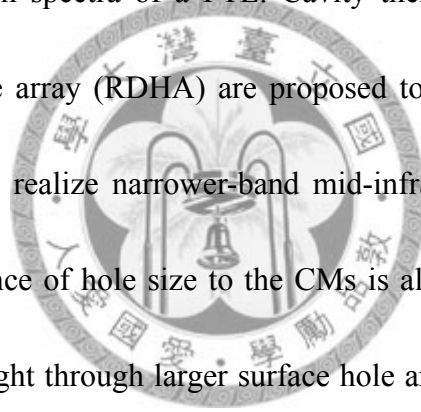
Chapter 5 Conclusions

In this thesis, the fundamental concepts of surface plasmon polaritons (SPPs) have been described. The characteristics of extraordinary transmission through a silver film perforated with periodic hole array in far infrared region have been investigated in detail. The characteristics of plasmonic thermal emitter with grating on top silver film are also discussed.

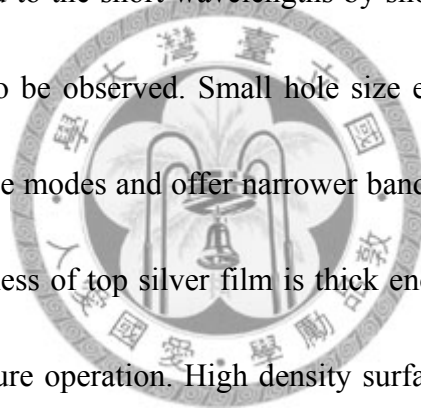
In chapter 3, the extraordinary transmission characteristics of silicon substrates and plasmonic thermal emitters with a silver film on top perforated with hole array arranged in a rhombus lattice are investigated in theory and experiment. For the transmission experiments of silicon substrates perforated with hole array arranged in a rhombus lattice, it is found that the transmissions of Ag/Si modes are approximately linearly dependent on the numbers of degenerated modes in the longer wavelength range where the couplings between Ag/Si and Ag/air modes are weak. In the shorter wavelength range where Ag/Si and Ag/air are coupled together, the transmission intensities are approximately constant without apparent peaks in the wavelength range longer than the Ag/air modes and decay rapidly in the wavelength smaller than the Ag/air modes due to asymmetric slope of the Ag/air mode in the spectra. For plasmonic thermal emitters with rhombus lattice, the same characteristic are observed either. Only hexagonal lattice produce the strongest emission peak due to largest

degenerated modes. The peak intensities follow the blackbody radiation curve multiplying transmission efficiency of the top metal film which is dependent on the numbers of degenerated modes.

In chapter 4, the SiO₂ thickness of PTEs is increased to the order of μm , it is found that not only SPPs modes but also cavity modes (CMs) exist in the reflection and emission spectra. The CMs would be scattered by the periodic hole array and result in many Bragg scattered CMs in the spectra. CMs exhibited better performance than SPPs in the emission spectra of a PTE. Cavity thermal emitters (CTEs) with randomly distributed hole array (RDHA) are proposed to eliminate Bragg scattered CMs and SPPs modes to realize narrower-band mid-infrared thermal emitters with purer spectra. The influence of hole size to the CMs is also investigated, it is found that larger scattering of light through larger surface hole array would form the LCMs and FP-hole modes. When the hole diameter is small, only the incident light coupled to the CMs and LCMs can have extraordinary transmission through top metal film into the cavity, this leads to a weak reflection and dark lines. When the hole diameter becomes large, the transmission of incident light with different wavelengths becomes significant, only those light coupled to CMs and LCMs can propagate or resonate in the cavity and re-emit from the holes to the far-field so that changes the reflection spectra from dark lines into white lines. When the hole diameter is larger than or equal



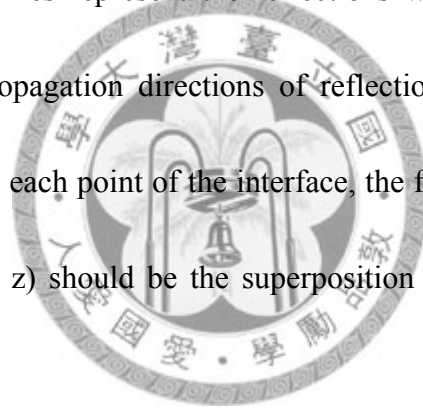
to $2.5\ \mu\text{m}$, the Fabry-Perot hole shape resonance (FP-hole) modes appear and the wavelengths of FP-hole modes are linear dependent on the hole size. Finally, the emission spectra of CTEs with RDHA are pure and narrow-band if the hole size is small. However, their output intensities are very weak due to low density of total hole area. Novel CTEs with short period of hole array (SPHA) are proposed to overcome the intensity problem. The surface holes are arranged in the highest-density hexagonal lattice with short period and small hole diameter. The SPPs modes and Bragg scattering CMs are shifted to the short wavelengths by short period where blackbody radiations are too weak to be observed. Small hole size eliminates non-ideal effects such as LCMs and FP-hole modes and offer narrower bandwidth emission peaks with small FWHM. The thickness of top silver film is thick enough to offer good thermal stability in high temperature operation. High density surface hole array offers strong emission intensities where CTEs with RDHA could not achieve. The FWHM, $(\Delta\lambda)/\lambda$ and Q factors are demonstrated to be all better than what traditional PTEs could achieve. Besides, the emission peaks of CTEs would not split into four branches in the direction other than normal direction as the SPPs modes of PTEs but exhibit little blue shift only. Finally, the wavelengths of emission peaks are tunable just by changing the thickness of the cavity.



Appendix [64~65]

Proof of momentum conservation law of grating coupling

Consider parallel polarization waves (TM mode) impinge on a one dimensional arbitrary shape interface whose period is Λ as shown in Fig. 2.4. The coordination (x, z) of interface in space is $(x, h(x))$ where $h(x)$ is in the period of Λ . The blue lines indicate the incident waves with common propagation directions (common k_{ix} and k_{iz}); the green lines and red lines represent the reflections waves and the transmission waves. Since that the propagation directions of reflection waves and transmission waves may be different at each point of the interface, the final electromagnetic waves in any point of space (x, z) should be the superposition of waves coming from all directions:



$$\vec{H}_r(x, z) = \int_{-\infty}^{+\infty} R(k_x) e^{i(k_x x + k_{rz} z)} d(k_x) \vec{y} \quad (A.1)$$

$$\vec{H}_t(x, z) = \int_{-\infty}^{+\infty} T(k_x) e^{i(k_x x - k_{tz} z)} d(k_x) \vec{y} \quad (A.2)$$

where k_{rz} and k_{tz} are the function of k_x because

$$k_{(r,t)z}^2 + k_x^2 = k_0^2 \mu_{r(1,2)} \epsilon_{r(1,2)} \quad (A.3)$$

$R(k_x)$ and $T(k_x)$ denote the amplitude of magnetic field of reflection waves and transmission waves traveling in the (k_x, k_{rz}) direction and (k_x, k_{tz}) direction respectively. The incident waves are described as:

$$\vec{H}_i = H_0 e^{i(k_{ix}x - k_{iz}z)} \vec{y} \quad (\text{A.4})$$

Consider an arbitrary interface point $(x, h(x))$, the boundary condition requires that Eq. (A.1) + Eq. (A.4) = Eq. (A.2):

$$\int_{-\infty}^{+\infty} [R(k_x) e^{ik_{iz}h(x)} - T(k_x) e^{-ik_{iz}h(x)}] e^{ik_x x} d(k_x) + H_0 e^{i(k_{ix}x - k_{iz}h(x))} = 0 \quad (\text{A.5})$$

Since that $e^{-ik_{iz}h(x)}$ is a periodic function in the period of Λ , it can be spanned into the Fourier series:

$$e^{-ik_{iz}h(x)} = \sum_{m=-\infty}^{+\infty} A_m e^{+i(m\frac{2\pi}{\Lambda}x)} \quad (\text{A.6})$$

$$\text{where } A_m = \frac{1}{\Lambda} \int_0^\Lambda e^{-ik_{iz}h(x)} e^{-i(m\frac{2\pi}{\Lambda}x)} dx \quad (\text{A.7})$$

Substitute Eq. (A.6) into Eq. (A.5) yields:

$$\int_{-\infty}^{+\infty} [R(k_x) e^{ik_{iz}h(x)} - T(k_x) e^{-ik_{iz}h(x)}] e^{ik_x x} d(k_x) + H_0 \sum_{m=-\infty}^{+\infty} A_m e^{i(k_{ix} + m\frac{2\pi}{\Lambda})x} = 0 \quad (\text{A.8})$$

Compared the integral term and summation term in Eq. (A.8), it is clear that if $k_x \neq k_{ix} + m\frac{2\pi}{\Lambda}$, the integral term should be zero because there is no corresponding

summation term to cancel this integral term. This can be achieved if one let

$R(k_x) = T(k_x) = 0$ when $k_x \neq k_{ix} + m\frac{2\pi}{\Lambda}$, that is:

$$R_y(k_x) = \sum_{m=-\infty}^{+\infty} R_m \delta(k_x - k_{ix} - m\frac{2\pi}{\Lambda}) \quad (\text{A.9})$$

$$T_y(k_x) = \sum_{m=-\infty}^{+\infty} T_m \delta(k_x - k_{ix} - m\frac{2\pi}{\Lambda}) \quad (\text{A.10})$$

where R_m and T_m are constants and δ is the Dirac delta function in math.

Substitute Eqs. (A.9) and (A.10) back into Eqs. (A.1) and (A.2) yields:

$$\vec{H}_r(x, z) = \sum_{m=-\infty}^{+\infty} R_m e^{i((k_{ix} + m\frac{2\pi}{\Lambda})x + k_{iz}z)} \vec{y} \quad (\text{A.11})$$

$$\vec{H}_i(x, z) = \sum_{m=-\infty}^{+\infty} T_m e^{i((k_{ix} + m\frac{2\pi}{\Lambda})x + k_{iz}z)} \vec{y} \quad (\text{A.12})$$

Eqs. (A.11) and (A.12) can be rewrote as

$$\vec{H}_r(x, z) = \sum_{m=-\infty}^{+\infty} R_m e^{i(k_{rx}x + k_{rz}z)} \vec{y} \quad (\text{A.13})$$

$$\vec{H}_t(x, z) = \sum_{m=-\infty}^{+\infty} T_m e^{i(k_{tx}x - k_{tz}z)} \vec{y} \quad (\text{A.14})$$

$$\text{where } k_{rx} = k_{tx} = k_x = k_{ix} + m\frac{2\pi}{\Lambda} \quad (\text{A.15})$$

The proof is complete.

It should be note that not only TM waves but also TE waves (perpendicular polarization) will obey the momentum conservation laws of grating coupling. The proof is the same as above except replacing the H field of TM mode with the electric field of TE mode. However, one should keep in mind that for TE waves and non-magnetic materials. The absolute value of “m” is not allowed to be too large since there are no evanescent wave (SPPs) for such structure as shown in Sec. 2.1.1.1. The TE waves after scattering can only by spanned in the basis of *finite waves* where evanescent waves are not allowed.

Finally, it should be note that the proof above did not ask what materials of medium1 and medium 2 should be; momentum conservation is a general law which can be use in dielectric/dielectric once the interface is periodic structure.

References

- [1] H. A. Bethe, Phys. Rev. **66**, 163 (1944).
- [2] T. W. Ebbesen, H. J. Lezec, H. F. Ghaemi, T. Thio, and P. A. Wolff, Nature (London) **391**, 667 (1998).
- [3] H. F. Ghaemi, Tineke Thio, D. E. Grupp, T. W. Ebbesen, H. J. Lezec, Phys. Rev. B **58**, 6779 (1998).
- [4] R. H. Ritchie, Phys. Rev. **106**, 874–881 (1957).
- [5] H. Raether, Surface Plasmons (Springer-Verlag, Berlin, 1988).
- [6] D. E. Grupp, H. J. Lezec, T. W. Ebbesen, K. M. Pellerin, and Tineke Thio, Appl. Phys. Lett. **77**, 1569 (2000).
- [7] H. J. Lezec, A. Degiron, E. Devaux, R. A. Linke, L. Martin-Moreno, F. J. Garcia-Vidal, and T. W. Ebbesen, Science **297**, 820 (2002).
- [8] Liang-Bin Yu, Ding-Zheng Lin, Yi-Chun Chen, You-Chia Chang, Kuo-Tung Huang, Jiunn-Woei Liaw, Jyi-Tyan Yeh, Jonq-Min Liu, Chau-Shiung Yeh, and Chih-Kung Lee, Phys. Rev. B **71**, 041405(R) (2005).
- [9] Seyoon Kim, Hwi Kim, Yongjun Lim, and ByoungHo LeeN, Appl. Phys. Lett. **90**, 051113 (2007).
- [10] W. L. Barnes, T. W. Preist, S. C. Kitson, and J. R. Sambles, Phys. Rev. B **54**, 6227 (1996).

- [11] S. C. Kitson, W. L. Barnes, and J. R. Sambles, *Phys. Rev. B* **52**, 11441 (1995).
- [12] D. Egorov, B. S. Dennis, G. Blumberg, and M. I. Haftel, *Phys. Rev. B* **70**, 033404 (2004).
- [13] A. Degiron, H.J. Lezec, N. Yamamoto and T.W. Ebbesen, *Optics Communications* **239**, 61-66 (2004).
- [14] A. Degiron and T. W. Ebbesen, *J. Opt. A: Pure Appl. Opt.* **7** S90-S96 (2005).
- [15] R. Gordon, A. G. Brolo, A. McKinnon, A. Rajora, B. Leathem, and K. L. Kavanagh, *Phys. Rev. Lett.* **92**, 037401 (2004).
- [16] Y. W. Jiang, L. D. C. Tzuang, Y. H. Ye, M. W. Tsai, C. Y. Chen, Y. T. Wu and S. C. Lee, 2009, *Opt. Express* **26**, 2631-2637 (2009).
- [17] Shaun M. Williams, Amanda D. Stafford, Trisha M. Rogers, Sarah R. Bishop, and James V. Coe, *Appl. Phys. Lett.*, **85**, 1472 (2004).
- [18] J. W. Lee, M. A. Seo, D. S. Kim, S. C. Jeoung, Ch. Lienau, J. H. Kang, and Q.-Han Park, *Appl. Phys. Lett.*, **88**, 071114 (2006).
- [19] Jin E. Kihm, Y. C. Yoon, D. J. Park, Y. H. Ahn, C. Ropers, C. Lienau, J. Kim, Q. H. Park, and D. S. Kim, *Phys. Rev. B* **75**, 035414 (2007).
- [20] A. Krishnan, T. Thio, T. J. Kim, H. J. Lezec, T. W. Ebbesen, P. A. Wolff, J. Pendry, L. Martin-Moreno, and F. J. Garcia-Vidal, *Opt. Commun.*, **200**, 1 (2001).

- [21] Tzu-Hung Chuang, Ming-Wei Tsai, Yi-Tsung Chang, and Si-Chen Lee, Appl. Phys. Lett. **89**, 033120 (2006).
- [22] J. B. Pendry, L. Martín-Moreno, F. J. García-Vidal, Science **305**, 847 (2004).
- [23] A. P. Hibbins, B. R. Evans, and J. R. Sambles, Science **308**, 670 (2005).
- [24] C. R. Williams, S. R. Andrews, S. A. Maier, A. I. Fernández-Domínguez, L. Martín-Moreno, and F. J. García-Vidal, Nature Photonics **2**, 175 (2008).
- [25] J. Gómez Rivas, Nature Photonics **2**, 137 (2008).
- [26] J. Saxler, J. Gómez Rivas, C. Janke, H. P. M. Pellemans, P. H. Bolívar, and H. Kurz, Phys. Rev. **B** 69, 155427 (2004).
- [27] T.-I. Jeon and D. Grischkowsky, Appl. Phys. Lett. **88**, 061113 (2006).
- [28] Xiangang Luo and Teruya Ishihara, Appl. Phys. Lett. **84**, 4780 (2004).
- [29] Zhao-Wei Liu, Qi-Huo Wei, and Xiang Zhang, Nano Lett. **5**, 957 (2005).
- [30] J. K. Mapel, M. Singh, M. A. Baldo, and K Celebi, Appl. Phys. Lett. **90**, 121102 (2007).
- [31] Kristofer Tvingstedt, Nils-Krister Persson, Olle Inganäs, Aliaksandr Rahachou, and Igor V. Zozoulenko, Appl. Phys. Lett. **91**, 113514 (2007).
- [32] Chi-Yang Chang, Hsu-Yu Chang, Chia-Yi Chen, Ming-Wei Tsai, Yi-Tsung Chang, and Si-Chen Lee, Appl. Phys. Lett. **91**, 163107 (2007).
- [33] W. -C. Kuo, C. Chou, and H. -T. Wu, Opt. Lett. **28**, 1329-1331 (2003)

- [34] Sergey I. Bozhevolnyi, Valentyn S. Volkov, Eloïse Devaux, Jean-Yves Laluet and Thomas W. Ebbesen, *Nature* **440**, 508-511 (2006)
- [35] Wayne Dickson, Gregory A. Wurtz, Paul R. Evans, Robert J. Pollard, and Anatoly V. Zayats, *Nano Lett* **8**, 281-286 (2008)
- [36] Genet, C, Ebbesen, T. W, *Nature* **445**, 39-46 (2007)
- [37] William L. Barnes¹, Alain Dereux² & Thomas W. Ebbesen, *Nature* **424**, 824-830 (2003)
- [38] M. W. Tsai, T. H. Chuang, C. Y. Meng, Y. T. Chang and S. C. Lee, *Appl. Phys. Lett* **89**, 173116. (2006)
- [39] T. H. Chuang, M. W. Tsai, Y. T. Chang, and S. C. Lee, *Appl. Phys. Lett.*, **89**, 173128 (2006)
- [40] C. Y. Chen, M. W. Tsai, Y. W. Jiang, Y. H. Ye, Y. T. Chang and S. C. Lee, *Appl. Phys. Lett.* **91**, 243111 (2007)
- [41] M. W. Tsai, J. W. Jiang, C. Y. Chen, Y. H. Ye and S. C. Lee, 2007, “Cavity mode in trilayer Ag/SiO₂/Au plasmonic thermal emitter”, 2007 Solid State Devices and Materials (SSDM 2007), Ibaraki, Japan, September.
- [42] Irina T. Sorokina and Konstantin L. Vodopyanov, Solid-State Mid-Infrared Laser Sources (Topics in Applied Physics), Springer; 1 edition (2003)
- [43] Bujin Guo, Yi Wang, Yang Wang, Han Q. Le, *Journal of Biomedical Optics* **12**,

- p. 024005 (2007)
- [44] Ivan Celanovic, David Perreault, and John Kassakian, *Physical Review B* **72**, 075127 (2005)
- [45] B. J. Lee and Z. M. Zhang, *J. Appl. Phys.* **100**, 063529 (2006)
- [46] B. J. Lee, Y.-B. Chen, and Z. M. Zhang, *Optics Letters* **33**, 204-206 (2008)
- [47] David L. C. Chan, Marin Soljačić, and J. D. Joannopoulos, *Physical Review E* **74**, 016609 (2006)
- [48] David L. C. Chan, Marin Soljačić and J. D. Joannopoulos, *Opt. Express* **14**, 8785-8796 (2006)
- [49] David L. C. Chan, Ivan Celanovic, J. D. Joannopoulos, and Marin Soljačić, *Physical Review A* **74**, 064901 (2006)
- [50] David L. C. Chan, Marin Soljačić, and J. D. Joannopoulos, *Physical Review E* **74**, 036615 (2006)
- [51] 李正中, 薄膜光學與鍍膜技術, 第五版, 附錄一, 藝軒圖書 (2006)
- [52] E. D. Palik, *Handbook of Optical Constants of Solids I & II* (Academic San Diego, CA, 1985)
- [53] C. T. Kirk, *Phys. Rev. B* **38**, 1255 (1988).
- [54] Yong-Hong Ye and Jia-Yu Zhang, *Optics Letters* **30**, 1521-1523 (2005)
- [55] Y. C. Jun, R. D. Kekatpure, J. S. White, and M. L. Brongersma, *Physical*

- Review B **78**, 153111 (2008)
- [56] Karl Joulain, Jean-Philippe Mulet, Francois Marquier, Re'mi Carminati, Jean-Jacques Greffet, Surface Science Reports **57**, 59-112 (2005)
- [57] David K. Cheng, Field and Waves Electromagnetics, 2nd, Addison-Wesley (1989)
- [58] Stefan A. Maier, Plasmonics: Fundamentals and Applications, Springer (2007)
- [59] Ashcroft/Mermin, Solid State Physics, Thomson (1976)
- [60] M. A. Ordal, Robert J. Bell, R. W. Alexander, Jr, L. L. Long, and M. R. Querry, Applied Optics **24**, 4493-4499 (1985)
- [61] M. A. Ordal, L. L. Long, R. J. Bell, S. E. Bell, R. R. Bell, R. W. Alexander, Jr., and C. A. Ward, Applied Optics **22**, 1099-1120 (1983)
- [62] B. Prade, J. Y. Vinet, and A. Mysyrowicz, Physical Review B **44**, 13556-13572 (1991)
- [63] S. Collin, F. Pardo, and J.-l. Pelouard, Opt express **15**, 4310 (2007)
- [64] Shun Lien Chuang, Physics of Photonic Devices, 2nd, Wiley (2009)
- [65] Hermann A. Haus, Waves and Fields in Optoelectronics, Prentice-Hall (1984)
- [66] Handbook of Instrumental Techniques for Analytical Chemistry, Ch. 15, edited by C. P. Sherman Hsu.
- [67] Sergey A. Darmanyan, Anatoly V. Zayats, Physics Review B **67**, 035424 (2003)

[68] R. W. Wood, Phys. Rev. **48**, 928 (1935)

[69] Yi-Tsung Chang, Tzu-Hung Chuang, Ming-Wei Tsai, Lung-Chien Chen, and

Si-Chen Lee, Journal of Applied Physics **101**, 054305 (2007)

[70] Mastui. T, Agrawal. A, Nahata. A, Nature **446**, 517-521 (2007)

[71] David M. Pozar, "Microwave Engineering", 3rd, Wiley (2005)

